SPECTROSCOPIC STUDY OF SPRITES

By

Takeshi Kanmae

RECOMMENDED:

Dr. Donald Hampton

Dr. William Simpson

Dr. Dirk Lummerzheim

Dr. John Olson

Dr. Hans Stanbaek-Nielsen
Advisory Committee Chair

Dr. Curt Szuberla
Chair, Department of Physics

APPROVED:

Dr. Paul Layer
Dean, College of Natural Science and Mathematics

Dr. John Eichelberger
Dean of the Graduate School

12/7/14

Date

SPECTROSCOPIC STUDY OF SPRITES

A

DISSERTATION

Presented to the Faculty

of the University of Alaska Fairbanks

in Partial Fulfillment of the Requirements

for the Degree of

DOCTOR OF PHILOSOPHY

By

Takeshi Kanmae, B.S.

Fairbanks, Alaska

Deember 2014

Abstract

Optical emissions from sprites—large electric discharges in the mesosphere caused by intense lightning strokes—have been studied for decades. Studies have identified that sprite emissions are primarily composed of molecular band emissions of nitrogen and notably identified the near ultraviolet and blue emission from the N_2^+ First Negative system, which provided direct evidence of ionization in sprites. This implies that further evidence of the ionization may be provided by the visible and near infrared emission from the N_2^+ Meinel system, which is more accessible from ground-based platforms, though anticipated strong quenching in the mesosphere and below have made the presence of the emission somewhat controversial. To investigate the presence of the Meinel emission along the vertical extent of sprites, we made ground-based spectral observations in 2005. The observed spectra were mainly composed of the N_2 First Positive system, and no or little indication of the Meinel bands were found. This study suggests that the quenching is indeed severe at sprite altitude, and it is difficult to study the ionization process in sprites via the Meinel emission. In addition, the data allowed us to investigate details of the First Positive emission from sprites. The observed First Positive spectra showed that the vibrational distribution of the upper state varies along the vertical extent of sprites, which is in agreement with previous reports, and furthermore this study indicates that the variation is associated with altitude, implying that collisional energy transfer processes play roles in exciting the First Positive emission, particularly at lower altitudes. Recent high-speed imaging observations have revealed the very dynamic nature of sprites: they develop within a few to 10 ms in forms of streamers and columnar glows. The underlying electron energies in these features have been inferred from their emissions in previous measurements, but they lacked either sufficient temporal or spatial resolution. To investigate the underlying electron energies, we made airborne spectral observations in 2009 with a slitless spectrograph, which provided temporal and spatial resolution improved over the previous measurements. The observed spectra clearly showed that the streamers consistently had a higher fraction of blue emission compared to the glows, indicating that the more energetic nature of the streamers. From the fractional blue emissions, the local electric fields were inferred to be 0.7 to $1.5E_k$ in the streamers and 0.3 to $0.6E_k$ in the glows, where E_k is the conventional breakdown electric field. The results support the interpretation of sprites as scaled analogs of streamer discharges observed in laboratory experiments.

Table of Contents

Page

List of Figures

List of Tables

Page

Acknowledgments

First and foremost, I would like to thank my advisor Hans Stenbaek-Nielsen. He has provided opportinities to participate in many observation campaigns, where I learned a lot from hands-on experiences. Without his insightful guidance, financial support, and constant encouragement and patience, I would not have been able to complete this dissertation. Second, I would like to thank two dear colleagues, Geoff McHarg of US Air Force Academy and Ryan Haaland of Fort Lewis College. I have been very fortunate to work with them over many years. A lot of good memories with Hans, Geff, and Ryan will remain forver.

I am grateful to Dave Sentman. He was always accessible to discuss various topics for hours, even when I stopped by at midnight. I am also grateful to Jeff Morrill of Naval Research Laboratory. He came all the way to Fairbanks in one winter to help me when I was stucked with computation of synthetic nitrogen spectra.

Many people have provided generous support to our sprite observation campaigns; I am grateful to all of them. Jim Desroschers have provided his expertise in optical instruments and electronics. Will Winn of New Mexico Tech has been a gracious host at the Langmuir Laboratory for Atmospheric Research. Jorgen Jensen, Jim Moore and all the members of the NCAR Earth Observing Laboratory team have supported our airborne observation campaign in 2009. Steve Cummer of Duke University have provided access to near real-time lightning data.

During the course of my graduate research, many colleagues and colloborators have provided helpful suggestions, generous assistance, and thoughtful encouragement; in particular, I thank Peter Jenissken (SETI Institute), Richard Sonnenfeld (New Mexico Tech), Toru Adachi (Waseda University, Tokyo, Japan), Richard Fernsler (Naval Research Laboratory), Mitsuteru Sato and Yukihiro Takahashi (Hokkaido University, Sapporo, Japan), Tomohiro Inoue (NHK, Tokyo, Japan), Jeff Tobolski (Aero Air, Hillsboro, OR), Mike Taylor (Utah State University), Walter Lyons (FMA Research, Fort Collins, CO), and Victor Pasko (Penn State University).

Several data sets presented in this dissertation were provided by others. These include the infrared imagry from the GOES satellites, provided by NOAA National Climatic Data Center, and the lightning data from the Naional Lightning Detection Network, provided by Vaisala via the Unidata Local Data Manager system.

Last, but definitely not the least, I am grateful to my family, particularly my father Wataru and my mother Yoshimi, for allowing me to pursue my passion thousands of miles away from home.

Chapter 1
Introduction

Large electric discharges above thunderstorms—now known as "sprites"—were first discovered about three decades ago. Visual sightings of flashes above thunderstorms had been reported for more than a century. But they were not identified before 1989 when a scientist unexpectedly recorded the first image of "an unusual luminous electric discharge over a thunderstorm" during a test of a low-light level TV camera [*Franz et al.*, 1990]. The reported optical events were later dubbed "sprites" by D. Sentman to reflect their elusive nature, but without implying specific underlying mechanisms [*Sentman et al.*, 1995].

The discovery sparked active research, particularly in the United States, but also in other countries, and it soon became clear that there are other forms of large-scale, short-lived optical events above thunderstorms—they are now known as "elves", "halos", "blue jets", and "gigantic jets" (Figure 1.1). These transient optical events, including sprites, are collectively termed as transient luminous events (TLEs) [*Lyons*, 1996]. Studies have shown that they are all caused by lightning activity in the troposphere, indicating that they are an optical manifestation of electric coupling between the troposphere and the upper atmosphere.

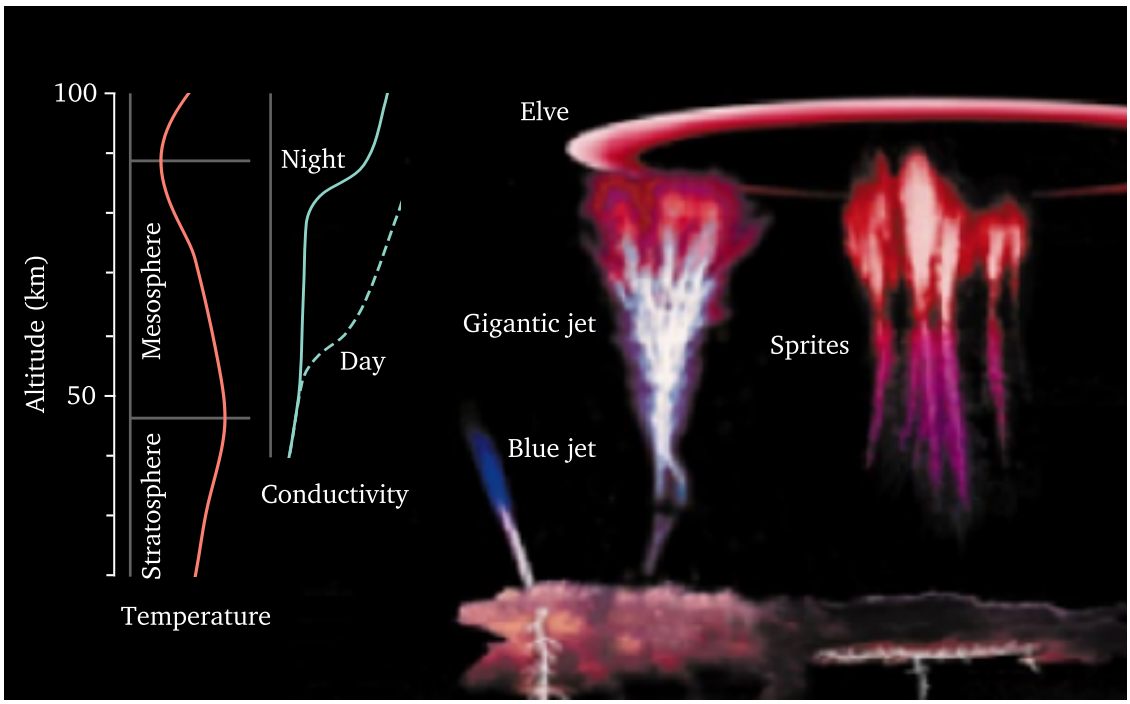

Figure 1.1. Schematics of transient luminous events (TLEs). The focus of this dissertation is spectral studies of sprites. The image was reproduced from [*Pasko*, 2003].

Sprites are electric discharges in the mesosphere caused by intense lightning strokes in the troposphere. They produce large structures in the altitude range of 40 to 90 km with lateral extent of 5 to 10 km [*Sentman et al.*, 1995]. They rarely occur singly but usually occur in clusters, occasionally packed together into a gigantic structure of 50 km or more across [*Sentman et al.*, 1995]. The clustering results in a wide variety of appearances resembling vertical columns, carrots, trees, wishbones, jellyfishes, fireworks, etc. [*Bór*, 2013].

The formation of these large structures proceeds in a form of propagating filamentary channels with transverse size of a few tens to hundreds of meters [*Gerken et al.*, 2000]. They rapidly propagate both downward and upward, frequently split into narrower channels, and quickly extend the full altitude range within a few ms [*Stenbaek-Nielsen and McHarg*, 2008]. The optical emissions from these filamentary channels and induced secondary emissions result in large flashes, which typically last for a few to 10 ms, though their luminosity has been observed to persist for over 100 ms [*Stenbaek-Nielsen and McHarg*, 2008]. The nature of sprites has been noted similar to that of streamer discharges—a type of transient electric discharges observed in laboratory experiments [*Pasko*, 2007; *Ebert et al.*, 2010].

This dissertation addresses issues relevant to the processes associated with the optical emissions from sprites. Previous spectral and photometric observations have identified the emissions from molecular band systems of nitrogen in wavelength ranges from the far ultraviolet to near infrared, and have provided insights into the processes associated with the emissions. However, these measurements did not have sufficient resolution to closely examine the spatial and temporal variation of the band emissions. To overcome these limitations, our research group has made two different types of spectral observations with improved resolution compared to the previous measurements. Using these data, this dissertation addresses unresolved issues raised by the previous studies.

1.1 Initial Electric Breakdown in the Lower Ionosphere

Sprites are large electric discharges in the mesosphere caused by intense lightning strokes in the troposphere. A lightning stroke produces a transient electric field above the cloud, and if the electric field is sufficiently strong, it may cause the breakdown in the lower ionosphere, triggering electric discharges or sprites. Sprites are almost exclusively produced by intense positive cloud-to-ground lightning strokes but very rarely by negative ones.

In the electrically conducting atmosphere, an electric field relaxes in a time scale determined by the local conductivity. Radioactivity, cosmic rays and energetic solar radiation constantly

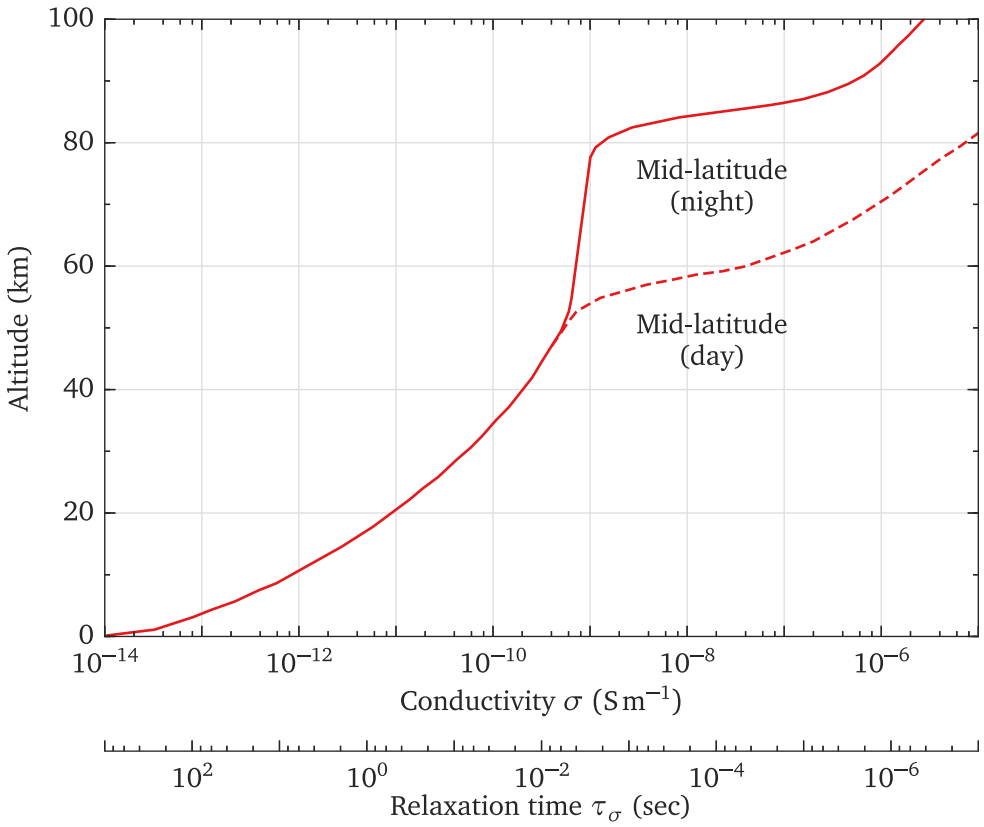

Figure 1.2. Typical atmospheric conductivity and corresponding relaxation time. The data were reproduced from [*Hale*, 1994].

produce ions and electrons and maintain the electric conductivity of the Earth's atmosphere [*Rakov and Uman*, 2003, p. 6]. The conductivity increases exponentially with altitude as the densities of ions and electrons increases, though it changes diurnally with the solar radiation above about 60 km altitude (Figure 1.2). The finite conductivity (and its vertical gradient) induces space charges in the atmosphere, and the space charges relax an electric field with a time constant given by

$$\tau_\sigma = \epsilon_0/\sigma, \tag{1.1}$$

where σ is the local conductivity and ϵ_0 is the permittivity in vacuum. The relaxation time decreases exponentially with altitude; it is about half an hour at the ground and reduces to about 1 ms at 80 km altitude (Figure 1.2).

Because of the finite conductivity of the atmosphere, the high-altitude region above a thundercloud is screened from the slowly intensifying electrostatic field produced by the cloud charges prior to a lightning stroke. The cloud charges build up via convective charge separation. The charge separation process occurs on a time scale of hundreds of seconds, while the local

relaxation time at the cloud top altitude, say 20 km, is about 1 s (Figure 1.2). Hence, as the cloud charges slowly build up, space charges immediately appear above the cloud top and screen the high-altitude region from the slowly intensifying thundercloud field.

But a lightning stroke suddenly removes charge from the cloud to the ground and produces a transient electric field above the cloud. The sudden charge removal typically occurs on a time scale of milliseconds, which is equivalent to the local relaxation time at about 80 km altitude. Hence, the remaining charges in the cloud and above the cloud top produce an electric field above the cloud up to about 80 km altitude. The penetrating electric field is referred as the "quasi-electrostatic field". This is because the electric field is electrostatic immediately after the charge removal, but persist only for a short period of time approximately equal to the local relaxation time at each altitude (Figure 1.2). The short duration of the quasi-electrostatic field, in part, determines the transient nature of sprites.

The sudden removal of a charge by a lightning stroke can be viewed as deposition of an identical charge but with opposite polarity. Hence, regardless of the actual charge structure in the cloud, the electrostatic field immediately after the charge removal is approximated by that of a dipole formed by the "deposited" charge and its mirror below the ground [*Pasko et al.*, 1995]. As a dipole electric field decays with distance, the quasi-electrostatic field decays with altitude z as z^{-3}.

On the other hand, the threshold field for electric breakdown falls off exponentially with altitude. Electric breakdown is fast formation of an ionized gas under the action of a sufficiently strong electric field*. In air, the electrons accelerated by an electric field ionize neutral species but also attach to oxygen atoms via dissociation of oxygen molecules. The electron attachment removes electrons from the gas and may prevent net ionization to occur. Hence, the quantitative criterion for the "sufficiently strong electric field" in air is that the electric field exceeds the threshold determined by the equality between the electron impact ionization rate and the electron attachment rate [*Bazelyan and Raizer*, 1998, p. 43]. These rates are functions of the reduced electric field E/N, the ratio of the electric field E to the gas density N. Therefore, the breakdown threshold is proportional to air density, which exponentially decreases with altitude; the threshold value is about $3\,\mathrm{MV\,m^{-1}}$ at the ground and reduces to about $50\,\mathrm{V\,m^{-1}}$ at 80 km altitude.

These altitude variations indicate that if the quasi-electrostatic field is sufficiently strong, it

*In the context of high-voltage engineering, the term "electric breakdown" is alternatively used to refer short circuiting of the voltage between an insulation gap [*Bazelyan and Raizer*, 1998, p. 12].

may exceed the breakdown threshold in the lower ionosphere, triggering electric discharges or sprites. The breakdown threshold falls off more rapidly with altitude than the strength of the quasi-electrostatic field, indicating that there may be a height above which the electric field exceeds the breakdown threshold. Modeling studies have estimated that the breakdown altitude to be at 70 to 80 km in the lower ionosphere [*Pasko*, 2007, references therein]. The predicted altitude in general agrees with the onset altitudes of sprites, which has been recently determined by triangulation measurements [*Stenbaek-Nielsen et al.*, 2010]

The breakdown in the lower ionosphere is not caused by all lightning strokes but caused only by those with large charge moment changes. A charge moment change is the product of the charge removed from the cloud and the height of the charge center from the ground. Under the dipole approximation, this quantity is a measure of the strength of the quasi-electrostatic field produced by a lightning stroke. Accordingly, only lightning strokes with large charge moment changes can produce a sufficiently strong electric field field and cause the breakdown in the lower ionosphere.

Studies have found that sprites are almost exclusively produced by particularly intense positive lightning strokes but very rarely by negative ones [*Boccippio et al.*, 1995; *Williams et al.*, 2007]. Positive and negative lightning strokes transfer net positive and negative charges from a thundercloud to the ground, respectively. Statistically speaking, positive lightning strokes, which consists of only 10 percent of global lightning strokes, produce much larger charge moment changes than negative ones [*Rakov and Uman*, 2003, Chapter 4 and 5]. This, in part, explains the asymmetry on the polarity of sprite producing lighting strokes [*Williams et al.*, 2007]. Furthermore, sprites are produced by positive lightning strokes with unusually large charge moment changes. Remote sensing using extremely low frequency waves (ELF, 3 to 3000 Hz) radiated from lightning strokes has shown that the charge moment change required to initiate sprites to be on the order of hundreds of C km [*Cummer and Lyons*, 2005, references therein], which is an order of magnitude larger than the charge moment changes produced by normal positive lightning strokes [*Cummer and Lyons,* 2004].

As a side note, C. T. R. Wilson[†] first discussed the possibility of electric discharges in the upper atmosphere above thunderstorms in the 1920s. He noted that the breakdown threshold decreases more rapidly with altitude than the thundercloud field which is essentially a dipole

[†]Although C. T. R. Wilson is perhaps best known for his invention of cloud chamber, for which he was awarded the Nobel Prize in physics in 1927, his contributions to the study of atmospheric electricity are both abundant and diverse. A good short piece of writing on his biography is found in [*Williams*, 2010].

electric field, and remarked, "if the electric moment of a cloud is not too small, there will be a height above which the electric force due to the cloud exceeds the sparking limit." [*Wilson*, 1924]. Although his theory does not incorporate the finite conductivity of the atmosphere, which in part determines the transient nature of sprites, it remarkably grasps the underlying physics.

1.2 Formation and Development of Sprites

Immediately after the initial breakdown, sprites rapidly develop in the altitude range of 40 to 90 km, typically within a few ms. Such dynamic nature of sprites can not be resolved at normal video frame rate of 30 frames per seconds (fps), at which sprites are adequately portrayed as gigantic flashes. In an effort to resolve the formation and development of sprites, imaging observation has been progressively made at higher frame rates.

Sprites develop in a form of filamentary structures, called "streamers". The term was introduced after their similarities to streamer discharges was recognized. [*Pasko et al.*, 1998]. This will be discussed in the next section. Streamers have narrow filamentary channels with transverse size ranging from a few tens to hundreds of meters [*Gerken et al.*, 2000]. They initially develop at 70 to 90 km altitude and propagate both downward and upward [*Stanley et al.*, 1999]. As they propagate, they frequently split into narrower streamers, creating complex, tendril-like structures in video imagery (Figure 1.3).

Streamers develop very rapidly: the upward and downward motion of streamers typically proceeds at a speed of 10^6 to 10^7 m s^{-1} [*Stanley et al.*, 1999]. Their true nature can only be documented with high-speed imaging observations. Early high-speed observations made at up to 4000 fps showed that sprites start with propagating streamers, but, at the same time, the data clearly indicated that yet higher frame rates would be required to resolve details of their development [*Stanley et al.*, 1999; *Stenbaek-Nielsen et al.*, 2000; *Moudry et al.*, 2002].

Recent high-speed observations made at 10 000 fps and higher resolved much greater details than had been possible with the earlier observations [*McHarg et al.*, 2007; *Stenbaek-Nielsen et al.*, 2007]. These studies showed that the propagating streamers indeed have no visible bodies but have compact luminous fronts. The luminous streaks, so clearly identifiable in the earlier images, were produced by the fast-moving fronts as a result of insufficient temporal resolution, much like "a nighttime long time exposure photograph of a highway where lights on moving cars form long streaks in the image" [*Stenbaek-Nielsen and McHarg*, 2008]. The effects of higher frame rates are illustrated in Figure 1.4, with images of the same sprites recorded at

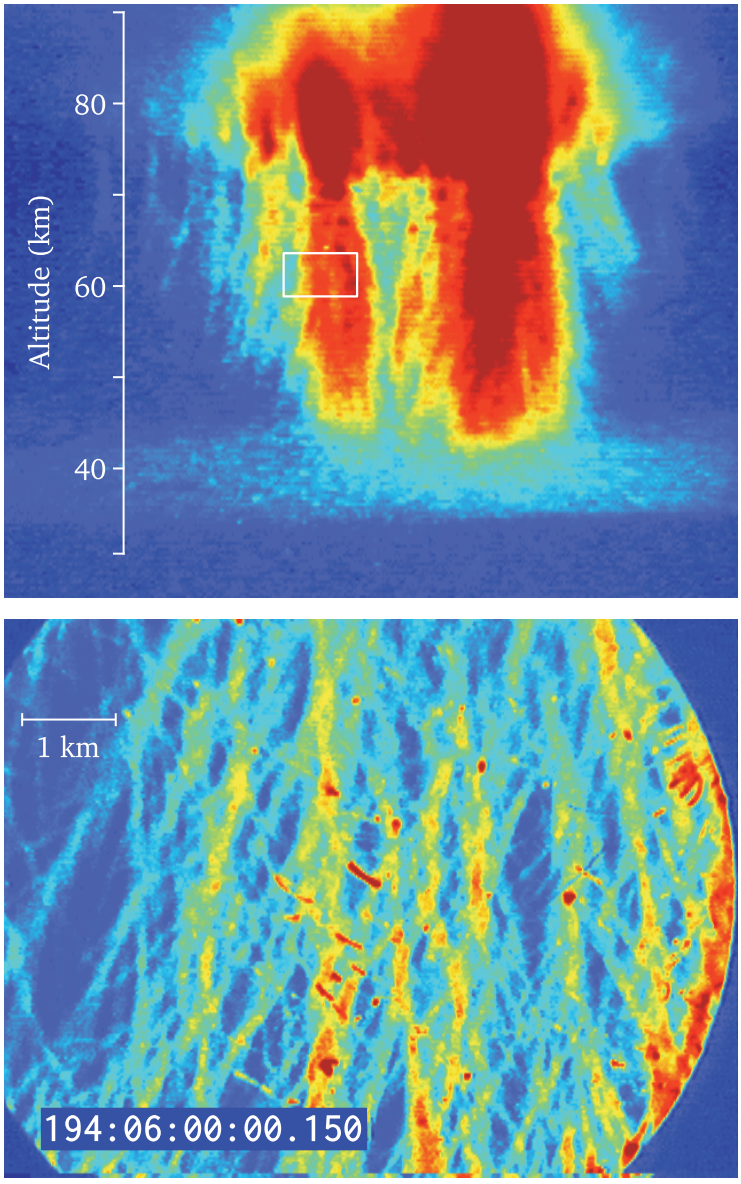

Figure 1.3. Fine scale structures in sprites. The top and bottom images were simultaneously observed by two imagers with different field of views; a box in the wide field of view (top) shows the narrow field of view (bottom). The large structures of sprites are composed of fine scale structures with transverse sizes ranging from a few tens to hundreds of meters. The false-colored images were reproduced from [*Gerken et al.*, 2000].

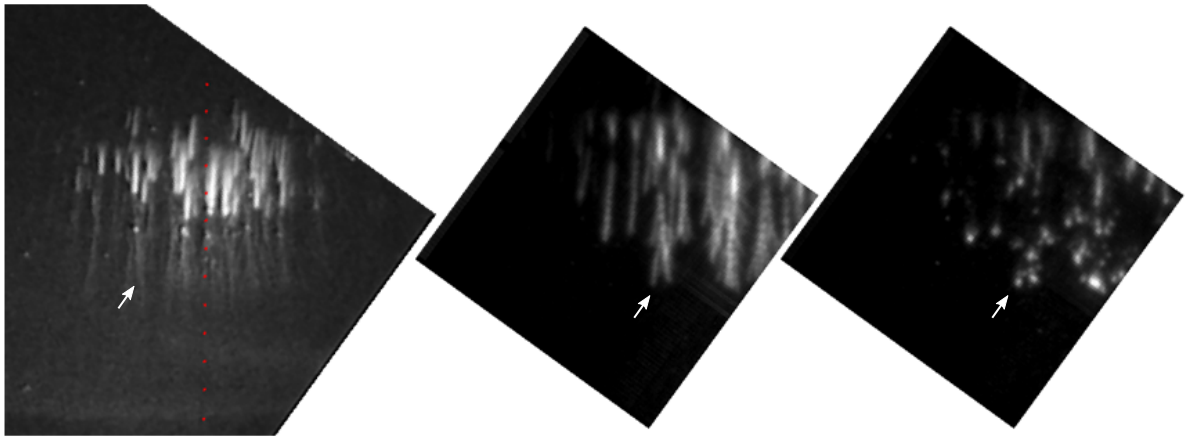

33 ms 1 ms 0.05 ms

Figure 1.4. Sprites recorded at different frame rates. The three images illustrate the same sprites recorded with different frame rates, 30, 1000 and 10 000 fps. Note that the 10 000 fps image was recorded with a 50 μs exposure. The images were reproduced from [*Stenbaek-Nielsen and McHarg*, 2008].

different frame rates: 30, 1000 and 10 000 fps.

Typical development of a sprite as observed at at 10 000 fps or higher is illustrated in Figure 1.5. A sprite initiates with the development of a downward propagating streamer. The streamer appears at 70 to 90 km altitude out of dark background or from inhomogeneities at the bottom of a sprite halo, which is another type of TLE often preceding sprites [*Cummer et al.*, 2006]. The streamer moves vertically downward and becomes faster and brighter as it descends. The propagation continues for roughly 5 to 10 km, and then the streamer split into narrower streamers. They continuously propagate and split; the subsequent propagation and splitting repeatedly occurs and spawns narrower and narrower streamers [*McHarg et al.*, 2010]. These streamers slow down as they descend and eventually fade at the terminal altitude of about 40 km [*Li and Cummer*, 2009].

After the initial downward propagating streamer rapidly moves through the atmosphere, a faint luminous trail forms in the wake. The initial streak becomes brighter and appears to expand both upward and downward following the path of the initial streamer. The expansion does not proceed very far; the upward expansion may go as far as a few km higher than the onset altitude of the streamer, and the downward expansion may reach the point where the streamer splits but rarely continues further. Hence, the initial streak grows into a columnar glow with a height of roughly 5 to 10 km. In contrast to the rapidly moving streamers, the

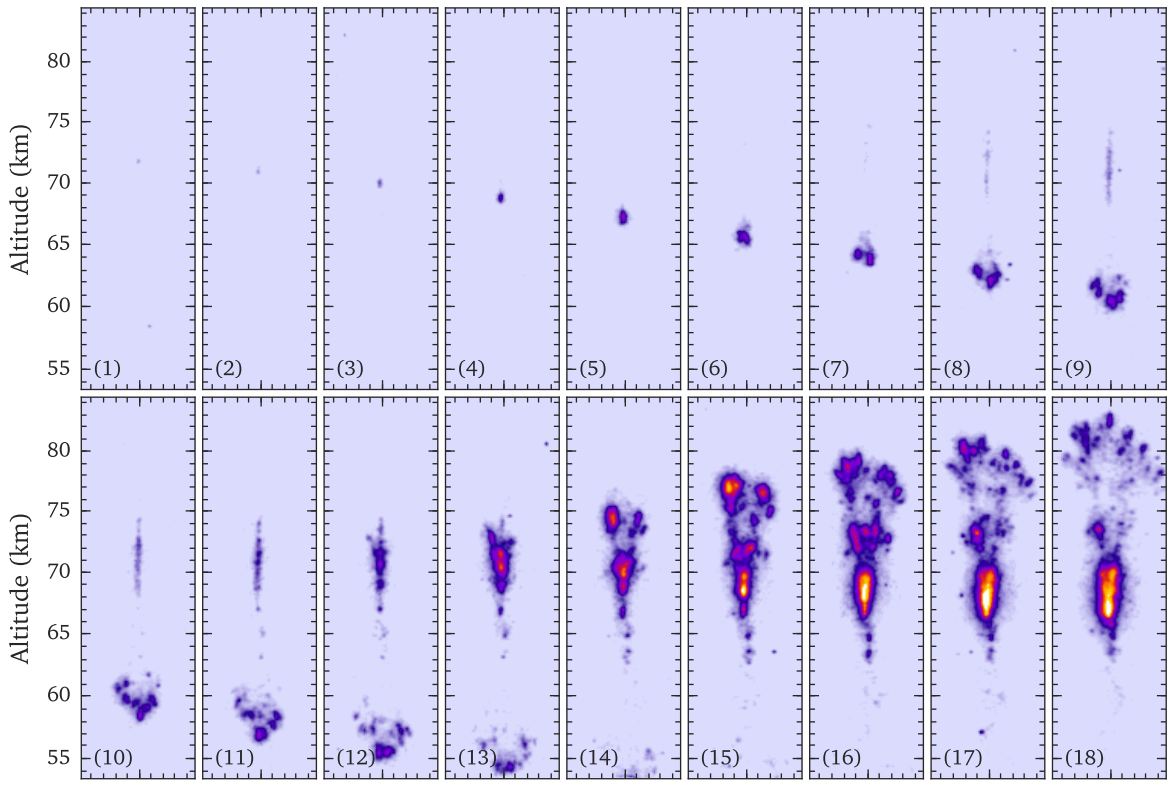

Figure 1.5. Typical development of a sprite. Consecutive images were recorded at 10 000 fps with a 50 μs exposure starting at the beginning of the integration time, and were false-colored to enhance the visual dynamic range.

columnar glow is more or less stationary.

As the columnar glow forms, upward propagating streamers may develop. They start from existing structures in the column glow, and move rapidly upward with a significant horizontal velocity component. They move as fast as the downward propagating streamers, though the upward propagating streamers have been observed to be slightly faster [*McHarg et al.*, 2007]. They initially have sizes comparable to that of the initial downward propagating streamer, but they quickly become larger as they propagate and often terminate with a "puff" much like fireworks leaving a diffusive patch of emission [*Stenbaek-Nielsen and McHarg*, 2008]. They also split, but not as prolifically as the downward propagating streamers [*Cummer et al.*, 2006].

The initial active phase with the dynamic development of the streamers is followed by a quiescent phase during which the columnar glow and other features slowly decay with little apparent motion. While the active phase is very short, typically a few milliseconds, the quiescent phase is much longer persisting for 10 to 100 ms [*Stenbaek-Nielsen and McHarg*, 2008]. The most prominent feature in the quiescent phase is the columnar glow. It is more or less stationary

and slowly decays in 10 to 100 ms. Another type of feature identifiable in the quiescent phase is called "bead". The beads tend to form where preceding streamers split and have lentil-like shape with size ranging from a few tens to hundreds of meters [*Gerken et al.*, 2000]. These fine-scale structures are also stationary and persist even longer than the columnar glow.

Time integration of the optical emissions from the streamers and other features collectively produce a gigantic flash with distinct structures along the vertical extent. The relatively long-lived optical emission from the columnar glow provides the major source of the luminosity and results in a bright, central body. The frequently splitting downward propagating streamers produce faint, tendril-like filamentary structures extending downward from the bottom of the body (Figure 1.3). The upward propagating streamers produce branch-like structures protruding upward from the body and the puffs at their termination produce diffusive tops spreading from the top of the body.

1.3 Streamer Discharges and Their Similarities to Sprites

As mentioned in the previous section, sprite streamers were named based on their similarities to streamer discharges—a type of transient electric discharges observed in laboratory experiments. The relevance of sprite observations to laboratory discharge studies, and vice versa, has been pointed out by *Pasko* [2007] and by *Ebert et al.* [2010].

At ground pressure, when a high voltage pulse is applied to a gap between electrodes, electric breakdown may occur, typically proceeding in a form of filamentary plasmas, called streamers. Streamers are narrow channels of weakly ionized plasmas driven by nonlinear ionization waves with transverse size ranging from 10^{-2} to 10^{-1} cm [*Bazelyan and Raizer*, 1998, p. 48]. They develop from an electrode and rapidly propagate toward the other electrode at a speed of 10^5 to 10^7 m s^{-1} [*Bazelyan and Raizer*, 1998, p. 48]. They frequently branch into narrower streamers and create tree-like structures in the gap. After bridging the gap, the weakly ionized channels may evolve into spark leaders, which are strongly ionized channels. Streamer discharges often occur as precursors to spark discharges, such as lightning [*Bazelyan and Raizer*, 1998, p. 87].

Streamer discharges observed in laboratory experiments are illustrated in Figure 1.6. These images shows streamers emerging from a point anode at the upper left corner and extending toward a plate cathode at the bottom at different exposures. The true nature of the streamers becomes clearer at shorter exposures; while the leftmost image with a 300 ns exposure shows filamentary channels extending between the electrodes, the rightmost image with a 1 ns exposure shows no visible channel but compact heads of the channels, clearly indicating that the optical

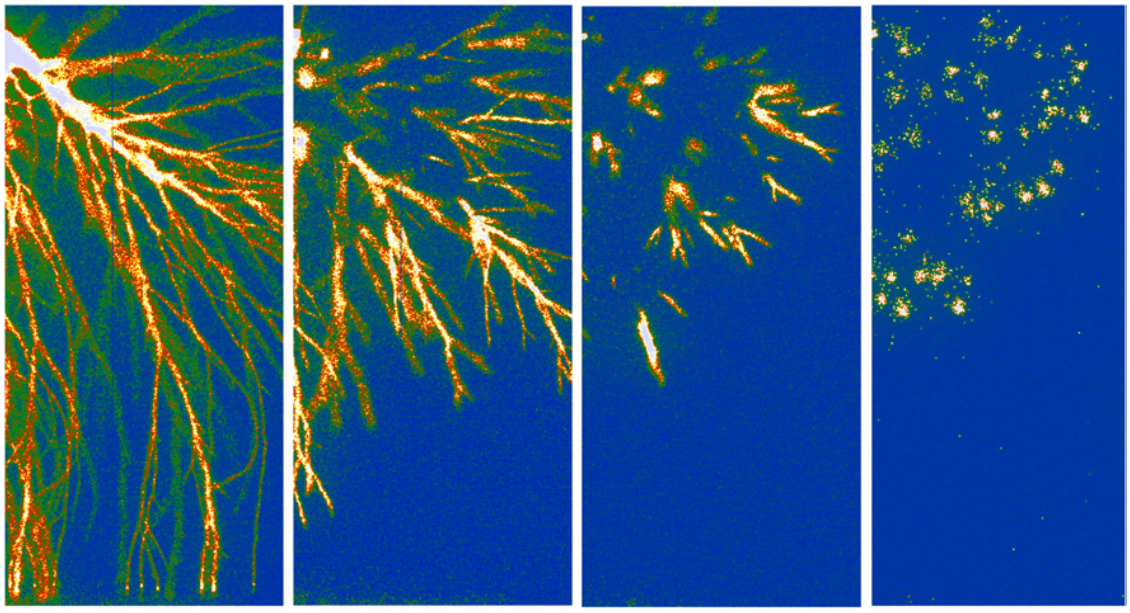

Figure 1.6. Laboratory streamers recorded at different exposures of 300, 50, 10, and 1 ns. The streamers were produced in air at ground pressure in a 4 cm gap between a point anode at the top left corner and a plate cathode at th the bottom. Actual time intervals are shown in the parentheses. The images are reproduced from [*Ebert et al.*, 2006].

emissions from the streamers are concentrated in the fast-moving streamer heads. The luminous streaks identifiable in the images with a 10 ns exposure and longer are, in fact, the traces of the fast-moving streamer heads during the exposure times.

The concentration of optical emissions arises from a unique charge structure of a streamer that causes intense electron impact ionization of the ambient gas in its head. The body of a streamer is a narrow channel of weakly ionized plasmas. The channel with finite conductivity induces a space charge layer surrounding it, and the space charges screen the interior from the background electric field. Hence, the electric field in the streamer channel is weak and produces no substantial ionization or excitation of neutral species. But the charge structure at the tip of the channel is different from the rest. A thin layer of space charges at the tip is strongly curved and therefore significantly enhances the electric field just ahead of it. The electric field becomes much greater than the background field—exceeding the breakdown threshold many times over—and produces intense electron impact ionization of neutral species in the streamer head.

The space charge layer in the streamer head forms the ionizing front of a nonlinear ionization

wave and plays a crucial role in the streamer propagation. The intense ionization quickly raises the densities of electrons and ions from the ambient level to that comparable to those in the streamer channel. This leads the streamer channel to extend and the space charge layer to advance while maintaining its charge structure. Hence, the space charge layer forms the ionizing front of a nonlinear ionization wave. The presence of the space charge layer allows streamers to propagate in the region where the background field is too weak to maintain ionization, i.e., below the breakdown threshold. The minimum strength of the background field required for stable propagation of streamers in air has been reported to be about seven times lower than the breakdown threshold [*Allen and Ghaffar*, 1995].

The space charge layer induces not only ionization but also dissociation and excitation of neutral species by electron impact, producing chemically active species that can initiate complex chemical reactions. Because of the ability to generate the chemically active species, streamer discharges have been used in industrial applications such as ozone production and pollution control [*Nijdam*, 2011, references therein].

Similarities between sprite streamers and laboratory streamers are easily identifiable in their visual characteristics. Both types of streamers form frequently branching, filamentary channels. The visual characteristics of sprite streamer channels (Figure 1.3) and that of laboratory streamer channels (Figure 1.6) are similar. Another indication of their similarity is that both types of streamers have no visible channels but have luminous, compact, fast-moving heads. The concentration of optical emissions in sprite streamer heads (Figure 1.4) and that in laboratory streamer heads (Figure 1.6) are also similar. Furthermore, recent sprite observations with high spatial and temporal resolution revealed that the shape of sprite streamer heads remarkably resembles that of laboratory streamer heads (Figure 1.7).

Although they are apparently similar, their length and time scales are vastly different. Their diameters are greatly different; while the diameter of sprite streamers is a few to hundreds of meters, that of laboratory streamers is 10^{-2} to 10^{-1} cm. Their time scales are also greatly different; for example, the streamers in Figure 1.7 appear quite similar, but the sprite streamer and the laboratory streamer were recorded with a exposure of 200 μs and 300 ps, respectively. Hence, the length and time scales of sprite streamers are larger than those of laboratory streamers by a factor of 10^5.

The apparent similarities, but with different length and time scales, have been interpreted in terms of similarity laws for streamer discharges. Streamer discharges in gases with the same composition, but with different densities can be physically similar, meaning that the discharge

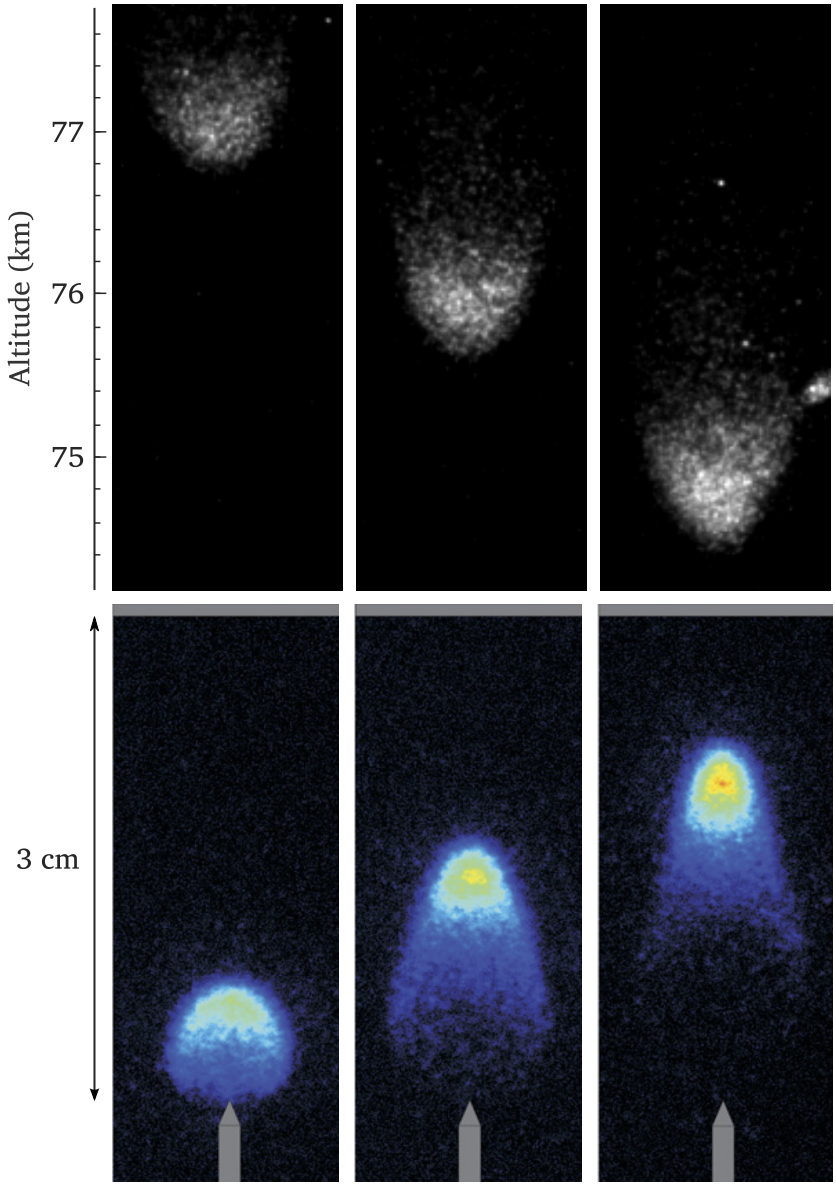

Figure 1.7. Streamer heads observed in sprites and in laboratory experiments. (top) Three successive images of a large sprite streamer recorded at 16 000 fps with 20 μs exposure. The diameter of the steamer is about 500 m. The images were reproduced from [*Stenbaek-Nielsen et al.*, 2013]. (bottom) Three successive images of a positive laboratory streamer recorded 5 ns apart with a 300 ps exposure. The streamer was produced in air at 460 Torr between a 3 cm gap with an applied voltage of 38 kV. The diameter of the streamer is 4 to 6 mm. The images were reproduced from [*Nudnova and Starikovskii*, 2008].

characteristics—length and time scales, velocity, etc.—are scaled with the gas density N, and the scaled characteristics are otherwise same [*Pasko*, 2007; *Ebert et al.*, 2010]. In any type of electric discharges, the fundamental process is electron impact ionization of neutral species [*Bazelyan and Raizer*, 1998, p. 43]. While the energies required to ionize neutral species are independent of N, the electron-neutral collision frequency is proportional to N, indicating that the energies gained by electrons over the mean free path are inversely proportional to N. Therefore, one should expect that the discharge characteristics are somehow scaled with N. The set of the density dependent scales are often referred as the similarity laws.

The observations of similarities are indeed consistent with the similarity laws: the length scale and time scale are scaled as N^{-1}, and the speed is independent of N [*Ebert et al.*, 2010]. As mentioned earlier, the length scale and time scale of sprite streamers are larger than those of laboratory streamers by a factor of 10^5. The observed increase is—according to the U.S. Naval Research Laboratory Mass Spectrometer and Incoherent Scatter Radar model (NRLMSISE-00) [*Hedin*, 1991]—roughly equivalent to the reduction of the air density at 80 km altitude from the ground, which agrees with the similarity laws. Furthermore, the speed of sprite streamers (10^6 to $10^7\,\mathrm{m\,s^{-1}}$) and that of laboratory streamers (10^5 to $10^7\,\mathrm{m\,s^{-1}}$) are roughly same regardless of the different ambient air densities, which also agrees with the similarity laws.

The observed similarities conforming with the similarity laws strongly indicate that sprites are scaled analogs of streamer discharges in laboratory experiments. Both experimental and modeling studies of the laboratory discharges have provided many insights in interpretation of sprite observations [*Pasko*, 2007, references therein]. Conversely, sprite observations may provide new insights in our understanding of streamers in laboratory experiments, particularly their dynamics. According to the similarity laws, "a decrease of gas density acts as magnifying glass and slow motion player" [*Ebert et al.*, 2010]. Hence, sprite observations may be able to resolve great details of streamer dynamics that are very difficult to do in laboratory experiments due to the limitation of current imaging technologies.

1.4 Optical Emissions From Sprites

1.4.1 Identification of Nitrogen Band Emissions

The optical emissions from sprites consist of the emissions from molecular band systems of nitrogen—the spontaneous emissions associated with transitions between vibrational levels in different electronic states of the molecule. Observations have identified the nitrogen band

emissions in wavelength ranges from the far ultraviolet to near infrared, and the identification of the emissions from ionized nitrogen has provided direct evidence of ionization in sprites. Moreover, studies have indicated that the emissions are primarily excited by electron impact of nitrogen molecules.

The predominant red emission from sprites mainly consists of the visible and near infrared emission from the N_2 First Positive system. The First Positive system is associated with the transitions from vibrational levels in the upper electronic state designated $B\,^3\Pi_g$ to those in the lower electronic state designated $A\,^3\Sigma_u^+$, and is often denoted as $B\,^3\Pi_g \rightarrow A\,^3\Sigma_u^+$. During the summer of 1995, *Mende et al.* [1995] and *Hampton et al.* [1996] made the first ground-based spectral observations in the visible and near infrared. These studies identified that the predominant red emission to be produced by the First Positive system. Their findings have been confirmed by subsequent ground-based spectral observations [*Morrill et al.*, 1998; *Heavner*, 2000; *Bucsela et al.*, 2003]. In a follow-up study, *Green et al.* [1996] showed that the first spectral data are consistent with electron impact excitation of nitrogen molecules, indicating the presence of free electrons with energies at least 7.4 eV, the excitation threshold energy of the First Positive system.

The blue emission from sprites consists of the near ultraviolet and blue emissions from the N_2 Second Positive ($C\,^3\Pi_u \rightarrow B\,^3\Pi_g$) and the $N_2{}^+$ First Negative ($B\,^2\Sigma_u^+ \rightarrow X\,^2\Sigma_g^+$) systems. The Second Positive and the First Negative systems have the excitation threshold energies of 11.0 and 18.8 eV, respectively; both are substantially higher than the excitation threshold energy of the First Positive system. *Armstrong et al.* [1998] and *Suszcynsky et al.* [1998] made the first ground-based photometric observations in the near ultraviolet and blue. These studies identified the Second Positive emission, but the wide passband used in the measurements did not allow unambiguous identification of the First Negative band emission. The First Negative emission, a direct evidence of ionization in sprites, was first identified by subsequent ground-based photometric observations made by *Armstrong et al.* [2000]. The Second Positive and the First Negative emissions have been confirmed by years of spaceborne photometric observations using a multi-instrument payload called Imaging of Sprites and Upper Atmospheric Lightning (ISUAL) onboard a Taiwanese satellite, FORMOSAT-2 [*Kuo et al.*, 2005, 2008; *Liu et al.*, 2006].

The Second Positive and the First Negative systems, however, have not been fully confirmed by spectral observations. The emissions in the shorter wavelengths are difficult to measure from ground-based platforms, which have been commonly used in spectral observations. Ground-based observations typically involve long lines of sight—hundreds of kilometers—in the dense

Table 1.1. Summary of nitrogen band emissions from sprites.

Band system	Transition	Spectral range	Lifetime[a]	Threshold energy[b]	Quenching altitude[c]
N_2 First Positive	$B\,^3\Pi_g \rightarrow A\,^3\Sigma_u^+$	visible and near IR	8 µs	7.4 eV	65 km
N_2 Lyman–Birge–Hopfield	$a\,^1\Pi_g \rightarrow X\,^1\Sigma_g^+$	far UV	58 µs	8.5 eV	85 km
N_2 Second Positive	$C\,^3\Pi_u \rightarrow B\,^3\Pi_g$	near UV and visible	37 ns	11.0 eV	30 km
N_2^+ Meinel	$A\,^2\Pi_u^+ \rightarrow X\,^2\Sigma_g^+$	visible and near IR	12 µs	16.5 eV	85 to 90 km
N_2^+ First Negative	$B\,^2\Sigma_u^+ \rightarrow X\,^2\Sigma_g^+$	near UV and visible	62 ns	18.8 eV	50 to 55 km

[a] Radiative lifetime in vacuum [*Gilmore et al.*, 1992].

[b] Excitation threshold energy [*Cartwright et al.*, 1977].

[c] Quenching altitudes were computed with an atmospheric density profile obtained from the NRLMSISE-00 model [*Hedin*, 1991] and the rate coefficients for quenching of relevant electronic states by N_2 and O_2. The rate coefficients for the First Positive system were adopted from [*Piper*, 1988, 1992], those for the LBH system were from [*Marinelli et al.*, 1989], those for the Second Positive system were from [*Dilecce et al.*, 2006; *Pereira et al.*, 2010], those for the Meinel system were from [*Piper et al.*, 1985], and those for the First Negative system were from [*Dilecce et al.*, 2010].

lower atmosphere. Along the long paths, the emissions in the shorter wavelengths are severely attenuated by atmospheric scattering and absorption. To avoid the atmospheric attenuation, *Heavner et al.* [2010] made, in July 1998, the first airborne spectral observations in the near ultraviolet and blue. The study identified the Second Positive system in a sprite spectrum but found no distinct feature of the First Negative system. Since then, no spectral observation in the near ultraviolet and blue has been made.

Two other band emissions in sprites have been reported to date. The first is the far ultraviolet emission from the N_2 Lyman–Birge–Hopfield ($a\,^1\Pi_g \rightarrow X\,^1\Sigma_g^+$) system, which has the excitation threshold energy of 8.5 eV. Since emission in the far ultraviolet is severely absorbed by oxygen molecules in the atmosphere, the LBH emission can only be measured from space. The spaceborne photometric observations using the ISUAL instrument first reported the LBH emission in sprites [*Kuo et al.*, 2005; *Liu et al.*, 2006].

The second is the visible and near infrared emission from the $N_2{}^+$ Meinel ($A\,^2\Pi_u^+ \rightarrow X\,^2\Sigma_g^+$) system; however, its presence has been somewhat controversial. The Meinel system has the excitation threshold energy of 16.7 eV, which is slightly higher than 15.6 eV, the ionization threshold energy of nitrogen molecules. This suggests that the presence of the Meinel emission may provide further evidence of ionization in sprites. But studies have indicated that the Meinel emission is strongly quenched below 85 to 90 km altitude (Table 1.1) and should be difficult to observe in sprites. *Morrill et al.* [1998] made ground-based spectral observations and found distinct features attributable to the Meinel bands, which was later re-examined and confirmed by *Bucsela et al.* [2003]. Their findings, however, contradict the early spectral studies that found no distinct feature of the Meinel system [*Mende et al.*, 1995; *Hampton et al.*, 1996; *Green et al.*, 1996]. Nonetheless, the presence of the Meinel emission in sprites remains an open issue.

1.4.2 Implication of the Band Emissions: Sprites as Streamer Discharges

Temporal and spatial variations of relevant band emissions indicate that ionization emissions are primarily associated with sprite streamers and neutral emissions are largely associated with columnar glows, suggesting the ranking of the underlying electron energies in respective features. Moreover, the ability to ionize the ambient air emphasizes the physical similarity between sprite streamers and laboratory streamers.

The early photometric observations simultaneously recorded precise time histories of relevant band emissions using narrowband photometers. *Suszcynsky et al.* [1998] and *Armstrong et al.*

[1998] showed that ionization emissions occur impulsively at the onset, but neutral emissions persists for a longer period of time. Later, *Armstrong et al.* [2000] reported that the signals from all band emissions raise simultaneously at the onset, but the duration of each signal is different: the N_2^+ First Negative emission lasts about 140 μs, the N_2 Second Positive emission lasts about 1 ms, and finally the N_2 First Positive emission persists for a few ms or longer. These reports indicates that sprites develop roughly in two separate phases. The first occurs within the first millisecond of the onset and is associated with an energetic initiation process; the second persists for tens to hundreds of milliseconds and is associated with less energetic secondary processes induced by the initiation [*Suszcynsky et al.*, 1998].

The development in two separate phases parallels the sprite development documented by high-speed imaging studies. As discussed in Section 1.2, high-speed imaging studies have shown that sprites develop in two phases: the initial active phase within the first few ms of the onset where sprite streamers rapidly develop, and the quiescent phase persisting for 10 to 100 ms where a columnar glow slowly decay. Hence, the two separate phases associated with the emissions parallel those observed in the sprite development. This implies that the impulsive ionization emissions at the onset and the continuing neutral emissions are associated with sprite streamers and columnar glows, respectively.

The photometric observations alone, however, did not establish hard evidence of these associations. This is because the measurements did not have sufficient resolution to examine the spatial information associated with the emissions. Other types of the measurements were needed to study the spatial variations of the emissions and to test the associations presumed from the temporal variations of the emissions.

To spatially resolve relevant band emissions from sprites, *Morrill et al.* [2002] made airborne multi-color imaging observations. The observations simultaneously recorded the N_2 Second Positive and N_2^+ First Negative emissions using intensified video cameras with narrow passband filters. While the video recording limited temporal resolution, the airborne imaging with narrowband filters provided altitude profiles of the band emissions with spatial resolution improved over the previous photometric observations.

The multi-color imaging study indeed confirmed the association of the ionization emissions with sprite streamers and that of the neutral emissions with columnar glows. *Morrill et al.* [2002] reported that the N_2^+ First Negative emission is nearly constant at all altitudes, and the N_2 Second Positive emission is roughly constant in the tendrils but intensifies in the body. As mentioned in Section 1.2, the tendrils are produced by the emissions from sprite streamers,

and the body is mainly produced by the emissions from a columnar glow. Hence, the altitude profiles indicate that the First Negative emission is primarily associated with sprite streamers, and a large part of the Second Positive emission is associated with a columnar glow, confirming the associations presumed from the previous photometric observations.

Therefore, the photometric and multi-imaging observations together indicate that sprite streamers are energetic initiation processes that primarily cause ionization in sprites, trailing columnar glows are less energetic secondary processes that mainly produce the relatively long-lived neutral emissions. The excitation threshold energy of the N_2^+ First Negative system is about 8 eV higher than that of the N_2 Second Positive system and is about 11 eV higher than that of the N_2 First Positive system. Accordingly, the presence and absence of the ionization emission suggests the ranking of the underlying electron energies: the electron energy in sprite streamers is definitely higher than that in columnar glows.

The ability to ionize the ambient air emphasizes the physical similarity between sprite streamers and laboratory streamers, supporting the interpretation of sprites as streamer discharges. As the optical emissions from sprite streamers concentrate in their heads (Figure 1.7), the ionization in sprite streamers likely takes place there. As mentioned in Section 1.3, such localized ionization is also present in laboratory streamers, and it plays a crucial role in the streamer propagation and determines various characteristics of streamer discharges. The physical similarity of the localized ionization supplements the similarities between sprite streamers and laboratory streamers that are obtained from their visual characteristics and the corresponding similarity laws, supporting the interpretation of sprites as scaled analogs of streamer discharges observed in laboratory experiments.

1.4.3 Implication of the Band Emissions: Roles of Collisional Processes

Color imagery of sprites shows that they are predominantly red but their tendrils gradually merge into blue at lower altitude (Figure 1.8). The color variation implies that the ranking of processes producing excited species varies along with the vertical extent of sprites. The process mainly responsible for the color variation is collisional quenching of electronically excited species. In addition to quenching, other types of collisional processes have been noted responsible for altitude variation of observed spectral features.

The observed color variation is, in part, linked to the different electron energies in the body and tendrils. The different electron energies result in different excitation rates of excited species

Figure 1.8. Color image of sprites photographed with a digital single-lens reflex camera (courtesy of Jason Ahrns). Blue light across the bottom of the image is a lightning flash scattered above the cloud top.

in respective features. The excitation rates of the N_2 First Negative and the N_2 Second Positive systems increase with electron energy, and so does the fraction of the near ultraviolet and blue emissions from these band systems. Since the electron energy in sprite streamers is higher than that in columnar glows [*Morrill et al.*, 2002], the tendrils become more bluish than the body, which is predominantly red because of higher fraction of the visible and near infrared emission from the First Positive system. The different electron energies alone, however, do not fully account for the observed color variation.

The color variation is mainly caused by a collisional process called quenching—a process in which electronically excited species lose their energy by collision with atoms and molecules before emitting light. The effects of quenching tend to be more serious on the excited species with longer radiative lifetimes, and increase with the densities of quenching species such as N_2 and O_2, becoming severe at lower altitudes. The severity of the effects is quantified as the quenching altitude—the altitude below which the emission rate of the excited species is reduced to less than half of its unquenched value [*Vallance Jones*, 1974]. The quenching altitude of the First Positive system, which has relatively long radiative lifetime of 8 μs, is 65 km, whereas those of the Second Positive and the N_2 First Negative systems are 30 and 55 km, respectively

(Table 1.1). Therefore, while the blue and near ultraviolet emissions from the N_2 Second Positive and N_2^+ First Negative systems remain intact at lower altitudes, the visible and near infrared emission from the First Positive system is severely reduced below 65 km altitude.

In addition to quenching, other types of collisional processes have been noted responsible for observed variation in spectral features. *Heavner* [2000] examined the N_2 First Positive spectra obtained from different sprites and reported that the relative intensities of the vibrational bands vary with altitude. The band intensities are directly linked to the vibrational distribution of the upper electronic state, the N_2 ($B\,^3\Pi_g$) state. *Bucsela et al.* [2003] examined two First Positive spectra obtained from the same sprite but from different altitudes and reported that the two spectra have different vibrational distributions, which is consistent with the altitude variation reported by *Heavner* [2000]. *Bucsela et al.* [2003] showed that the vibrational distribution from the lower altitude spectrum is similar to that observed in laboratory afterglow, implying that some emissions from the First Positive system are excited by collisional processes involving vibrationally excited N_2 ground state and the low-lying metastable N_2 ($A\,^3\Sigma_u^+$) state.

1.5 Thesis Outline

The previous observations have provided insights into the processes associated with the optical emissions from sprites, but these measurements had their limitations. The previous spectral observations did not have sufficient temporal resolution; they integrated the emissions over at least 17 ms and did not allow an examination of the temporal variation of the emissions. Moreover, they recorded spectra from single altitudes and did not examine the spatial variation of the emissions. The previous photometric observations did not have sufficient spatial resolution; although they had sufficient temporal resolution, they integrated the emissions from ranges of altitudes and did not distinguish the emissions from the individual structures.

To overcome some of the limitations, we have developed two different types of spectrographs with resolution improved over the previous observations. The first is an intensified CCD imaging slit spectrograph. It records spectra in the visible and near infrared at a frame rate of up to 1000 fps and has a spectral resolution of about 3 nm. Although the temporal resolution is only moderately high and not sufficient to resolve the sprite development, its vertically oriented slit provides altitude resolution. The second is a high-speed imaging slitless spectrograph. It records spectra in the visible and near infrared at a frame rate of 10 000 fps. Although the spectral resolution was rather coarse compared to the other spectrograph, slitless spectroscopy with the high temporal resolution provides the spectra of individual streamers and columnar

glows.

Using the data obtained with these instruments, this dissertation addresses some of the issues relevant to the optical emissions from sprites, which could not be studied with the previous observations due to the lack of sufficient resolution. These issues are summarized in the following:

(1) The presence of the Meinel emission along the vertical extent of sprites. Although ionization in sprites have been evidenced by the presence of the First Negative emission, further evidence of the ionization and some insights into the ionization process may be provided by the Meinel emission. *Morrill et al.* [1998] and *Bucsela et al.* [2003] first reported the presence of the Meinel emission in the streamer region below 60 km altitude, which is far below the quenching altitude. The presence of the Meinel emission at such low altitude implies the significant excitation of the Meinel system that exceeds the quenching effects. Such significant excitation may be caused by strong electron impact ionization in sprite streamers or by collisional energy transfer process between $N_2^+(A^2\Pi_u^+)$ and $N_2^+(X^2\Sigma_g^+)$ [*Bucsela et al.*, 2003]. Nonetheless, the data indicating the presence of the Meinel emission is very limited. Additional data covering wide ranges of altitude are required to investigate the presence and altitude dependence of the Meinel emission.

(2) The altitude variation of the $N_2(B^3\Pi_g)$ vibrational distribution. The previous spectral observations showed that the vibrational distribution varies with altitude and indicated that processes beyond electron impact excitation and simple quenching occur in sprites [*Heavner*, 2000; *Bucsela et al.*, 2003]. *Bucsela et al.* [2003] showed that the vibrational distribution below 60 km altitude is similar to ones observed in laboratory afterglow, and suggested that some emissions from the First Positive system are excited by collisional energy transfer process between vibrationally excited N_2 ground state and the low-lying metastable state. Nonetheless, the data indicating the altitude variation are very limited. Additional data covering a wide range of altitude are needed to characterize the altitude variation of the vibrational distribution.

(3) The ranking of the electron energies in sprite streamers and columnar glows. The previous photometric and multi-color imaging observations together indicate that sprite streamers are energetic initiation processes that primarily cause ionization in sprites, and trailing columnar glows are less energetic secondary processes that mainly produce the relatively

long-lived neutral emissions [*Armstrong et al.*, 2000; *Morrill et al.*, 2002]. This indicates that the electron energies in sprite streamers are higher than those in trailing columnar glows. But there have been no direct measurement of the band emissions from individual sprite streamers and trailing columnar glows.

The organization of this dissertation is as follows. Chapter 2 describes a method for producing synthetic spectra of nitrogen band systems, which was used to examine observed spectra. Chapter 3 describes ground-based observations we made in July 2007 using the high-speed slit spectrograph, and examines the observed spectra for the presence and altitude dependence of the Meinel emission and the altitude variation of the $N_2(B\,^3\Pi_g)$ vibrational distribution. Chapter 4 describes aircraft-based observations we made in August 2009 using the high-speed slitless spectrograph, and examines the observed spectra from individual sprite streamers and trailing columnar glows. Finally, Chapter 5 summarizes the results presented in this dissertation and presents suggestions for future research.

1.6 Scientific Contributions

Original contributions of this dissertation are summarized below:

(1) Contrary to the previous reports [*Morrill et al.*, 1998; *Bucsela et al.*, 2003], no or little indication of the N_2^+ Meinel system was found in the observed spectra. To investigate the presence and altitude dependence of the Meinel bands, we made ground-based observations using the slit spectrograph and observed spectra along the vertical extent of sprites. The observed spectral features were primarily composed of the First Positive system, and the signals from the Meinel bands were determined to be below or comparable to the noise level. Based on the noise levels, the population of $N_2^+(A^2\Pi_u^+, v = 2)$ was inferred to be at most 3 to 7% of $N_2(B\,^3\Pi_g, v = 2)$

(2) The $N_2(B\,^3\Pi_g)$ vibrational distribution was confirmed to vary with altitude and to become similar to ones observed in laboratory afterglow at lower altitudes. The vertically resolved spectra showed that the band intensities of the First Positive system vary with altitude. The spectral analysis determined that the vibrational distribution varies with altitude and becomes similar to ones observed in laboratory afterglow at lower altitudes. The altitude variation indicates that the secondary collisional interactions among excited species may play a role in exciting the First Positive system. This study investigated the vibrational

distribution over a wide range of altitude compared with previous studies and provided further characterization of the altitude variation.

(3) A new technique for recording the spectra of individual sprite streamers and trailing columnar glows was developed. High-speed imaging observations showed that sprite streamers are small and essentially point sources in typical viewing geometries. To record the spectra of individual sprite streamers, we designed and built a high-speed imaging slitless spectrograph. Slitless spectroscopy is a classical technique commonly used in astronomy for recording spectra of stars and meteors; for such point sources, a grating in front of a camera lens just works as a spectrograph without a slit or a collimating unit. Using the high-speed slitless spectrograph, we have documented the spectra of individual sprite streamers and columnar glows at an unprecedented frame rate of 10 000 fps.

(4) The ranking of the electron energies in sprite streamers and columnar glows was unambiguously determined. To investigate the electron energies in respective features, we made aircraft-based observations using the high-speed slitless spectrograph. The observed spectral features were identified to be the First Positive system in the visible and near infrared and the Second Positive system in the ultraviolet and blue. The data showed that sprite streamers consistently have a larger fraction of blue emission than columnar glows, clearly indicating that the electron energies in the streamers exceed those in the glows. The observations unambiguously confirmed the more energetic nature of sprite streamers than columnar glows, which had not been possible with the previous observations.

Parts of the results presented in this dissertation have been published in peer-reviewed journals. A large part of the results presented in Chapter 3 was published in

> Kanmae, T., H. C. Stenbaek-Nielsen, and M. G. McHarg (2007), Altitude resolved sprite spectra with 3 ms temporal resolution, *Geophys. Res. Lett.*, *34*(7), L07810.

The high-speed slitless spectrograph was first used in ground-based observations in June 2007. These preliminary observations successfully recorded spectra of individual sprite streamers and columnar glows, and the results were published in

> Kanmae, T., H. C. Stenbaek-Nielsen, M. G. McHarg, and R. K. Haaland (2010a), Observation of sprite streamer head's spectra at 10,000 fps, *J. Geophys. Res.*, *115*, A00E48.

The ground-based spectral observations, however, recorded no blue emission because of severe atmospheric attenuation. To minimize atmospheric attenuation, we made an aircraft-based spectral observations in August 2009. The results are presented in Chapter 4, and a large part of the results were published in

> Kanmae, T., H. C. Stenbaek-Nielsen, M. G. McHarg, and R. K. Haaland (2010b), Observation of blue sprite spectra at 10,000 fps, *Geophys. Res. Lett.*, *37*, L13808.

Relevant work has also been published in:

> Kanmae, T., H. C. Stenbaek-Nielsen, M. G. McHarg, and R. K. Haaland (2012), Diameter-speed relation of sprite streamers, *J. Phys. D: Appl. Phys.*, *45*(26), 275203.

Chapter 2
Spectral Analysis

In order to examine observed spectra, I have developed a method for producing synthetic spectra. It was designed to simulate the shapes of observed vibrational bands of the nitrogen band systems. The shapes of the vibrational bands are produced by computing the individual rotational lines of the vibrational bands and by taking into account the effects of the atmospheric attenuation for a given viewing geometry. The attenuated features are then convolved with a function representing the instrument broadening. The resulting spectra were compared with observed spectra and were used for identifying the band systems and determining the vibrational distributions and the rotational temperatures. In this chapter, I describe models for computing the rotational lines of molecular bands and the effects of the atmospheric attenuation.

2.1 Electronic Spectroscopy of Diatomic Molecules

In this section, I briefly introduce fundamental concepts and various nomenclatures in the electronic spectroscopy of diatomic molecules, which are essential for computing the rotational lines of molecular bands. The material presented here is based on a seminal book on the molecular spectroscopy of diatomic molecules written by G. Herzberg [*Herzberg*, 1950].

2.1.1 Born–Oppenheimer Approximation

In a diatomic molecule, the electrons rapidly orbit around the two atomic nuclei, and the nuclei slowly move back and forth along the internuclear axis. These electrons and nuclei interact with each other via electrostatic forces of similar magnitude. But, since the nuclei are about four orders of magnitude heavier than the electrons, the electrons move much faster than the nuclei. Empirical observations show that while the nuclei motion takes place on a time scale of 10^{-13} s, the electronic motion takes place on a much shorter time scale of 10^{-15} s [*Brown*, 1998, p. 68].

The large separation of time scales indicates that the molecular motion can be separated into an electronic and a nuclear part. The electrons move rapidly and instantaneously follow the nuclear motion. Therefore, the electronic motion can be treated as if the nuclei were fixed, indicating that the electronic energy—the sum of the potential and kinetic energies of the individual electrons—changes as a function of the internuclear distance as the nuclei oscillate. It follows that the nuclei in motion must compensate not only the work against the electrostatic

repulsion of the nuclei, but also the work necessary for the change in the electronic energy. Therefore, the nuclear motion can be treated as if the nuclei were within an effective potential energy—the sum of the electrostatic potential energy of the nuclei and the electronic energy. The curve representing the effective potential energy as a function of the internuclear distance are referred to as a potential curve. The potential curves for different electronic states of N_2 and N_2^+ are illustrated in Figure 2.1. As clearly shown in the figure, each electronic state is characterized by a definite potential curve.

The separation of the electronic and nuclear motion is known as the Born–Oppenheimer approximation—after its two original proponents, M. Born and J. R. Oppenheimer. The Born–Oppenheimer approximation separates the molecular Hamiltonian into an electronic and a nuclear part. Accordingly, the total wavefunction ψ is approximated by the product of the electronic ψ_e and nuclear ψ_n wavefunction:

$$\psi = \psi_e \psi_n. \tag{2.1}$$

The nuclear motion can be further separated into a vibrational and a rotational part. The nuclei not only oscillate along the internuclear axis but also change the orientation in a laboratory-fixed frame. Empirical observations show that the vibrational motion is much faster than the rotational motion; while the rotational motion takes place on a time scale of 10^{-11} s, the vibrational motion takes place on a much shorter time scale of 10^{-13} s [*Brown*, 1998, p. 68]. This indicates that the nuclei move back and forth hundreds of times for each rotational cycle. Therefore, the vibrational motion can be treated as if the molecular orientation were fixed in space; on the other hand, the rotational motion can be treated as if the internuclear separation were at an averaged value.

The separation of the vibrational and rotational motion provides an extension of the Born–Oppenheimer approximation, separating the nuclear Hamiltonian into a vibrational and a rotational part. Accordingly, ψ_n is approximated by the product of the vibrational ψ_v and rotational ψ_r wavefunction. As a result, the total wave function ψ is approximated as the product of ψ_e, ψ_v, and ψ_r:

$$\psi = \psi_e \psi_v \psi_r. \tag{2.2}$$

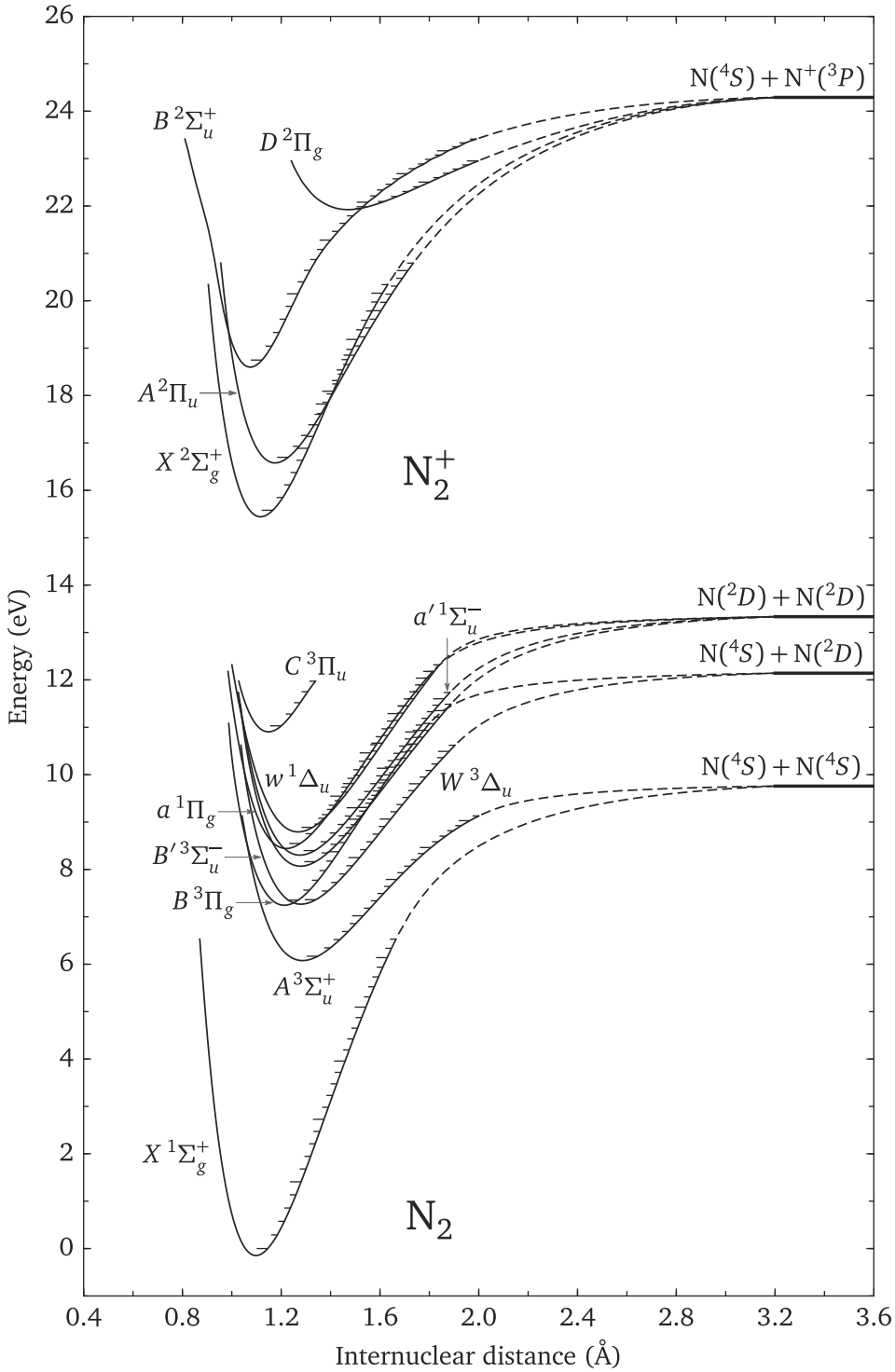

Figure 2.1. Potential energy curves for N_2 and N_2^+. Each curve represents the sum of the electrostatic potential energy of the nuclei and the electronic energy as a function of the internuclear distance, and defines the potential energy for vibrational motion of the nuclei. The vibrational energy levels are shown as tick marks within respective curves.

2.1.2 Total Energy and the Hierarchy of Energy Levels

In consequence of the Born–Oppenheimer approximation (Equation 2.2), the total internal energy of a diatomic molecule is given by a sum of energies associated with the three types of motion:

$$E = E_{\mathrm{e}} + E_{\mathrm{v}} + E_{\mathrm{r}}. \tag{2.3}$$

This form is of course only an approximation, but it is indeed a very good approximation in the vast majority of cases [*Brown*, 1998, p. 10]. In general, the electronic energy E_{e} is much larger than the vibrational energy E_{v}, and the vibrational energy is much larger than the rotational energy E_{r}. The ranking of energies produces a familiar hierarchy of energy levels: each electronic state supports a series of vibrational energy levels, and each vibrational level, in turn, owns a set of many rotational levels. Figure 2.1 shows vibrational energy levels as tick marks within each potential curve. Rotational energy levels are not shown because their intervals are too small to be shown in the figure.

In spectroscopy, energy is conventionally expressed in a quantity known as a term value, which is obtained by dividing energy by the product of the Planck constant h and the speed of light c. Term values have a dimension of wavenumber, normally expressed in units of cm^{-1}. Hence, Equation 2.3 is alternatively written as

$$\begin{aligned} T &= \frac{E_{\mathrm{e}} + E_{\mathrm{v}} + E_{\mathrm{r}}}{hc} \\ &= T_{\mathrm{e}} + G + F \end{aligned} \tag{2.4}$$

where T_{e}, G, and F are called the electronic, vibrational, and rotational term values, respectively. The electronic term value T_{e} corresponds to the electronic energy at the minimum of the potential curve where the internuclear distance is in equilibrium.

The vibrational term value G is given as a function of the vibrational quantum number v. In a first order approximation, the vibrational motion can be modeled as that of a harmonic oscillator, whose term value takes a familiar form of

$$G^{(1)}(v) = \omega_{\mathrm{e}}\left(v + \frac{1}{2}\right) \tag{2.5}$$

where ω_{e} is called the vibrational constant. But the vibrational motion actually deviates from

that of a harmonic oscillator, which is evidenced by that the potential curves in Figure 2.1 are not exactly parabolic. The energy levels of such an anharmonic oscillator are well approximated by a power series of $(v+\frac{1}{2})$. Accordingly, the vibrational term value is given as

$$G(v) = \omega_e(v+\frac{1}{2}) - \omega_e x_e(v+\frac{1}{2})^2 + \omega_e y_e(v+\frac{1}{2})^3 + \cdots \tag{2.6}$$

where ω_e, $\omega_e x_e$, $\omega_e y_e$, $\cdots$ are called the vibrational constants. These constants are unique to each electronic state.

The rotational term value F is in general given as a function of the rotational quantum number J that corresponds to the total angular momentum of a molecule. In a first order approximation, the rotational motion can be modeled as that of a rigid rotator, whose term value takes a familiar form of

$$F^{(1)}(J) = BJ(J+1) \tag{2.7}$$

where B is the rotational constant, which is inversely proportional to the moment of inertia of the molecule. But the bond between the two nuclei is actually not infinitely stiff; as the molecule rotates faster, the nuclei separate further, increasing the moment of inertia and thus reducing the rotational constant. The term value of such an non-rigid rotator are well approximated by introducing a term that accounts for the centrifugal distortion effect:

$$F^{(2)}(J) = BJ(J+1) - DJ^2(J+1)^2 + \cdots \tag{2.8}$$

where D is called the centrifugal distortion constant. Furthermore, in an actual molecule, B and D slightly change with the vibrational quantum number v. This is because the vibrational motion takes place hundreds of times for each rotational cycle, and the bond length under consideration is an average over the vibrational motion. Accordingly, the rotational term value is given in a form of

$$F(J) = B_v J(J+1) - D_v J^2(J+1)^2 + \cdots . \tag{2.9}$$

The rotational constant B_v and the centrifugal distortion constant D_v are given by

$$B_v = B_e - \alpha_e(v+\frac{1}{2}) + \gamma_e(v+\frac{1}{2})^2 + \cdots \tag{2.10}$$

$$D_v = D_e - \beta_e(v+\frac{1}{2}) + \cdots \tag{2.11}$$

where B_e, D_e, α_e, β_e, γ_e, $\cdots$ are called the spectroscopic constants. These constants are unique to each electronic state.

2.1.3 Classification of Electronic States

As shown in Figure 2.1, each molecule has a number of electronic states, and each electronic state has a definite potential curve. In addition to the potential curve, each electronic state is characterized by the quantum numbers and the symmetry properties of the electronic eigenfunction. These properties are encoded in what is known as the spectroscopic term symbol.

One of the quantum numbers used to characterize the electronic states is the quantum number Λ that corresponds to the projection of the electronic orbital angular momentum along the internuclear axis. In an diatomic molecule, electrons move in a cylindrically symmetric electrostatic field, which is produced by the charge distribution in the cylindrically symmetric environment. The electric field strongly couples the orbital motion of the electrons with the internuclear axis in such a way that the orbital angular momentum $\boldsymbol{L}$—a resultant formed by the orbital angular momenta of the individual electrons—precesses about the internuclear axis (Figure 2.2a). Because of the strong coupling, only the projection of $\boldsymbol{L}$ along the internuclear axis is a constant of the motion and therefore a well-defined quantity. The axial component is conventionally designated $\boldsymbol{\Lambda}$, and the corresponding quantum number

$$\Lambda = 0,\ 1,\ 2,\ \cdots \tag{2.12}$$

is one of the quantum numbers used to characterize the electronic states.

All electronic states with $\Lambda > 0$ are doubly degenerate; the twofold degeneracy is called the Λ-type doubling. It comes from that the molecular system has the same energy regardless of whether the orbital motion of the electrons is clockwise or counterclockwise about the internuclear axis. In contrast, electronic states with $\Lambda = 0$ have no orbital motion of the electrons; therefore, they are not degenerate.

Another quantum number used to characterize the electronic states is the quantum number S that corresponds to the electronic spin $\boldsymbol{S}$, which is a resultant formed by the spins of the individual electrons. Since the spin is not affected by an electric field, $\boldsymbol{S}$ remains a well-defined quantity in the molecule system. The electronic spin quantum number S takes either integral $(0,\ 1,\ 2,\ \cdots)$ or half-integral $(1/2,\ 3/2,\ 5/2,\ \cdots)$ values depending on whether the number of electrons in the molecule is even or odd.

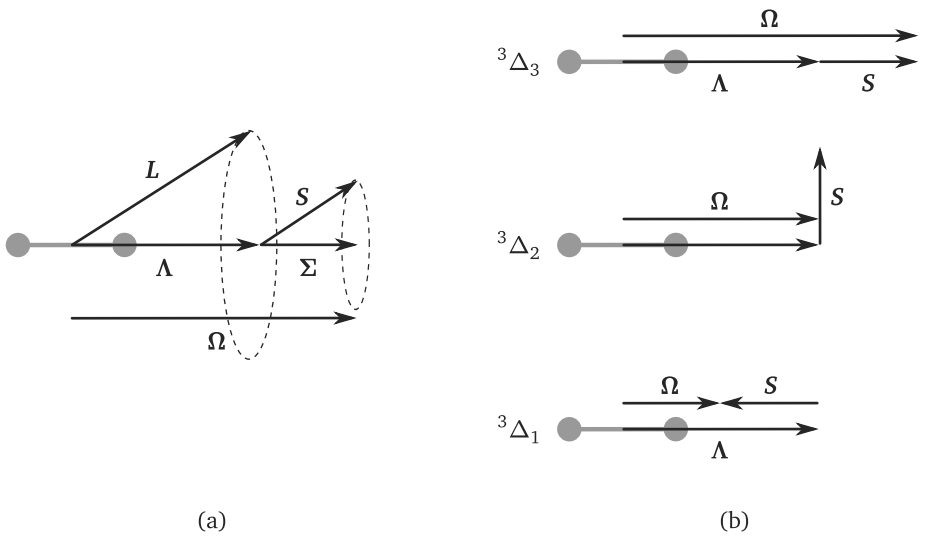

Figure 2.2. Electronic angular momenta and their coupling with the internuclear axis. (a) The molecular electric field couples the orbital angular momentum $\boldsymbol{L}$ of the electrons with the internuclear axis, and the internal magnetic field produced by the orbital motion of the electrons couples the electronic spin $\boldsymbol{S}$ with the internuclear axis. (b) The spin–orbit interaction splits an electronic state into $2S+1$ electronic substates with different energies. Shown here is an electronic state with $\Lambda = 2$ and $S = 1$.

All electronic states with $\Lambda > 0$ have $2S+1$ electronic substates. The orbital motion of the electrons produces an internal magnetic field along the internuclear axis and causes the electronic spin $\boldsymbol{S}$ to precess about the axis (Figure 2.2a). The axial component of $\boldsymbol{S}$ is conventionally designated $\boldsymbol{\Sigma}$. The corresponding quantum number

$$\Sigma = S,\ S-1,\ S-2,\ \cdots,\ -S \tag{2.13}$$

takes $2S+1$ possible values. The different values of Σ are associated with different energies. Therefore, the spin–orbit interaction splits the energy level of an electronic state into a multiplet of $2S+1$ components (Figure 2.2b). The electronic term value of each multiplet component is approximately given by

$$T_e = T_e^{(1)} + A\Lambda\Sigma \tag{2.14}$$

where $T_e^{(1)}$ is the electronic term value when the spin–orbit interaction is neglected, and A is the spin–orbit coupling constant. The second term represents the magnetic energy of the electronic spin: the magnitude of the magnetic field is proportional to Λ, and the magnetic moment of the electronic spin in the field direction is proportional to Σ. The components of the multiplet are often referred to as electronic substates. They are, in addition to Σ, characterized by the

quantum number

$$\Omega = \Lambda + \Sigma \tag{2.15}$$

that corresponds to the projection $\boldsymbol{\Omega}$ of the total electronic angular momentum along the internuclear axis (Figure 2.2). The quantum numbers Σ and Ω take integral or half-integral values depending on whether the number of the electrons is even or odd.

All electronic states with $\Lambda = 0$ have no electronic substate as long as nuclear rotation is neglected. Since the electronic states have no orbital motion of the electrons, they have no internal magnetic field along the internuclear axis. In the absence of the magnetic field, the electronic spin $\boldsymbol{S}$ is not coupled to the internuclear axis at all, and therefore the quantum numbers Σ and Ω are not defined. In the absence of the spin–orbit interaction, no splitting of the energy level occurs; the electronic states are single without nuclear rotation.

The set of quantum numbers used to characterize the electronic states is summarized in what is known as the spectroscopic term symbol, which is written as

$$^{2S+1}\Lambda_{\Omega} \tag{2.16}$$

where the main symbol Λ is conventionally denoted with a Greek letter: Σ for $\Lambda = 0$*, Π for $\Lambda = 1$, Δ for $\Lambda = 2$, etc., analogous to the convention of designation for atoms. According to the value of $\Lambda = 0, 1, 2, \cdots$, an electronic state is called a Σ, Π, $\Delta \cdots$ state. Note that non-Σ states are doubly degenerate due to the Λ-type doubling, Σ states are not degenerate. The left superscript $2S + 1$ is the spin multiplicity, which is the number of degenerate spin states of a Σ state but is the number of electronic substates of a non-Σ state. The subscript Ω is used to specify the electronic substate of non-Σ states but is usually omitted from the term symbol unless each substate requires attention. The term symbols of the electronic states of N_2 and N_2^+ are shown along with the potential curves in Figure 2.1.

As a side note, the electronic states are also labeled with letters. The electronic state with the lowest energy in a molecule is called the ground state and is always labeled X. Excited states with the same spin multiplicity as that of the ground state are labeled with A, B, C, $\cdots$ in order of increasing energy, while those with the multiplicity different from that of the ground state are labeled likewise with a, b, c, $\cdots$. But this convention does not strictly apply to all excited states because of historical reasons (see Figure 2.1 for the designation of the excited

*This symbol Σ for electronic states must not be confused with the symbol Σ for the quantum number that corresponds to the projection of the electronic spin $\boldsymbol{S}$ along the internuclear axis.

states of N_2, which is very different from the convention).

In addition to the quantum numbers introduced above, the electronic states are classified according to the behavior of the electronic eigenfunction with respect to symmetry operations. The symmetry properties of the electronic eigenfunction arise from the symmetry properties of the internal electric field in which the electrons move. As will be shown later, the symmetry properties of the electronic states influence those of the rotational levels, and they together influence the selection rules for electronic transitions.

The electronic state of a diatomic molecule is classified by the behavior of the electronic wavefunction ψ_e with respect to a reflection at a plane containing the internuclear axis, which is a plane of symmetry. For such a reflection, ψ_e either remains unchanged or changes its sign. Accordingly, as the former or the latter is the case, an electronic state is labeled positive (+) or negative (−), respectively. This symmetry property is indicated by adding a superscript + or − to the term symbol. Σ states are designated Σ^+ and Σ^- states (Figure 2.1); however, non-Σ states are not designated likewise. This is because of the Λ-type doubling of non-Σ states. One component of the doubly degenerate states is always labeled + and the other is −. Designation such as $\Pi^\pm$, $\Delta^\pm$, $\Psi^\pm$, $\cdots$ is redundant and is usually omitted.

The electronic state of a homonuclear diatomic molecule is further classified by the behavior of the electronic eigenfunction ψ_e with respect to an inversion of the electronic coordinates at the center of the internuclear axis, which is a center of symmetry. For such an inversion, ψ_e either remains unchanged or changes its sign. Accordingly, as the former or the latter is the case, an electronic state is labeled "gerade" (g) or "ungerade" (u), respectively. This symmetry property is referred to as g/u parity and is indicated by adding a subscript g or u to the term symbol; it applies to both Σ and non-Σ states. Hence, the electronic states of homonuclear molecules are designated Σ_g^+, Σ_g^-, Σ_u^+, Σ_u^-, Π_g, Π_u, $\cdots$ states (Figure 2.1).

2.1.4 Coupling of Nuclear Rotation and Electronic Motion

The electronic and rotational motions influence each other in a way that the angular momenta of these motions form a resultant, the total angular momentum of the molecule. The coupling of the different angular momenta determines the structure of rotational levels: the quantum numbers and the symmetry properties of the rotational levels.

The electronic orbital angular momentum, the electronic spin, and the angular momentum of nuclear rotation are coupled to form the total angular momentum. The coupling of the

different angular momenta varies with different types of electronic states and some other factors. The different modes of coupling are classified into what is known as Hund's coupling cases. Although Hund's cases represent idealized, limiting cases, they provide insights into the rotational structures of actual molecules. There are five cases, conventionally labeled with letters (a) through (e). In the following, cases (a) and (b) are briefly introduced. They are the most widely observed in diatomic molecules [*Brown and Carrington*, 2003].

Hund's case (a) assumes that the electronic orbital angular momentum $\boldsymbol{L}$ is strongly coupled to the internuclear axis, and the electronic spin $\boldsymbol{S}$ is also strongly coupled to the internuclear axis due to the spin–orbit interaction. The strong coupling of the electronic motion to the internuclear axis essentially parallels the case for non-Σ states described in the previous section (Figure 2.2). Hence, in electronic states belonging to case (a), the electronic angular momentum $\boldsymbol{\Omega}$ is well defined, and the electronic energy level is split into a multiplet of $2S+1$ components.

In Hund's case (a), the angular momentum $\boldsymbol{\Omega}$ of the electronic motion and the angular momentum $\boldsymbol{R}$ of the rotation motion form a resultant, the total angular momentum $\boldsymbol{J}$ (Figure 2.3a). The corresponding quantum number J takes the values

$$J = |\Omega|,\ |\Omega|+1,\ |\Omega|+2,\ \cdots \tag{2.17}$$

for a given value of Ω; since Ω takes integral or half-integral values depending on whether the number of electrons is even or odd, J takes integral or half-integral values likewise. Using the quantum number J, the rotational term value excluding the centrifugal distortion term is expressed in a form of

$$F(J) = B_v J(J+1) \tag{2.18}$$

where the rotational constant B_v takes the same value for each multiplet component or electronic substate.

Hund's cases (b) assumes that while the electronic orbital angular momentum $\boldsymbol{L}$ is strongly coupled to the internuclear axis, the electronic spin $\boldsymbol{S}$ is very weakly coupled to the internuclear axis. The very weak coupling of $\boldsymbol{S}$ to the internuclear axis is observed in Σ states, in which $\boldsymbol{S}$ is not coupled to the internuclear axis at all due to the lack of the spin–orbit interaction; therefore, Σ states always belong to case (b). The very weak coupling of $\boldsymbol{S}$ to the internuclear axis is also observed in non-Σ states of some very light molecules [*Brown and Carrington*, 2003]. Nevertheless, in electronic states belonging to in case (b), the electronic angular momentum $\boldsymbol{\Omega}$ is not defined.

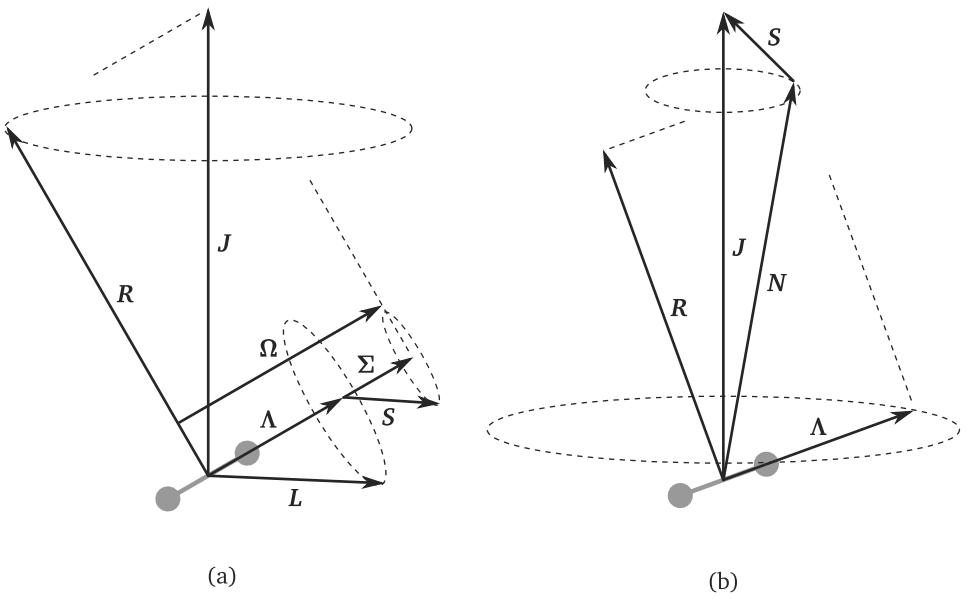

Figure 2.3. Hund's coupling case (a) and (b). They are most widely observed coupling cases. Hund's case (a) is characterized by the very strong coupling of the electronic motion (both orbital and spin) to the internuclear axis. Hund's case (b) is characterized by the very weak coupling of the electronic spin to the internuclear axis.

In Hund's case (b), the angular momentum $\boldsymbol{\Lambda}$ of the electronic motion and the angular momentum $\boldsymbol{R}$ of the rotational motion form a resultant, the total angular momentum $\boldsymbol{N}$ excluding electronic spin (Figure 2.3b). The corresponding quantum number N takes the integral values

$$N = \Lambda,\ \Lambda+1,\ \Lambda+1,\ \cdots \tag{2.19}$$

for a given value of Λ. Using the quantum number N, the rotational term value excluding the centrifugal distortion term is expressed in a form of

$$F(N) = B_v N(N+1). \tag{2.20}$$

Furthermore, each rotational level given by N is split into a multiplet of $2S+1$ components; the resulting sub-levels are characterized by the quantum number J that corresponds to the total angular momentum. The nuclear rotation produces a very slight magnetic field in the direction of $\boldsymbol{N}$ and causes a magnetic coupling between $\boldsymbol{N}$ and $\boldsymbol{S}$. This coupling causes $\boldsymbol{N}$ and $\boldsymbol{S}$ to form a resultant, the total angular momentum $\boldsymbol{J}$ (Figure 2.3b). The corresponding quantum

number J takes the values

$$J = (N+S),\ (N+S-1),\ (N+S-2),\ \cdots,\ |N-S| \tag{2.21}$$

for a given value of N; hence, it takes integral or half-integral values depending on whether the number of electrons is even or odd. The different values of J are associated with slightly different energies; therefore, the magnetic coupling splits the rotational level given by N into $2S+1$ components, which is equal to the spin multiplicity. The magnitude of splitting increases with nuclear rotation, linearly with the value of N.

Although Hund's coupling cases account for observed spectra to a good approximation, they merely represents idealized limiting cases; in reality, deviations from these idealized coupling cases are observed. The deviations come from that interactions regarded as small or neglected in the idealized coupling cases actually have an appreciable magnitude. The relative magnitude of these interactions changes with increasing rotation, and therefore the deviations becomes more obvious as the nuclear rotation increases.

One of the deviations is a transition from Hund's case (a) to (b) observed in non-Σ states. While Σ states strictly belong to case (b), non-Σ states usually belong to an intermediate between cases (a) and (b). The coupling of non-Σ states is well approximated as case (a) with no or very small rotation; that is, the electronic spin $\boldsymbol{S}$ is strongly coupled to the internuclear axis due to the spin–orbit interaction. However, as the nuclear rotation increases, the rotational speed becomes comparable to the precessional speed of $\boldsymbol{S}$ about the internuclear axis, and, as the rotation increases further, $\boldsymbol{S}$ becomes uncoupled from the internuclear axis. As a result of the spin uncoupling, $\boldsymbol{S}$ and $\boldsymbol{N}$ forms a resultant, the total angular momentum $\boldsymbol{J}$, in accordance with case (b). Therefore, non-Σ states belonging to an intermediate between cases (a) and (b) conform to case (a) at small values of J but tend to case (b) at large values of J.

Another type of the deviation is observed as splitting of the Λ-type doubling. In cases (a) and (b), the interaction between the nuclear rotation and the electronic orbital angular momentum $\boldsymbol{L}$ is neglected. However, this interaction must be accounted for at larger speeds of rotation; it produces a slight splitting of each rotational level given by J into two components. This is indeed splitting of the Λ-type doubling, the twofold degeneracy present in all non-Σ states (Section 2.1.3). The resulting two components, usually referred as Λ-type components, have different energies. The magnitude of splitting increases with nuclear rotation but is usually very small. The splitting typically amounts to only a fraction of a cm^{-1}, though it may reach a

few cm^{-1} in some cases at large values of J.

As electronic states are labeled with symmetry properties (Section 2.1.3), rotational levels are labeled likewise. While electronic states are classified by the symmetric properties of the electronic eigenfunction, rotational levels are classified by the behavior of the total wavefunction (Equation 2.2)—not the rotational wavefunction alone—with respect to symmetric operations. Hence, the symmetry properties of rotational levels are influenced by those of the electronic state.

The rotational levels of a diatomic molecule are classified by the behavior of the total wavefunction ψ for an inversion in a laboratory-fixed frame. For such inversion, ψ either remains unchanged or changes its sign. Accordingly, as the former or the latter is the case, a rotational level is labeled positive (+) or negative (−), respectively. This symmetry property of positive and negative—referred as parity—is not influenced by the behavior of the vibrational eigenfunction ψ_v because it only depends on the internuclear distance, but is influenced by the behavior of the rotational eigenfunction ψ_r and the electronic eigenfunction ψ_e.

For Σ states, the positive and negative are labeled depending on whether the quantum number N—not the quantum number J—is even or odd. The rotational eigenfunction ψ_r itself remains unchanged or changes its sign depending on whether N is even or odd. The electronic eigenfunction ψ_e remains unchanged or changes its sign depending on whether the electronic state is Σ^+ or Σ^-. This is because the inversion is equivalent to a rotation of the molecule through 180° about an axis perpendicular to the internuclear axis, followed by a reflection at a plane perpendicular to the rotational axis and passing through the internuclear axis. In the first operation, ψ_e remains unchanged. In the second operation, ψ_e remains unchanged for Σ^+ states and changes its sign for Σ^- states (Section 2.1.3). Therefore, the combination of the symmetry properties of ψ_r and ψ_e results in the rotational levels with even N being positive and those with odd N being negative for Σ^+ states, and vice versa for Σ^- states.

For non-Σ states, the positive and negative are assigned to the Λ-type components of each rotational level given by J. As mentioned in Section 2.1.3, one component of the doubly degenerate electronic states behaves like Σ^+ states, and the other behaves like Σ^- states. Therefore, for each rotational level given by J, one component is labeled positive, and the other is labeled negative.

The rotational levels of a homonuclear diatomic molecule are further classified by the behavior of the total wavefunction ψ for an exchange of the nuclei. For such an exchange, ψ either remains unchanged or changes its sign. Accordingly, as the former or the latter is the

case, a rotational level is labeled symmetric (s) or antisymmetric (a), respectively. Again, this symmetry property—referred as s/a parity—is not influenced by the behavior of the vibrational eigenfunction ψ_{v}, but is influenced by the behavior of the rotational eigenfunction ψ_{r} and the electronic eigenfunction ψ_{e}.

For both Σ and non-Σ states, the positive rotational levels are labeled symmetric and the negative rotational levels are labeled antisymmetric, or vice versa, depending on the g/u parity of the electronic state. An exchange of the nuclei is equivalent to an inversion of all particles at the center of the molecule, followed by an inversion of only the electrons at the center. In the first operation, the total wavefunction ψ remains unchanged for the positive rotational levels and changes its sign for the negative rotational levels. In the second operation, the electronic eigenfunction ψ_{e} remains unchanged for gerade electronic states and changes its sign for ungerade electronic states (Section 2.1.3). Therefore, the positive rotational levels are labeled symmetric and the negative rotational levels are labeled antisymmetric for gerade electronic states, and vice versa for ungerade electronic states.

2.1.5 Influence of Nuclear Statistics

The symmetric and antisymmetric rotational levels introduced in the previous section have different statistical weights[†]; one of these levels always has higher statistical weights than the other. The different statistical weights arise from the nuclear statistics of a homonuclear diatomic molecule.

An atomic nucleus has a nuclear spin $\boldsymbol{I}$, which is a resultant formed by the spins of the individual protons and neutrons. Since protons and neutrons have an intrinsic spin $1/2$, the nuclear spin quantum number I takes integral $(0, 1, 2, \cdots)$ or half-integral $(1/2, 3/2, 5/2, \cdots)$ values depending on the numbers of the constituent particles. Accordingly, a nucleus with even mass number has an integer spin, and a nucleus with odd mass number has a half-integer spin. Furthermore, all nuclei with even atomic number and even mass number have $I = 0$.

In a homonuclear diatomic molecule, the two atomic nuclei are indistinguishable, and therefore, for an exchange of the nuclei, the total wavefunction of the molecular system must be either symmetric or antisymmetric—that is, they must obey either the Bose–Einstein or Fermi–Dirac statistics. The nuclei with an integer spin obey the Bose–Einstein statistics; the total wavefunction must be symmetric for an exchange of the nuclei. The nuclei with a half-integer

[†]The statistical weight is the numbers of possible substates.

spin obey the Fermi–Dirac statistics; the total wavefunction must be antisymmetric for an exchange of the nuclei.

The total wavefunction ψ' under consideration takes into account the nuclear spin wavefunction ψ_{ns}, which have been neglected in the previous sections. Under the Born–Oppenheimer approximation, ψ' can be expressed as

$$\begin{aligned}\psi' &= \psi_{\mathrm{e}}\psi_{\mathrm{v}}\psi_{\mathrm{r}}\psi_{\mathrm{ns}} \\ &= \psi\psi_{\mathrm{ns}}\end{aligned} \tag{2.22}$$

where ψ is the total wavefunction excluding nuclear spin (Equation 2.2). Hence, the symmetric and antisymmetric property of ψ' is influenced by the behavior of ψ and ψ_{ns} for an exchange of the nuclei.

The total wavefunction ψ excluding nuclear spin is either symmetric or antisymmetric for an exchange of the nuclei. As mentioned in Section 2.1.4, for an given electronic state, the symmetric or antisymmetric property depends on whether a rotational level is symmetric or antisymmetric.

The nuclear spin wavefunction ψ_{ns} is also either symmetric or antisymmetric for an exchange of the nuclei, but with different statistical weights. The spin wavefunction depends on the orientation of the spins. Since each nucleus with spin I has $2I+1$ possible orientations, the two spin system in the molecule has $(2I+1)^2$ possible spin states. By taking linear combinations of these possible states, one can always form $(I+1)(2I+1)$ symmetric and $I(2I+1)$ antisymmetric components. These components can be split by a magnetic field, but the splitting is extremely small and is not usually resolved. Hence, the symmetric and antisymmetric nuclear spin states have statistical weights of $(I+1)(2I+1)$ and $I(2I+1)$, respectively.

The symmetric and antisymmetric rotational levels are associated with the symmetric and antisymmetric nuclear spin states in such a way that the combination conforms to the nuclear statistics. For the nuclei with an integer spin, the total wavefunction must be symmetric for an exchange of the nuclei; therefore, the symmetric rotational levels are associated with the symmetric nuclear spin states, and the antisymmetric rotational levels are associated with the antisymmetric nuclear spin states. For the nuclei with a half-integer spin, the total wavefunction must be antisymmetric for an exchange of the nuclei; therefore, the symmetric rotational levels are associated with the antisymmetric nuclear spin states, and the antisymmetric rotational

levels are associated with the symmetric nuclear spin states.

As a result, the symmetric and antisymmetric rotational levels have different nuclear statistical weights. The nuclear statistical weights of the symmetric and antisymmetric rotational levels are $(I+1)(2I+1)$ and $I(2I+1)$, respectively, for the nuclei with an integer spin, and vice versa for the nuclei with a half-integer spin.

2.1.6 Electronic Transition

As described in Section 2.1.2, an electronic state supports its own set of vibrational and rotational levels. Accordingly, an electronic transition involves vibrational transitions, and each vibrational transition, in turn, involves rotational transitions. These rotational transitions produce single lines. The rotational lines associated with a vibrational transition produce a band, and the vibrational bands associated with an electronic transition form an electronic band system. Therefore, a spectrum of an electronic band system is determined by the positions and intensities of the individual rotational lines. The transitions associated with the rotational lines do not occur arbitrarily but are restricted by the selection rules, which are specified in terms of the quantum numbers and the symmetry properties introduced in the previous sections.

Figure 2.4 illustrates energy levels and transitions involved in a typical $^3\Pi \rightarrow {}^3\Sigma$ electronic transition. As discussed in the previous sections, non-Σ states have $2(2S+1)$ electronic substates due to the spin-splitting and Λ-type doubling, and Σ states have $2S+1$ electronic substates due to the spin-splitting under the influence of nuclear rotation. The number of electronic substates in both types is expressed as $(2-\delta_{0,\Lambda})(2S+1)$ where $\delta_{0,\Lambda}$ is the Kronecker delta notation, which equals 1 if $\Lambda = 0$ and 0 otherwise. Each of the $(2-\delta_{0,\Lambda})(2S+1)$ electronic substates has a series of vibrational levels, and each vibrational level, in turn, has many rotational levels.

Regardless of the type of electronic states, each rotational level can be split by a magnetic field into $2J+1$ Zeeman states, each specified by a magnetic quantum number M. These Zeeman substates are degenerate in the absence of a magnetic field. A transition between two Zeeman substates forms a line component, which is the most fundamental spectral element. The sum of all Zeeman line components between two rotational levels is defined as a rotational line [*Whiting and Nicholls*, 1974; *Whiting et al.*, 1980]. Based on this definition, a doublet due to the Λ-type splitting is composed of two rotational lines regardless of whether they are resolved or not.

All rotational lines produced by transitions between the same vibrational levels v' and v''

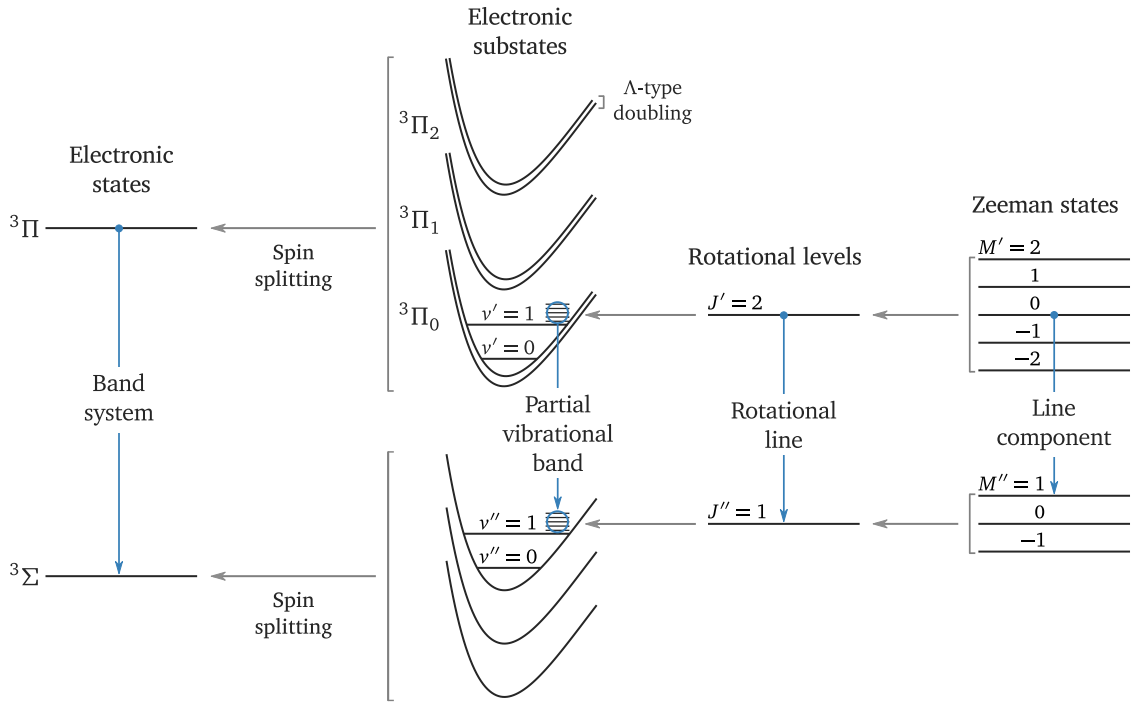

Figure 2.4. Energy levels and transitions of a typical $^3\Pi \rightarrow {}^3\Sigma$ electronic transition. The spin-splitting and Λ-type doubling are greatly exaggerated. This figure is based on the work published in [*Whiting and Nicholls*, 1974].

in all electronic substates compose a vibrational band. Figure 2.4 illustrates only the part of a vibrational band formed between two electronic substates. Furthermore, all vibrational bands produced by transitions between two electronic states compose an electronic band system. Therefore, an electronic band system is essentially a composite of all rotational lines involved in transitions between two electronic states.

The intensity of a single rotational line for spontaneous emission from a unit volume of a gas is given by

$$I_{J'J''} = A_{J'J'} N_{J'} \tag{2.23}$$

where $I_{J'J''}$ is the volume emission rate in units of photons $\mathrm{m}^{-3}\,\mathrm{s}^{-1}$, $N_{J'}$ is the population of the upper level in units of m^{-3}, and $A_{J'J''}$ is the transition probability or the Einstein coefficient for spontaneous emission in units of s^{-1}. The Einstein coefficient is expressed as

$$A_{J'J''} = \frac{64\pi^2}{(4\pi\epsilon_0)3hc^3}\nu^3_{J'J''}\frac{S_{J'J''}}{2J'+1} \tag{2.24}$$

where ϵ_0 is the permittivity of free space, c is the speed of light, and $\nu_{J'J'''}$ is the frequency of radiation, which corresponds to the energy difference between the two rotational levels. The

statistical weight factor $2J'+1$ is the degeneracy of the upper rotational level, i.e., the number of Zeeman substates. The quantity $S_{J'J''}$ is called the "line strength" for a rotational line in units of $\mathrm{C^2\,m^2}$.

The line strength $S_{J'J''}$ is defined by *Whiting and Nicholls* [1974] and *Whiting et al.* [1980] as

$$S_{J'J''} = \sum_{M'} \sum_{M''} \left| \left\langle \psi' \left| \boldsymbol{\mu} \right| \psi'' \right\rangle \right|^2 \tag{2.25}$$

where $\boldsymbol{\mu}$ is the electric dipole moment operator, ψ' and ψ'' are the wavefunctions of the upper and lower levels, respectively, and the double summation is over Zeeman substates of the upper and lower levels. Assuming isotropic excitation and unpolarized radiation, the line strength $S_{J'J''}$ can be written as

$$S_{J'J''} = \left| \left\langle v' \left| R_\mathrm{e}(r) \right| v'' \right\rangle \right|^2 \mathscr{S}_{J'J''} \tag{2.26}$$

where $|v'\rangle$ and $|v''\rangle$ are the vibrational wavefunctions of the upper and lower levels, respectively, $\mathscr{S}_{J'J''}$ is a dimensionless quantity called the rotational line intensity factor, and $R_\mathrm{e}(r)$ is the electronic transition moment in units of C m as a function of the internuclear distance r. For many band systems, $R_\mathrm{e}(r)$ is well approximated by either a constant or by a linear function of r, at least over the range of r important for the stronger vibrational bands [*Gilmore et al.*, 1992]. This indicates that the integral in Equation 2.26 is approximated as a product of the overlap integral of the vibrational wavefunctions and the electronic transition moment at a particular distance, called the r-centroid; this is known as the r-centroid approximation. Accordingly, $S_{J'J''}$ is expressed in a form of

$$S_{J'J''} = q_{v'v''} R_\mathrm{e}^2(\bar{r}_{v'v''}) \mathscr{S}_{J'J''} \tag{2.27}$$

where

$$q_{v'v''} = \left| \left\langle v' \left| v'' \right\rangle \right|^2 \tag{2.28}$$

is the square of the overlap integral of the vibrational wavefunctions, and

$$\bar{r}_{v'v''} = \left\langle v' \left| r \right| v'' \right\rangle / q_{v'v''}^{1/2} \tag{2.29}$$

is the r-centroid.

The square of the overlap integral $q_{v'v''}$ is known as the Franck–Condon factor. The Franck–Condon factors represent the probabilities of vibrational transitions associated with an electronic transition; they indicate the relative intensities of different vibrational bands in an electronic

band system. They also indicate the relative population of different vibrational levels in excited electronic states produced by electron impact. As they represent probabilities, the sum of the Frank–Condon factors are normalized to unity:

$$\sum_{v'} q_{v'v''} = \sum_{v''} q_{v'v''} = 1. \tag{2.30}$$

The rotational line intensity factor $\mathcal{S}_{J'J''}$ that has appeared in Equation 2.26 and 2.27 is also called Hönl–London factor. The Hönl–London factors are subject to the sum rule proposed by *Whiting and Nicholls* [1974] and *Whiting et al.* [1980]:

$$\sum_{J} \mathcal{S}_{J'J''} = (2 - \delta_{0,\Lambda'}\delta_{0,\Lambda''})(2S+1)(2J+1) \tag{2.31}$$

where $\delta_{0,\Lambda}$ is the Kronecker delta notation, which equals 1 if $\Lambda = 0$ and 0 otherwise, and the summation is over all allowed transitions from (or to) the group of rotational levels with the same value of J' or J''. The sum rule is symmetrical in J' and J'', and therefore explicit use of the primes on the right-hand side has been omitted.

An electronic transition involves the changes in the quantum numbers and symmetry properties introduced in the previous sections. These changes do not occur arbitrarily but are subject to constraints known as selection rules, which are derived from the matrix elements of Equation 2.25. The selection rules are classified as those common, regardless of the coupling cases, and those specific to certain coupling cases. In the following, the selection rules that are valid for Hund's cases (a) and (b) are summarized.

The selection rules for the electronic quantum numbers are as follows. The selection rule for the quantum number Λ that corresponds to the projection the electronic orbital momentum along the internuclear axis is

$$\Delta\Lambda = 0,\ \pm 1. \tag{2.32}$$

This means that, for example, Σ–Σ, Σ–Π, and Π–Π transitions are allowed, but Σ–Δ, Σ–Φ, and Π–Φ transitions are forbidden. The selection rule for the quantum number S that corresponds to the electronic spin is

$$\Delta S = 0. \tag{2.33}$$

This means that only transitions between electronic states with the same multipcility are allowed. In Hund's case (a), the quantum number Σ that corresponds to the projection of the electronic spin along the internuclear axis is defined. The selection rule for the quantum number is

$$\Delta \Sigma = 0. \tag{2.34}$$

This means that, for example, ${}^2\Pi_{1/2}$–${}^2\Pi_{1/2}$, ${}^2\Pi_{3/2}$–${}^2\Delta_{3/2}$, ${}^3\Pi_0$–${}^3\Pi_0$ transitions are allowed, but ${}^2\Pi_{1/2}$–${}^2\Delta_{3/2}$, ${}^3\Pi_0$–${}^3\Pi_1$ transitions are not allowed.

The selection rules for the symmetric properties of the electronic wavefunction are as follows. The selection rule for Σ^+ and Σ^- states is

$$\Sigma^+ \leftrightarrow \Sigma^+,\ \Sigma^- \leftrightarrow \Sigma^-,\ \Sigma^+ \nleftrightarrow \Sigma^-. \tag{2.35}$$

But Σ^+–Π and Σ^-–Π transitions do occur. For a homonuclear diatomic molecule, transitions are restricted to those between gerade and ungerade states, that is

$$g \leftrightarrow u,\ g \nleftrightarrow g,\ u \nleftrightarrow u. \tag{2.36}$$

This means that, for example, Σ_g^+–Σ_u^+, Σ_g^+–Π_u, Π_g–Π_u transitions are allowed, but Σ_g^+–Σ_g^+, Σ_g^+–Π_u, Π_g–Π_g transitions are not allowed.

The selection rules for the rotational quantum numbers are as follows. The selection rule for the quantum number J that corresponds to the total angular momentum is

$$\Delta J = 0,\ \pm 1 \text{ but } J = 0 \nrightarrow J = 0. \tag{2.37}$$

In Hund's case (a), an additional restriction applies to Equation 2.37; that is

$$\Delta J \neq 0 \text{ for } \Omega = 0 \rightarrow \Omega = 0. \tag{2.38}$$

In Hund's case (b), the quantum number N that corresponds to the total angular momentum excluding electronic spin is defined. The selection rule for the quantum number is

$$\Delta N = 0,\ \pm 1 \text{ but } \Delta N \neq 0 \text{ for } \Sigma\text{–}\Sigma \text{ transitions.} \tag{2.39}$$

The selection rules for the symmetric properties of the rotational levels are as follows. Transitions are restricted to those between the positive rotational levels and the negative rotational levels; that is

$$+ \leftrightarrow -,\ + \nleftrightarrow +,\ - \nleftrightarrow -. \tag{2.40}$$

For a homonuclear diatomic molecule, transitions are restricted to those between the symmetric rotational levels and those between the antisymmetric rotational levels; that is

$$s \leftrightarrow s,\ a \leftrightarrow a,\ s \nleftrightarrow a. \tag{2.41}$$

Since the symmetric and antisymmetric rotational levels have different nuclear statistical weights (Section 2.1.5), this selection rule produces intensity alternation of rotational lines. The ratio of line intensities is given by

$$R = \frac{I+1}{I} \tag{2.42}$$

where I is the nuclear spin quantum number of each nucleus. The stronger and weaker lines are those with $s \rightarrow s$ and $a \rightarrow a$ transitions, respectively, for the nuclei with an integer spin, and vice versa for the nuclei with a half-integer spin.

2.2 Synthetic Rotational Lines

To compute the individual rotational lines of the nitrogen band systems, I have developed a spectral model of diatomic molecules. It identifies the transitions that conform to an appropriate

set of the selection rules and computes the positions and intensities of the corresponding rotational lines. The resulting rotational lines establish a foundation for simulating the shapes of observed vibrational bands of the nitrogen band systems. In this section, I describe the computation of the rotational lines along with assumptions and approximations on which the model is built on.

First of all, the model does not distinguish the Λ-type doubling. As mentioned in Section 2.1.4, large rotational motion splits the twofold degeneracy of non-Σ states, but the splitting typically amounts to only a fraction of cm^{-1}, which is equivalent to about 0.01 nm at 400 nm and 0.05 nm at 900 nm. It is very small compared to the spectral resolution of our instruments, and can not be resolved in our measurements. Therefore, I do not distinguish the Λ-type doubling in the model. This means that a transition from a rotational level given by J produces a single line regardless whether the upper electronic state is a Σ state or a non-Σ state.

The model computes the position of a rotational line by taking the difference of the term values between the upper and lower levels; that is

$$\begin{aligned} \nu_{J'J''} &= T' - T'' \\ &= \left[T'_{\mathrm{e}} + G'(v') + F'(J')\right] - \left[T''_{\mathrm{e}} + G''(v'') + F''(J'')\right] \end{aligned} \tag{2.43}$$

where $\nu_{J'J''}$ is the line position in units of cm^{-1}. The line position given by Equation 2.43 has a dimension of wavenumbers in vacuum. To compare with our measurements, I convert the line positions into wavenumbers in air by multiplying the refractive index of dry air reported by *Ciddor* [1996]:

$$10^8(n_{\mathrm{air}} - 1) = \frac{k_1}{k_0 - \nu^2} + \frac{k_3}{k_2 - \nu^2} \tag{2.44}$$

where n_{air} is the refractive index of dry air, and ν is the wavenumber in $\mu\mathrm{m}^{-1}$. The constants k_0 through k_3 are 238.0185, 5 792 105, 57.362 and 167 917 $\mu\mathrm{m}^{-2}$, respectively.

The model computes the intensity of a rotational line from Equation 2.25, but under two assumptions, which make easier to compute relevant quantities. First, the model assumes that the Einstein coefficient $A_{J'J''}$ can be approximated in a form of

$$A_{J'J''} = A_{v'v''} \frac{\mathscr{S}_{J'J''}}{(2 - \delta_{\Lambda'0})(2J' + 1)} \tag{2.45}$$

where $(2-\delta_{\Lambda'0})(2J'+1)$ is the product of the statistical weights of the upper level due to the Λ-type doubling and the Zeeman states. The Einstein coefficient $A_{v'v''}$ for an electronic–vibrational transition is given by summing $A_{J'J''}$ for all possible rotational transitions from the upper level [*Schadee*, 1978]:

$$\begin{aligned} A_{v'v''} &= \sum_{J''} A_{J'J''} / g_n' g_v' \\ &= \frac{64\pi^2}{(4\pi\epsilon_0)3hc^3} \frac{\sum_{J''} \mathcal{S}_{J'J''}}{g_n' g_v' (2J'+1)} \nu_{v'v''}^3 \, q_{v'v''} R_e^2(\bar{r}_{v'v''}) \\ &= \frac{64\pi^2}{(4\pi\epsilon_0)3hc^3} \frac{2-\delta_{0,\Lambda'}\delta_{0,\Lambda''}}{2-\delta_{0,\Lambda'}} \nu_{v'v''}^3 \, q_{v'v''} R_e^2(\bar{r}_{v'v''}) \end{aligned} \tag{2.46}$$

where $g_n' = (2-\delta_{0,\Lambda'})(2S+1)$ and $g_v' = 1$ are the statistical weights of the upper electronic state and the upper vibrational level, respectively.

Second, the model assumes that the upper rotational levels are in thermal equilibrium at rotational temperature T_r, and therefore the density $N_{J'}$ of the upper rotational level is expressed as

$$N_{J'} = N_{v'} \frac{\phi(2J'+1)\exp(-F'(J')hc/k_B T_r)}{Q_r(T_r)} \tag{2.47}$$

where k_B is the Boltzmann constant, $N_{v'}$ is the density of the upper vibrational level v', and $Q_r(T_r)$ is the partition function of the upper rotational levels. An alteration factor ϕ arises from the different statistical weights of the symmetric and antisymmetric rotational levels (Section 2.1.5) and the corresponding selection rule (Equation 2.41). Its value is $(I+1)/(2I+1)$ for the symmetric rotational levels and $I/(2I+1)$ for the antisymmetric rotational levels for the nuclei with an integer spin, and vice versa for the nuclei with a half-integer spin. Since a nitrogen molecule has $I = 1$, $\phi = 2/3$ and $1/3$ for the symmetric and antisymmetric levels, respectively.

In the following sections, I describe the rotational structure of each nitrogen band system, which results from the multiplet structure of the electronic states and a set of the selection rules. I also show the computed rotational lines of a selected band for each band system.

2.2.1 N_2 First Positive System

The N_2 First Positive system is associated with the transition from the upper electronic state $B\,^3\Pi_g$ to the lower electronic state $A^3\Sigma_u^+$. The upper and lower states have electronic energies of 7.4 and 6.2 eV, respectively, above that of the ground state $X\,^1\Sigma_g^+$ of N_2 (Figure 2.1). The upper state conforms, to a good approximation, to Hund's case (a) at lower values of J but tends to Hund's case (b) at higher values of J [*Lofthus and Krupenie*, 1977]. This indicates that the upper state has $2S+1=3$ electronic substates at lower values of J, but it is no longer the case at higher values of J. Therefore, I treat the upper state as belonging to an intermediate between Hund's cases (a) and (b). On the other hand, the lower state strictly belongs to Hund's case (b); therefore, each rotational level given by N is composed of $2S+1=3$ sub-levels with $J=N+1$, $J=N$, and $J=N-1$.

Figure 2.5 illustrates the rotational structure of the First Positive system with the upper state conforming to Hund's case (a). The triplet manifolds of the $^3\Pi$ state form three sub-bands $^3\Pi_0 \rightarrow {}^3\Sigma$, $^3\Pi_1 \rightarrow {}^3\Sigma$, and $^3\Pi_2 \rightarrow {}^3\Sigma$. Within each sub-band, the rotational transitions are governed by the selection rule for the quantum number given by Equation 2.37 and by the selection rules for the symmetric properties given by Equation 2.40 and 2.41. These selection rules allow each of the three sub-bands to produce 9 series of rotational lines or branches: rotational lines are primarily classified by the values of ΔJ, and rotational lines with $\Delta J=-1$, 0 and 1 are designated P, Q and R branches, respectively. Out of the 9 branches, the three with $\Delta J=\Delta N$ are relatively strong and called main branches, and the six with $\Delta J\neq\Delta N$ are relatively weak and called satellite branches. Accordingly, there are 27 branches: 9 main (P_{11}, P_{22}, P_{33}, Q_{11}, Q_{22}, Q_{33}, R_{11}, R_{22} and R_{33}) and 18 satellite (P_{12}, P_{21}, P_{13}, P_{31}, P_{23}, P_{32}, Q_{12}, Q_{21}, Q_{13}, Q_{31}, Q_{23}, Q_{32}, R_{12}, R_{21}, R_{13}, R_{31}, R_{23} and R_{32}) branches.

The symmetric and antisymmetric rotational levels in the upper state are indistinguishable due to the Λ-type doubling, but those in the lower state are identifiable. The symmetric and antisymmetric levels in the lower states are the rotational levels with odd N'' and those with even N'', respectively (Figure 2.5). Hence, the alteration factor ϕ in Equation 2.47 equals to 1/3 for the upper levels that transition to the lower levels with even N'' and 2/3 for the upper levels that transition to the lower levels with odd N''. Because of the different statistical weights, the intensities of branches with odd N'' are twice as large as those with even N''.

To compute the positions and intensities of rotational lines, I adopted various constants and formulae from the literature; they are summarized in the following. The electronic term values

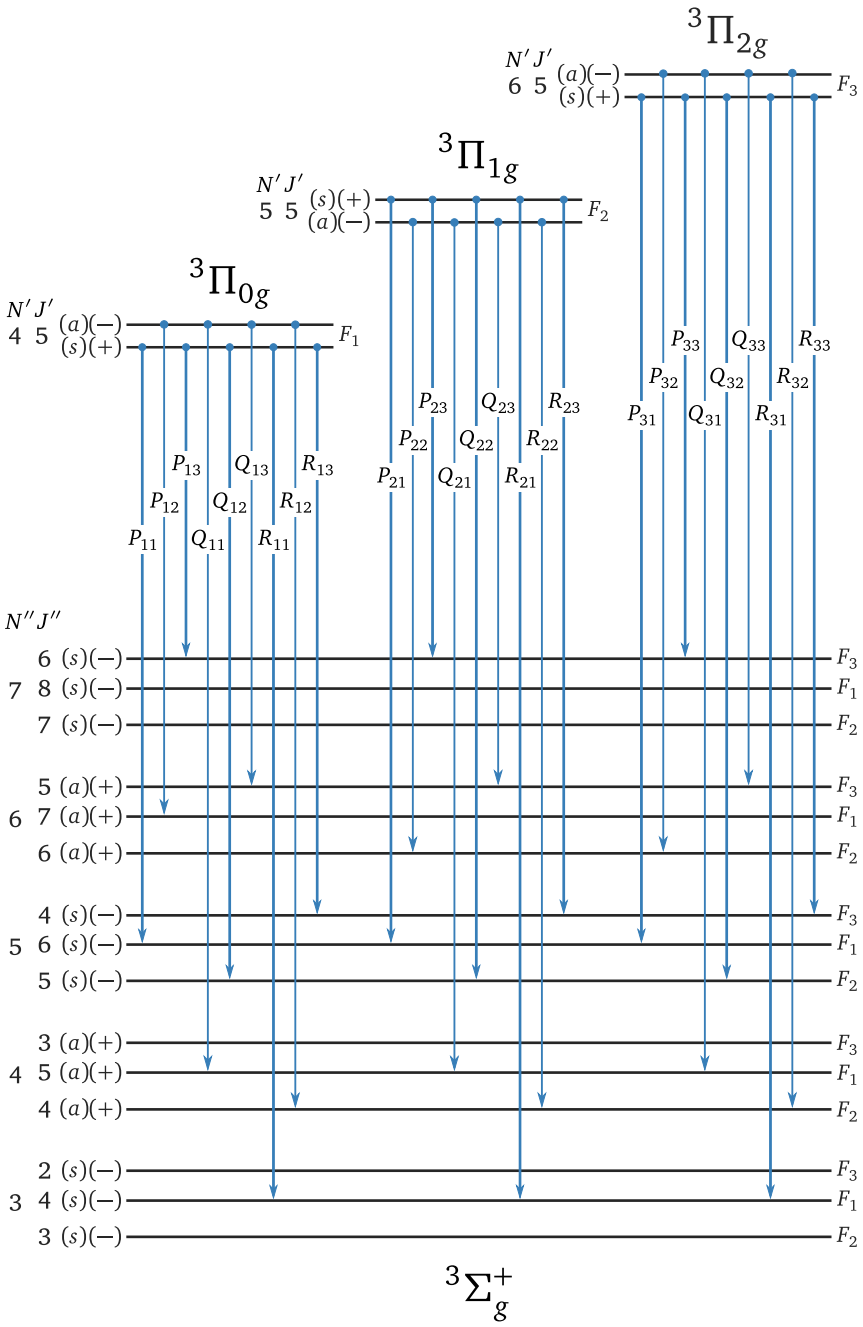

Figure 2.5. Rotational structure of the N_2 First Positive system with the upper state conforming to Hund's coupling case (a). Each of three sub-bands, $^3\Pi_0 \rightarrow {}^3\Sigma$, $^3\Pi_1 \rightarrow {}^3\Sigma$, and $^3\Pi_2 \rightarrow {}^3\Sigma$, produces 9 branches; therefore, there are 27 branches: 9 main and 18 satellite branches.

T_e of both states were adopted from those reported by *Laher and Gilmore* [1991]. The vibrational term values $G(v)$ of both states were computed from Equation 2.6 with the vibrational constants reported by *Laher and Gilmore* [1991]. The rotational term values $F(J)$ of the upper state were computed from Budó's formula for a $^3\Pi$ state [*Herzberg*, 1950, p. 235]:

$$
\begin{aligned}
F_1(J) &= B_v\left[J(J+1)-\sqrt{Z_1}-\frac{2Z_2}{3Z_1}\right]-D_v(J-\frac{1}{2})^4 \\
F_2(J) &= B_v\left[J(J+1)+\frac{4Z_2}{3Z_1}\right]-D_v(J+\frac{1}{2})^4 \\
F_3(J) &= B_v\left[J(J+1)+\sqrt{Z_1}-\frac{2Z_2}{3Z_1}\right]-D_v(J+\frac{3}{2})^4
\end{aligned}
\tag{2.48}
$$

This formula is valid for any degree of spin uncoupling: when the state conforms to Hund's case (a), F_1, F_2, and F_3 correspond to the components with $\Omega = 0$, $\Omega = 1$, and $\Omega = 2$, respectively; when the state conforms to Hund's case (b), F_1, F_2, and F_3 correspond to the components with $J = N+1$, $J = N$, and $J = N-1$, respectively. The quantities Z_1 and Z_2 in Equation 2.48 are given by

$$
\begin{aligned}
Z_1 &= Y(Y-4)+\frac{4}{3}+4J(J+1) \\
Z_2 &= Y(Y-1)-\frac{4}{9}-2J(J+1)
\end{aligned}
$$

where $Y = A_v/B_v$ is a measure of the strength of the coupling of the spin to the internuclear axis. The values of the spin–orbit coupling constants A_v were adopted from those reported by *Roux and Michaud* [1990]:

$$
A_v = 42.253 - 4.3\times10^{-2}(v+\frac{1}{2}) - 1.5\times10^{-3}(v+\frac{1}{2})^2 - 9.0\times10^{-5}(v+\frac{1}{2})^3. \tag{2.49}
$$

The rotational term values of the lower state were computed from Kramers's formula for a $^3\Sigma$ state [*Herzberg*, 1950, p. 223]:

$$
\begin{aligned}
F_1(N) &= B_vN(N+1)-\frac{2\lambda_v(N+1)}{2N+3}+\gamma_v(N+1)-D_vN^2(N+1)^2 \\
F_2(N) &= B_vN(N+1)-D_vN^2(N+1)^2 \\
F_3(N) &= B_vN(N+1)-\frac{2\lambda_vN}{2N-3}-\gamma_vN-D_vN^2(N+1)^2
\end{aligned}
\tag{2.50}
$$

where F_1, F_2, and F_3 refer to the components with $J = N+1$, $J = N$, and $J = N-1$, respectively, and λ_v and γ_v are the spin–splitting constants, respectively. The values of λ_v and γ_v were

adopted from those reported by *Roux and Michaud* [1990]:

$$\begin{aligned}\lambda_v &= -1.28 - 6.5 \times 10^{-2}(v + \frac{1}{2}) - 1.4 \times 10^{-3}(v + \frac{1}{2})^2 \\ \gamma_v &= -2.5 \times 10^{-3} + 1.1 \times 10^{-4}(v + \frac{1}{2})\end{aligned} \tag{2.51}$$

For both states, the values of the rotational constant B_v and the centrifugal distortion constant D_v were computed from Equation 2.10 and 2.11 with the spectroscopic constants reported by *Laher and Gilmore* [1991]. The values of the Einstein coefficients $A_{v'v''}$ were adopted from those reported by *Gilmore et al.* [1992], which conform to the definition in Equation 2.46. The Hönl–London factors $\mathcal{S}_{J'J''}$ were computed from the formulae for a triplet transition with $\Delta\Lambda = \pm 1$ given by *Kovacs* [1969, Table 3.10]. I have normalized the formulae so that they conform to the sum rule given by Equation 2.31 and have corrected typographical errors in the original publication, which were pointed out by *Whiting et al.* [1973].

Figure 2.10 illustrates the rotational lines of the (2–0) First Positive band computed at a rotational temperature of 300 K. Shown with the rotational lines is a Fortrat diagram, a graphical representation of the rotational branches showing the rotational quantum number J or N plotted against wavelength. The rotational branches in the Fortrat diagram form paraboras, and the vertices of some of these parabolas correpond to sharp peaks in the band. Among these peaks, the one at the edge of the band is called a band head. In the case of the First Positive band, the P_{11} branch forms the band head, and other branches such as the P_{22} and P_{33} form relatively sharp peaks inside the band.

2.2.2 N_2 Second Positive System

The N_2 Second Positive system is associated with the transition from the upper electronic state $C\,^3\Pi_u$ to the lower electronic state $B\,^3\Pi_g$, which is the upper state of the First Positive system. The upper and lower states have electronic energies of 11.0 and 7.4 eV, respectively, above that of the ground state $X\,^1\Sigma_g^+$ of N_2 (Figure 2.1). Both states conform, to a good approximation, to Hund's case (a) at lower values of J but tend to Hund's case (b) at higher values of J [*Lofthus and Krupenie*, 1977]. This indicates that both states have $2S + 1 = 3$ electronic substates at lower values of J, but that is no longer the case at higher values of J. Therefore, I treat both states as belonging to an intermediate between Hund's cases (a) and (b).

Figure 2.7 illustrates the rotational structure of the Second Positive system with both states

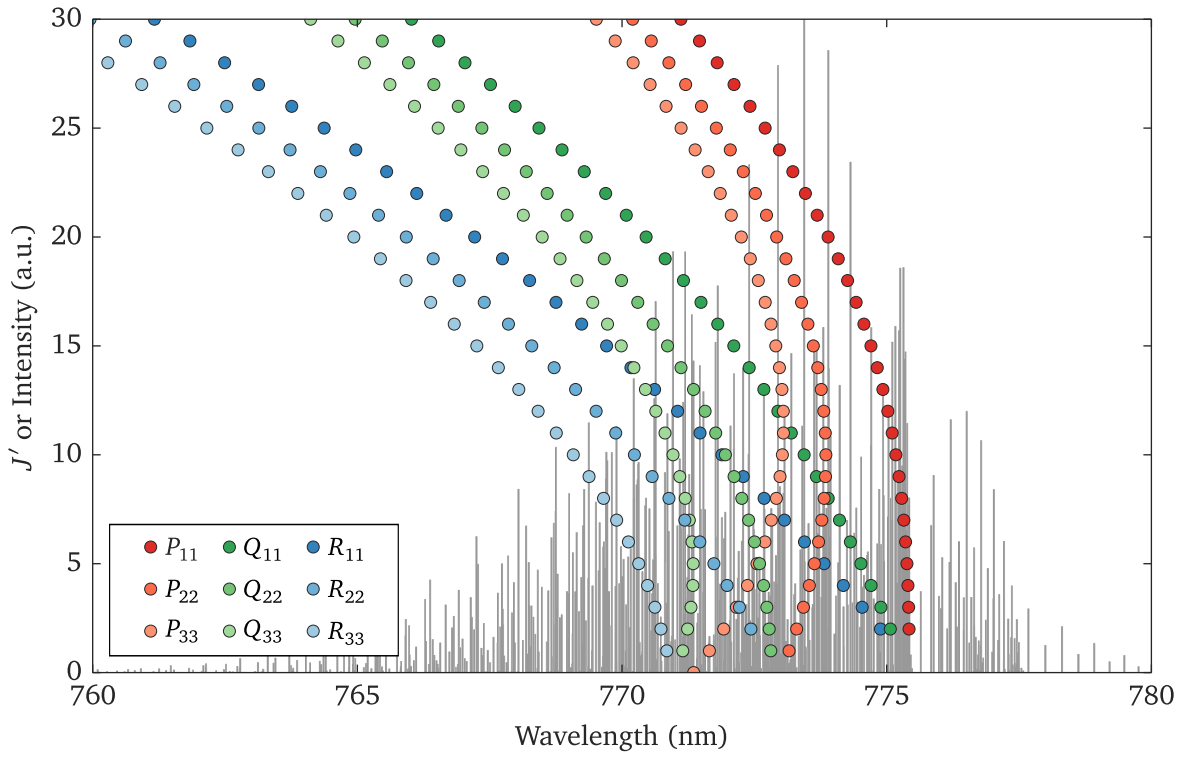

Figure 2.6. Rotational lines of the (2–0) N_2 First Positive band computed at a rotational temperature of 300 K. Shown with the rotational lines is the Fortrat diagram of the main branches.

conforming to Hund's case (a). The triplet manifolds of the $^3\Pi$ states form three sub-bands $^3\Pi_0 \rightarrow {}^3\Pi_0$, $^3\Pi_1 \rightarrow {}^3\Pi_1$, and $^3\Pi_2 \rightarrow {}^3\Pi_2$. Within each sub-band, the rotational transitions are governed by the selection rule for the quantum number given by Equation 2.37 and by the selection rules for the symmetric properties given by Equation 2.40 and 2.41. These selection rules allow each of the three sub-bands to produce three branches; therefore, there are 9 branches: all of them (P_{11}, P_{22}, P_{33}, Q_{11}, Q_{22}, Q_{33}, R_{11}, R_{22} and R_{33}) are main branches. When both states conform to Hund's case (b) at larger values of J, there are 19 branches: 9 main and 10 satellite branches. However, the difference between two coupling cases only modifies the number of satellite branches for which the intensities are negligible [*Naghizadeh-Kashani et al.*, 2010]. In both states, the symmetric and antisymmetric rotational levels are indistinguishable due to the Λ-type doubling (Figure 2.7). Hence, the alteration factor ϕ in Equation 2.47 equals to 1.

As in the case for the First Positive system, I adopt various constants and formulae from the literature to compute the positions and intensities of rotational lines; they are summarized in the following. The electronic term values T_e of both states were adopted from those reported

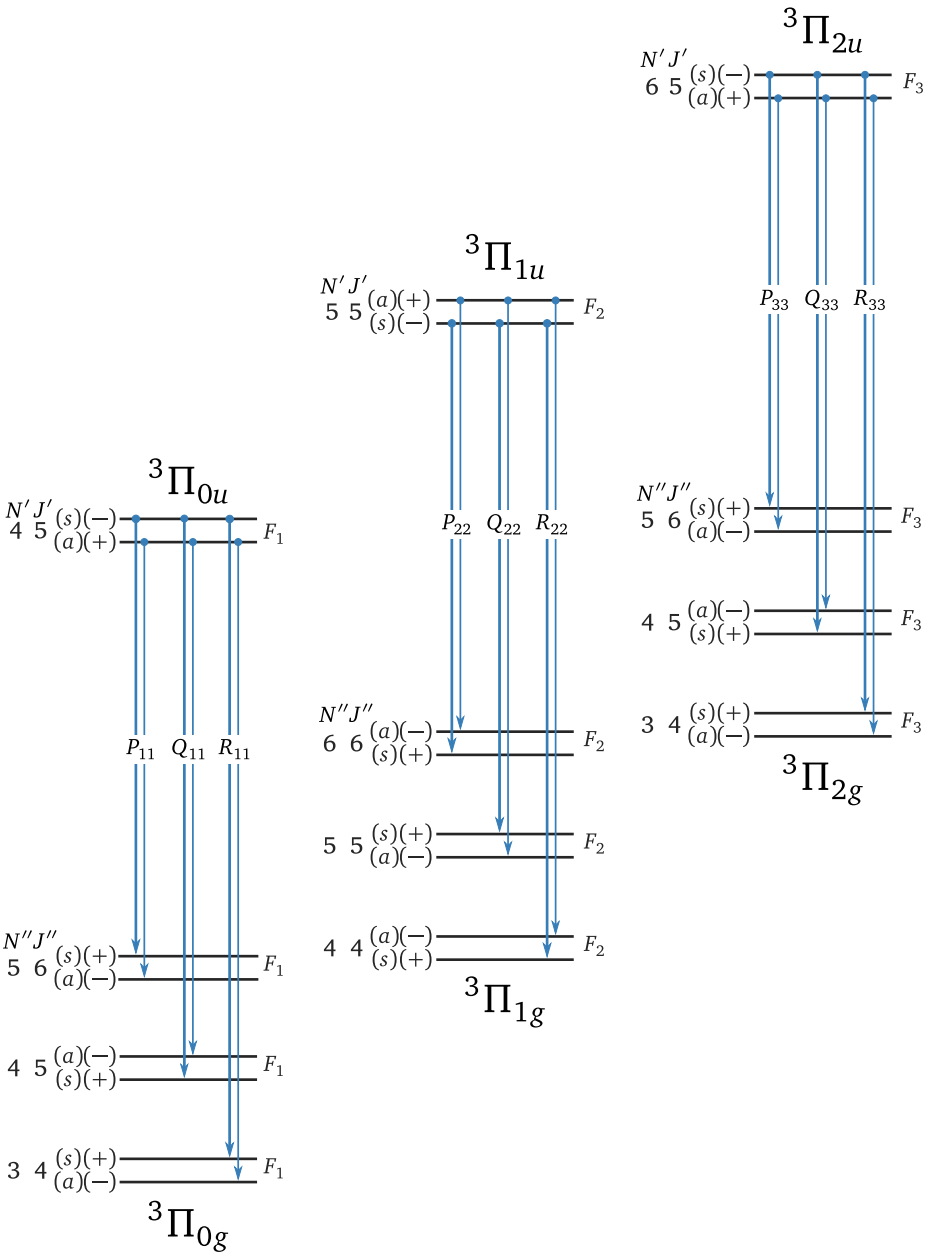

Figure 2.7. Rotational structure of the N_2 Second Positive system with both states conforming to Hund's case (a). Each of three sub-bands, $^3\Pi_0 \rightarrow {}^3\Pi_0$, $^3\Pi_1 \rightarrow {}^3\Pi_1$, and $^3\Pi_2 \rightarrow {}^3\Pi_2$, produces three branches; therefore, there are 9 branches.

by *Laher and Gilmore* [1991]. The vibrational term values $G(v)$ of both states were computed from Equation 2.6 with the vibrational constants reported by *Laher and Gilmore* [1991]. The rotational term values $F(J)$ of both states are computed from Equation 2.48. The values of the

spin–orbit coupling constant A_v of the upper state is given by *Roux et al.* [1993]:

$$A_v = 39.553 - 6.9 \times 10^{-1}(v + \frac{1}{2}) + 1.1 \times 10^{-1}(v + \frac{1}{2})^2 - 4.0 \times 10^{-2}(v + \frac{1}{2})^3. \qquad (2.52)$$

For both states, the values of the rotational constant B_v and the centrifugal distortion constant D_v were computed from Equation 2.10 and 2.11 with the values of the spectroscopic constants reported by *Laher and Gilmore* [1991]. The values of the Einstein coefficients $A_{v'v''}$ were adopted from those reported by *Gilmore et al.* [1992]. The Hönl–London factors $\mathcal{S}_{J'J''}$ were computed from the formulae for a triplet transition with $\Delta\Lambda = 0$ given by *Kovacs* [1969, Table 3.8]. I have normalized the formulae so that they conform to the sum rule given by Equation 2.31 and have corrected typographical errors in the original publication, which were pointed out by *Whiting et al.* [1973].

Figure 2.8 illustrates the rotational lines of the (0–0) Second Positive band computed at a rotational temperature of 300 K and the Fortrat diagram of the main branches. The P branches densely populate near 337.1 nm and produce a sharp, single band head there. The Q and R branches gradually degrade toward shorter wavelengths, though the Q branches are very weak.

2.2.3 N_2^+ First Negative System

The N_2^+ First Negative system is associated with the transition from the upper electronic state $B\,^2\Sigma_u^+$ to the lower electronic state $X\,^2\Sigma_g^+$, which is the ground state of N_2^+. The upper and lower states have electronic energies of 18.8 and 15.6 eV, respectively, above that of the ground state $X\,^1\Sigma_g^+$ of N_2 (Figure 2.1). Since both states are Σ states, they strictly belong to Hund's case (b); therefore, each rotational level given by N consists of $2S + 1 = 2$ sub-levels with $J = N + 1/2$ and $J = N - 1/2$.

Figure 2.9 illustrates the rotational structure of the First Negative system. The rotational transitions are governed by the selection rules for the quantum numbers given by Equation 2.37 and 2.39 and by the selection rules for the symmetry properties given by Equation 2.40 and 2.41. These selection rules produce 6 branches: four main (P_{11}, P_{22}, R_{11}, and R_{22}) and two satellite (Q_{12} and Q_{21}) branches. The symmetric and antisymmetric rotational levels in the upper state are the rotational levels with odd N' and those with even N', respectively (Figure 2.7). Hence, the alteration factor ϕ in Equation 2.47 equals to 2/3 for the upper levels with odd N' and 1/3 for those with even N'. Because of the different statistical weights, the intensities of the branches with odd N' (and even N'') are twice as large as those with even N' (and odd N'').

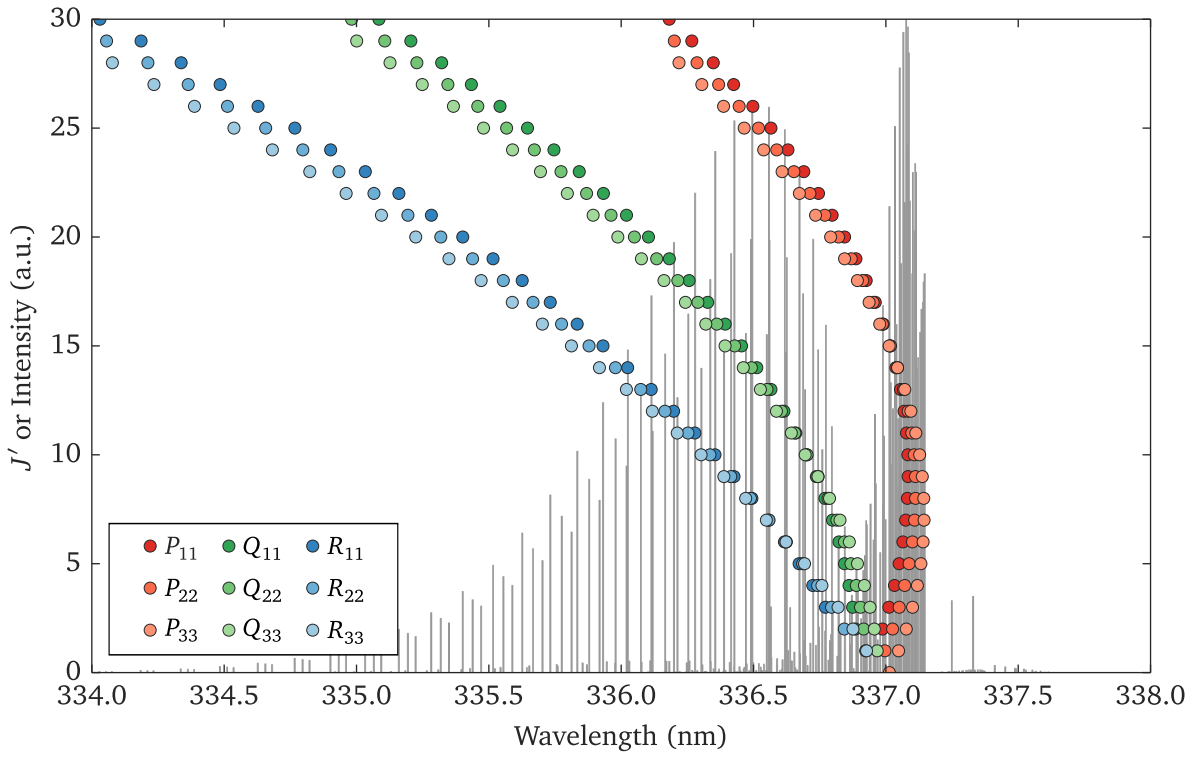

Figure 2.8. Rotational lines of the (0–0) N_2 Second Positive band computed at a rotational temperature of 300 K. Shown with the rotational lines is the Fortrat diagram of the main branches.

As in the case for the First Positive and Second Positive systems, I adopt various constants and formulae from the literature to compute the positions and intensities of rotational lines; they are summarized in the following. To compute the positions and intensities of rotational lines, I adopted various constants and formulae from the literature; they are summarized in the following. The electronic term values T_e of both states were adopted from those reported by *Laher and Gilmore* [1991]. The vibrational term values $G(v)$ of both states were computed from Equation 2.6 with the vibrational constants reported by *Laher and Gilmore* [1991]. The rotational term values $F(N)$ of both states were computed from Mulliken's formula for a $^2\Sigma$ state [*Herzberg*, 1950, p. 222]:

$$\begin{aligned} F_1(N) &= B_v N(N+1) + D_v\,[N(N+1)]^2 + \frac{1}{2}\gamma_v N \\ F_2(N) &= B_v N(N+1) + D_v\,[N(N+1)]^2 - \frac{1}{2}\gamma_v (N+1) \end{aligned} \tag{2.53}$$

where F_1 and F_2 terms correspond to the components with $J = N + 1/2$ and $J = N - 1/2$,

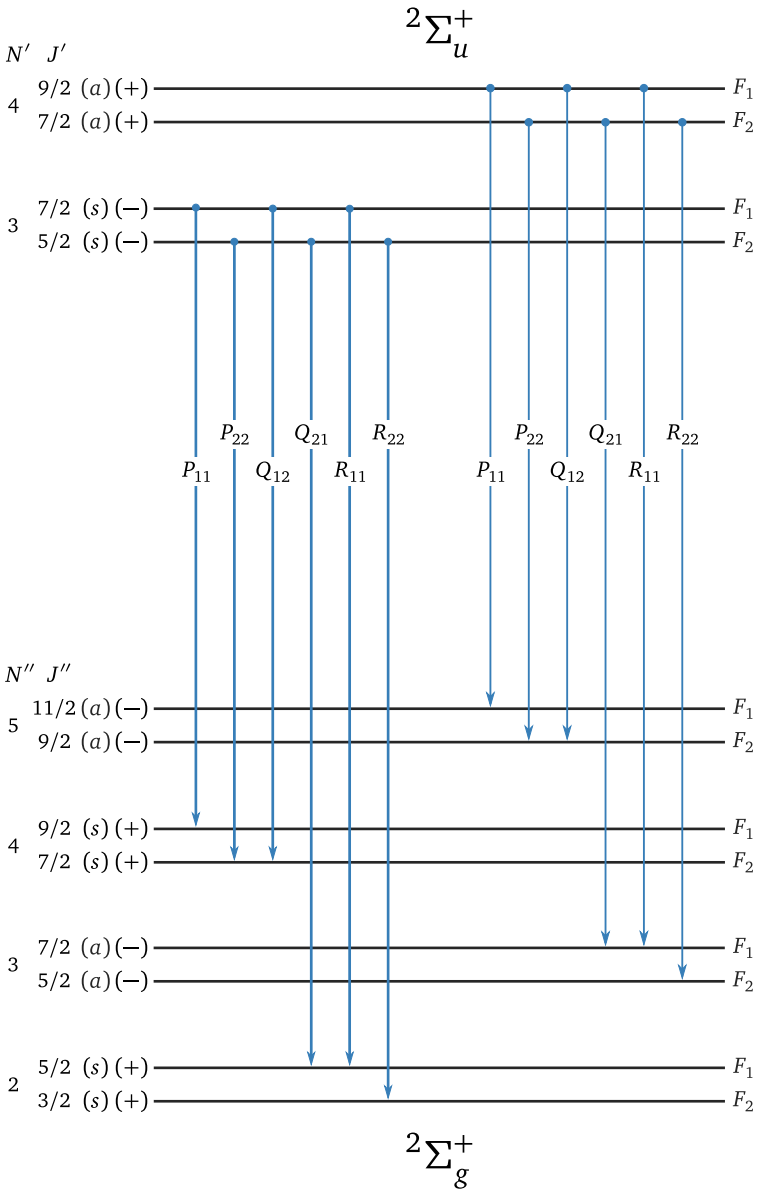

Figure 2.9. Rotational structure of the N_2^+ First Negative system. The rotational transitions produce 6 branches: four main and two satellite branches. The intensities of branches with odd N' (and odd N'') are twice as large as those with even N' (and odd N'').

respectively, and γ_v is the spin–splitting constant. The values of γ_v for both states were adopted from those reported by *Klynning and Pagès* [1982]. For both states, the values of the rotational constant B_v and the centrifugal distortion constant D_v were computed from Equation 2.10 and 2.11 with the spectroscopic constants reported by *Laher and Gilmore* [1991]. The values of the Einstein coefficients $A_{v'v''}$ were adopted from those reported by *Gilmore et al.* [1992]. The Hönl–London factors $\mathcal{S}_{J'J''}$ were computed from the formulae for a doublet transition with

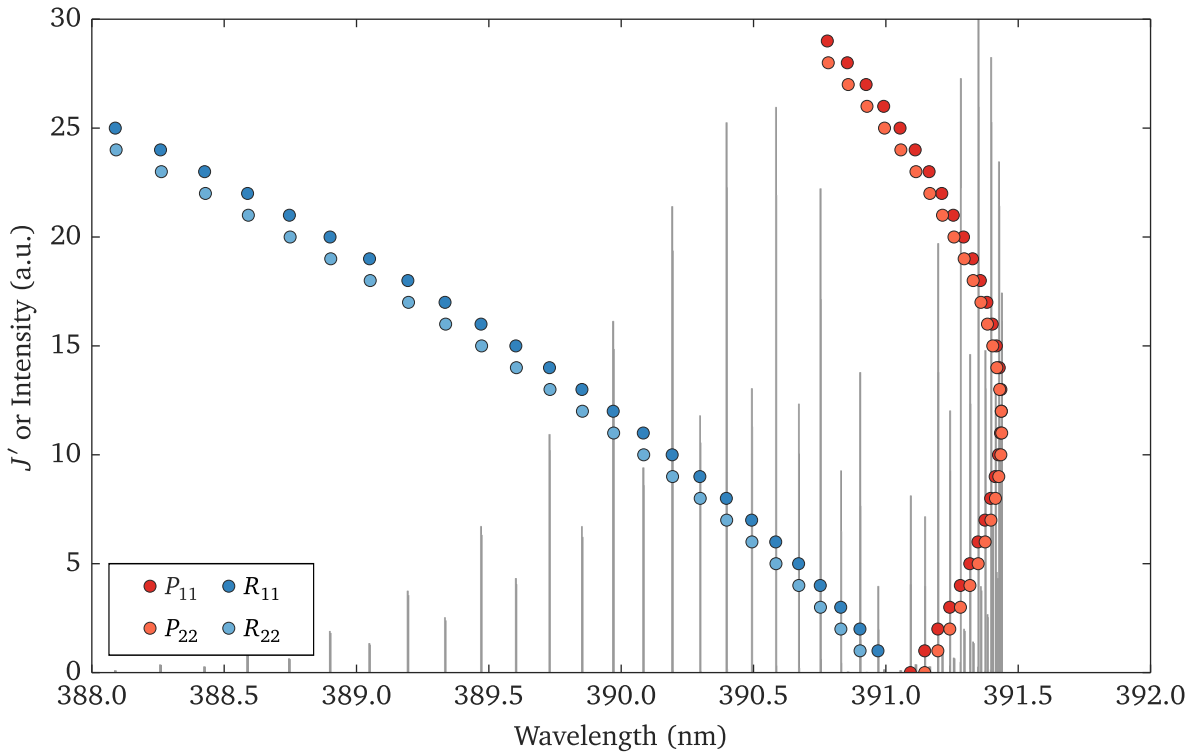

Figure 2.10. Rotational lines of the (0–0) N_2^+ First Negative band computed at a rotational temperature of 300 K. Shown with the rotational lines is the Fortrat diagram of the main branches.

$\Delta\Lambda = 0$ given by *Kovacs* [1969, Table 3.6].

Figure 2.10 illustrates the rotational lines of the (0–0) First Negative band computed at a rotational temperature of 300 K and the Fortrat diagram of the main branches. The P branches densely populate near 391.4 nm and produce a sharp, single band head there. The R branches gradually degrade toward shorter wavelengths. The 2 : 1 intensity alternation is clearly seen in the R branches.

2.3 Atmospheric Attenuation

To simulate the shapes of observed vibrational bands of the nitrogen band systems, I took into account the effects of the atmospheric attenuation. In this section, I discuss the effects of the atmospheric attenuation and describe a model for computing these effects. I also show attenuated synthetic spectra of the nitrogen band systems.

Optical emissions from sprites are severely attenuated by atmospheric scattering and absorption. Sprite observations are typically made at low elevation angles from a few to a few tens of degrees, giving long lines of sight—hundreds of kilometers—through the thick lower

atmosphere. Along the long lines of sight, sprite emissions are attenuated by processes such as molecular scattering (Rayleigh scattering), molecular absorption, and particle or aerosol scattering (Mie scattering). These processes are wavelength dependent, making observed spectra distorted from those originally radiated from sprites.

To incorporate the effects of the atmospheric attenuation in our spectral analysis, I computed the atmospheric transmittance using the Moderate Spectral Atmospheric Radiance and Transfer (MOSART) code [*Cornette et al.*, 1995, version 1.70]. The MOSART calculates the atmospheric transmittance and radiation along user-defined viewing geometries assuming local thermodynamic equilibrium between the UV and the microwave wavelengths. Extensive databases of atmospheric profiles and models are integrated in the code, and users can choose appropriate model parameters for their calculation. I have examined relevant parameters and adopted a set of the model parameters well-suited for our observations, which is summarized in Table 2.1.

Table 2.1. MOSART model parameters used in this study.

Parameter	Value
Model Atmosphere	1976 U.S. Standard Atmosphere (Summer)
Boundary Layer Aerosol Model	Default
Stratospheric Aerosol Model	Default
Tropo/Stratospheric Haze Profile	Default
Mesospheric Haze Profile	Default

Atmospheric transmittance profiles for typical ground- and aircraft-based observations are illustrated in Figure 2.11a. The data assume that an emission source at 60 km altitude, ground-based observation from 3.3 km altitude with a line of sight of 300 km, and aircraft observation from 13.7 km altitude with a line of sight of 200 km. As clearly shown in the figure, aircraft observations provide a significant advantage over ground-based observations by greatly reducing the atmospheric attenuation. It is especially notable at shorter wavelengths; for example, the transmittance at 400 nm is only few % for ground-based observations, but more than 70% for aircraft observations.

Figures 2.11b through 2.11f illustrate the contributions of different attenuating processes to the atmospheric transmittance profiles. With the well known cross section proportional to the inverse forth power of wavelength, Rayleigh scattering strongly attenuates the shorter wavelength. In addition, Mie scattering preferentially attenuates the shorter wavelength.

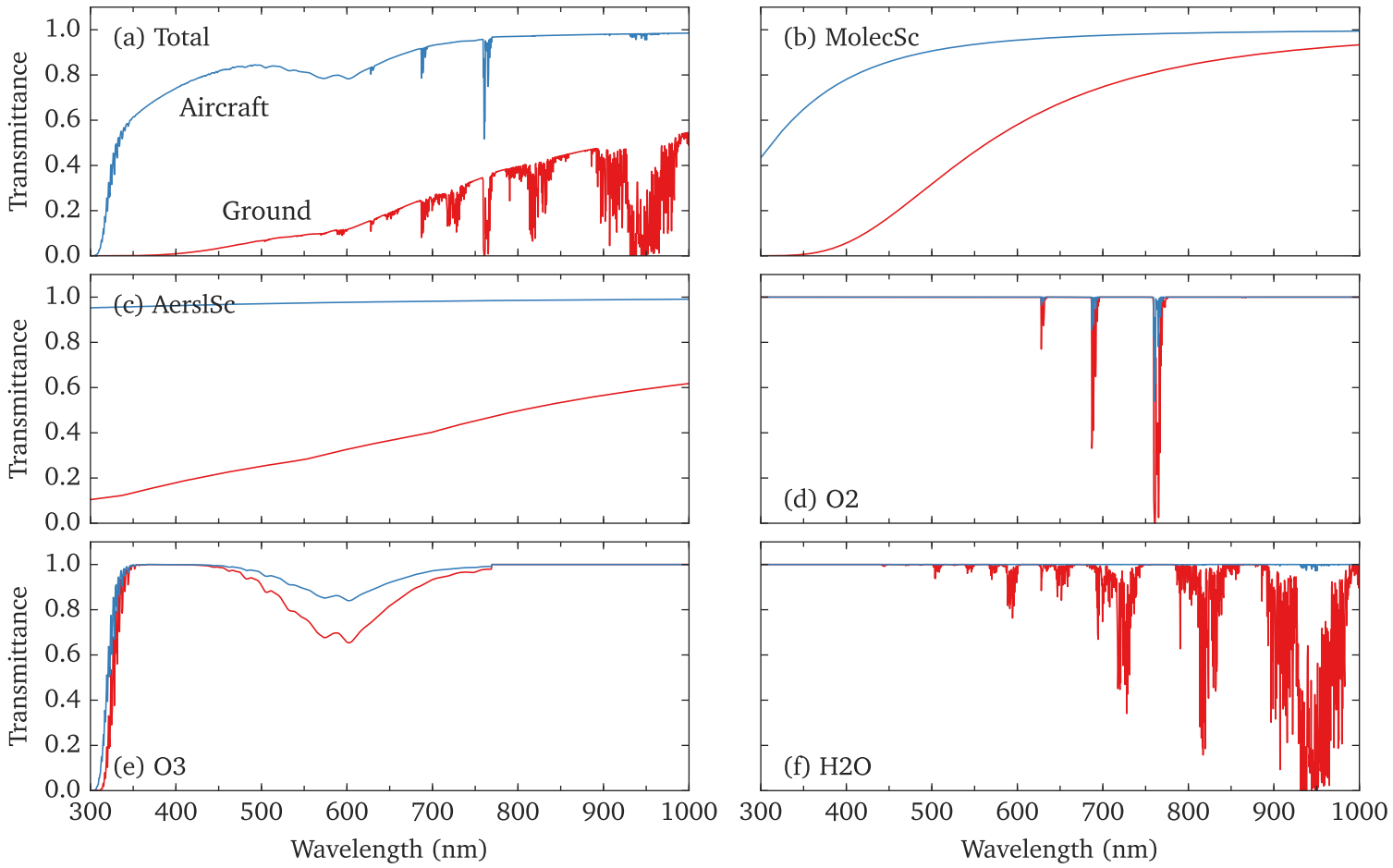

Figure 2.11. Atmospheric transmittance profiles for typical ground- and aircraft-based observations. (a) Total transmittance. ((b) through (f)) Transmittance by different attenuating processes: (b), Rayleigh scattering; (c), Mie scattering; (d), O_2 absorption; (e) O_3 absorption; (f) H_2O absorption. Red and blue curves show the data for ground- and aircraft-based observations, respectively.

Molecular oxygen has strongly peaked absorption bands corresponding to the O_2 Atmospheric ($b\,^1\Sigma_g^+ \rightarrow X\,^3\Sigma_g^-$) system. The (0–0) O_2 Atmospheric band at 762 nm overlaps the (3–1) N_2 First Positive band at 771 nm, and the absorption band can be clearly seen in observed sprite spectra [*Mende et al.*, 1995; *Hampton et al.*, 1996; *Morrill et al.*, 1998; *Bucsela et al.*, 2003]. Ozone has strong absorption below 300 nm by the Huggins band system, and broad absorption bands between 450 and 750 nm by the Chappius band system. Water vapor has significant absorption bands in the near infrared and beyond. These figures show that observations from an aircraft will significantly reduce the atmospheric attenuation from Rayleigh scattering, Mie scattering, and water vapor absorption.

Using atmospheric transmittance profiles obtained from the MOSART code, I simulate the effects of the atmospheric attenuation on synthetic spectra of nitrogen band systems. An attenuated band spectrum is synthesized in four steps. First, I compute the rotational lines of the vibrational bands (Section 2.2). Second, I compute an atmospheric transmittance profile for a given viewing geometry. Third, I collect the rotational lines into a 0.1 nm wavelength grid. This step is necessary because of the limitation on the spectral resolution of the MOSART output. Finally, I multiply the resulting spectrum by the atmospheric transmittance profile and produce the attenuated band spectrum.

Attenuated synthetic spectra of the First Positive, Second Positive, and First Negative systems are illustrated in Figure 2.12, 2.13, and 2.14, respectively. The spectra were produced by computing the rotational lines and by multiplying the atmospheric transmittance profiles shown in Figure 2.11. These figures clearly show that the atmospheric attenuation distorts the relative intensities of vibrational bands, which is especially severe at shorter wavelengths as seen in the Second Positive and First Negative systems.

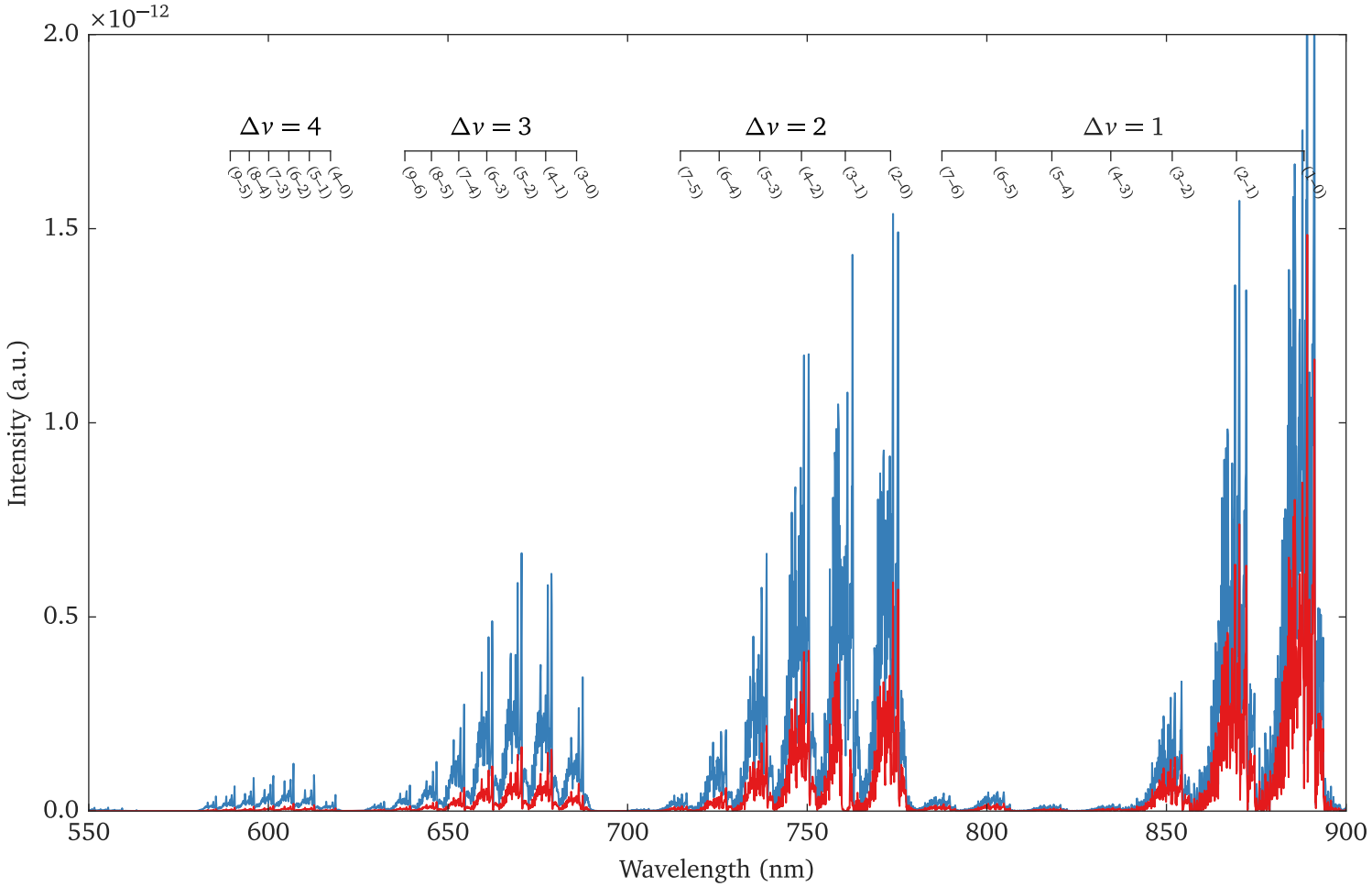

Figure 2.12. Attenuated synthetic spectra of the N_2 First Positive system. A synthetic spectrum of the First Positive system was attenuated with the atmospheric transmittance profiles shown in Figure 2.11. Red and blue curves show the data for ground- and aircraft-based observations, respectively.

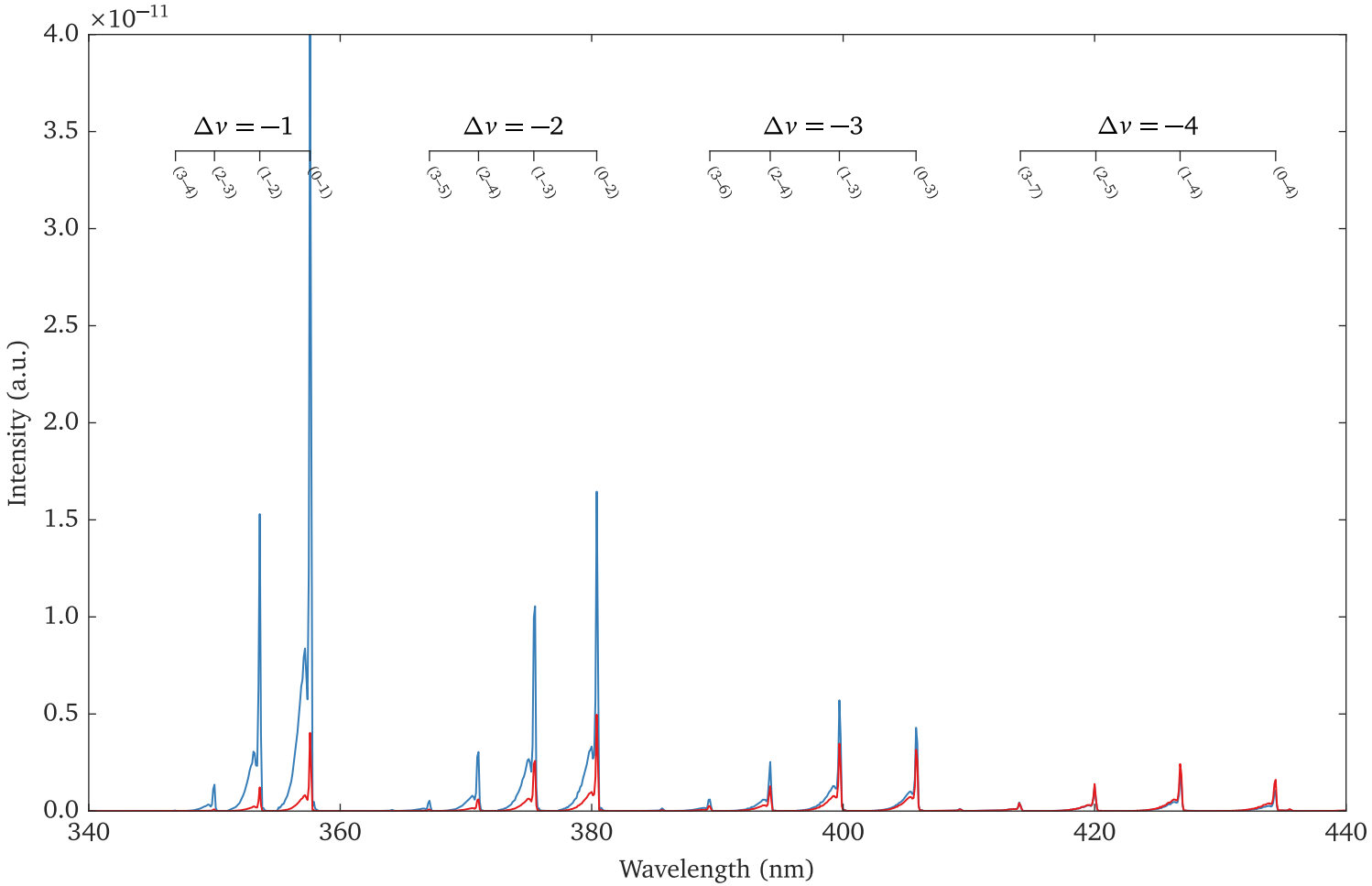

Figure 2.13. Attenuated synthetic spectra of the N_2 Second Positive system. A synthetic spectrum of the Second Positive system was attenuated with the atmospheric transmittance profiles shown in Figure 2.11. Red and blue curves show the data for ground- and aircraft-based observations, respectively. For presentation clarity, the intensities for ground-based observations were scaled by a factor of 50.

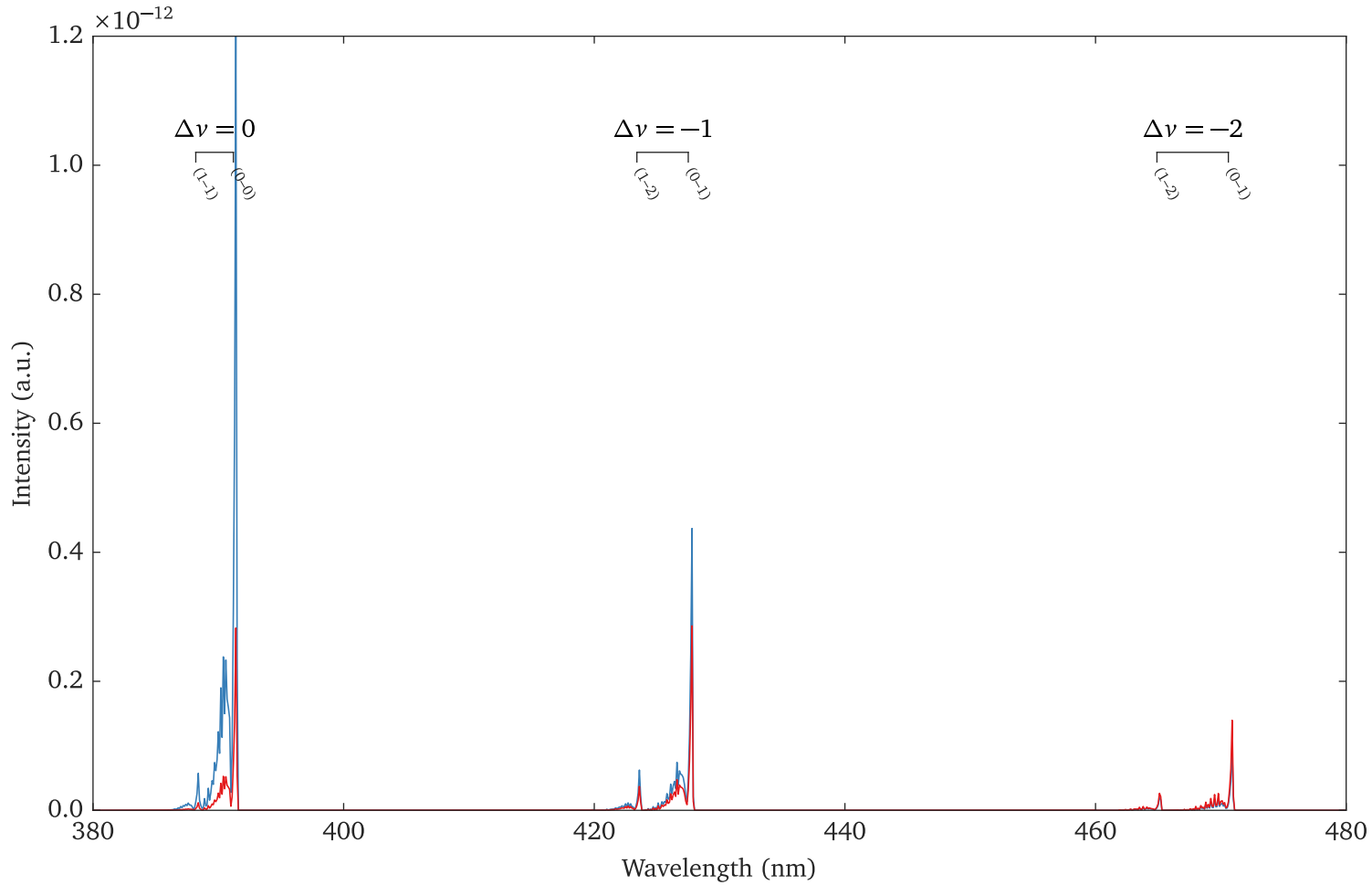

Figure 2.14. Attenuated synthetic spectra of the N_2^+ First Negative system. A synthetic spectrum of the First Negative system was attenuated with the atmospheric transmittance profiles shown in Figure 2.11. Red and blue curves show the data for the ground- and aircraft-based observations, respectively. For presentation clarity, the intensities for ground-based observation were scaled by a factor of 25.

Chapter 3
Observations of Vertically Resolved Sprite Spectra

3.1 Introduction

Ionization in sprites have been evidenced by the N_2^+ First Negative ($B\,^2\Sigma_u^+ \rightarrow X\,^2\Sigma_g^+$) emission, but further evidence of the ionization may be provided by the N_2^+ Meinel ($A^2\Pi_u^+ \rightarrow X\,^2\Sigma_g^+$) emission. Photometric and multi-color imaging observations have confirmed the presence of the First Negative emission in sprites [*Armstrong et al.*, 2000; *Morrill et al.*, 2002; *Kuo et al.*, 2005, 2008] and provided direct evidence of ionization. This indicates the presence of free electrons with energies higher than the excitation threshold energy of the First Negative system. The First Negative system has an excitation threshold energy of 18.8 eV, which is higher than 16.5 eV required for excitation of the Meinel system. Hence, the presence of the First Negative emission implies that the Meinel emission may be seen in sprites.

The Meinel emission would provide a valuable probe of ionization processes in sprites. The First Negative emission is in the ultraviolet and blue and is difficult to observe from the ground due to the atmospheric attenuation (Section 2.3). To avoid the attenuation, the ionization emissions have been observed from space in recent years [*Kuo et al.*, 2005, 2008; *Liu et al.*, 2006]. In contrast, the Meinel emission is in the visible and near infrared and is more accessible from the ground. For example, the atmospheric transmittance for the (2–0) Meinel band at 785.4 nm, according to the MOSART code, is about 20 times larger than that for the (0–0) First Negative band at 427.8 nm for a typical ground-based observations (Figure 2.11). Therefore, the Meinel emission would be a good target for examining ionization processes from ground-based platforms.

The presence of the Meinel emission, however, is somewhat controversial because it is expected to be strongly quenched in the mesosphere and below. The Meinel system has a relatively long radiative lifetime of about 12 μs and tends to be strongly quenched. Studies have indicated that the quenching altitude—the altitude below which the emission rate becomes less than half of the unquenched value—is 85 to 90 km (Table 1.1). This is at the nominal height of the top of sprites. Hence, the Meinel emission is expected to be difficult to observe in sprites.

The strong quenching does not necessarily indicate that the Meinel emission becomes completely extinct; it may be seen if the excitation is significant and surpasses the quenching effects. Such significant excitation may be caused by two mechanisms. The first is electron impact ionization, particularly in the tendrils, which has been observed to have a relative enhancement of ionization compared to the body [*Morrill et al.*, 2002]. The second is a

collisional energy transfer process beyond simple quenching. *Morrill et al.* [1998] and *Bucsela et al.* [2003] suggested that collisional energy transfer between $N_2^+(A^2\Pi_u^+)$ and $N_2^+(X^2\Sigma_g^+)$ [*Katayama et al.*, 1980; *Katayama*, 1984] is a rapid process and likely to play a role in exciting the Meinel emission in sprites.

Previous spectral measurements in the visible and near infrared have been examined for the presence of the Meinel emission, but the nature of the Meinel emission in sprites still remains an open issue. *Mende et al.* [1995] and *Hampton et al.* [1996] reported the first set of spectral data from sprites. They were obtained from the bodies of sprites. *Mende et al.* [1995] and *Hampton et al.* [1996] concluded that the observed spectra were primarily composed of the N_2 First Positive ($B^3\Pi_g \rightarrow A^3\Sigma_u^+$) system. These data were later examined by *Green et al.* [1996]. This study estimated the upper limits of the Meinel emission in the observed spectra but indicated they are at the noise level.

Morrill et al. [1998] and *Bucsela et al.* [2003] reported spectral data from the same sprite but from different altitudes, which are shown in Figure 3.1. They were obtained from the tendrils at 53 and 57 km altitude. *Morrill et al.* [1998] examined the 57 km spectrum and found spectral features attributable to the Meinel system; their finding was later re-examined and confirmed by *Bucsela et al.* [2003]. *Bucsela et al.* [2003], however, found no or little spectral feature of the Meinel system in the 53 km spectrum. Their findings raise two issues: (1) although the presence of the Meinel emission in the tendrils is consistent with the strong electron impact ionization expected there, the two spectra were obtained from below 60 km, well below the quenching altitude, where the Meinel emission should be difficult to observe; (2) although the absence of the Meinel emission at the lower altitude is consistent with the quenching effects, the altitude separation of the measurements, 4 km, is rather small.

Another issue relevant to sprite emissions in the visible and near infrared is the altitude variation of the vibrational distribution of the $N_2(B^3\Pi_g)$ state, the upper electronic state of the First Positive system ($B^3\Pi_g \rightarrow A^3\Sigma_u^+$). *Heavner* [2000] examined spectra obtained from different sprites and showed that the intensities of the First Positive bands change with altitude, indicating that the relative population of $N_2(B^3\Pi_g, v = 4)$ increases with altitude. *Bucsela et al.* [2003] examined the two spectra from the tendrils of the same sprite and reported that the First Positive system in the two spectra have different vibrational distributions, which are consistent with the altitude variation reported by *Heavner* [2000]. Furthermore, this study showed that the vibrational distribution from the lower altitude spectrum is similar to those observed in laboratory afterglow. *Bucsela et al.* [2003] suggested that collisional energy transfer processes

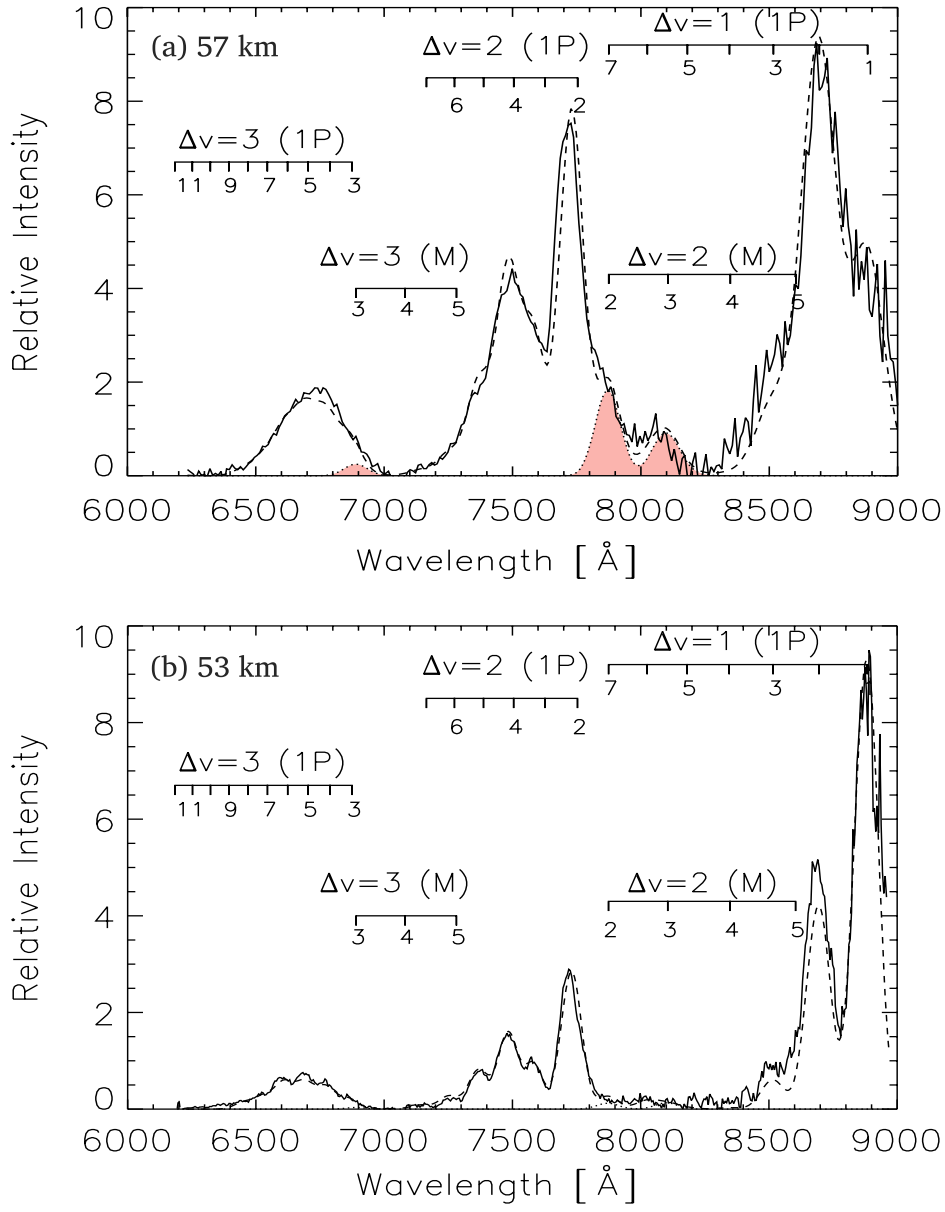

Figure 3.1. Spectra obtained from the same sprite but from two different altitudes. They were obtained from the tendrils at 53 and 57 km altitudes. *Morrill et al.* [1998] and *Bucsela et al.* [2003] concluded that, although they are primarily composed of the N_2 First Positive system, highlighted features in the 57 km spectrum are attributable to the N_2^+ Meinel system. These figures were reproduced from [*Bucsela et al.*, 2003].

beyond simple quenching are responsible for the observed distributions, and the similarity to the afterglow distribution implies that some emissions from the First Positive system are produced by energy transfer involving vibrationally excited N_2 ground state and the low-lying metastable state $N_2(A^3\Sigma_u^+)$.

Nevertheless, the data required to address these issues are limited, and additional spectral data are warranted. To systematically survey the presence of the Meinel emission and the $N_2(B^3\Pi_g)$ vibrational distribution along the vertical extent of sprites, we made a spectral observation campaign in July 2005 from the Laboratory Laboratory for Atmospheric Research (33.975°N, 107.181°W, 3255 m) in the Magdalena Mountains, near Socorro, New Mexico.

3.2 Instrumentation

An intensified CCD imaging spectrograph was used to measure emission spectra along the vertical extent of sprites. It was built based on an intensified CCD TV imaging spectrograph, which was first built for studying auroral emissions [*Hallinan et al.*, 1985] and later used for studying sprite emissions [*Hampton et al.*, 1996; *Morrill et al.*, 1998]. The essential optical system remains identical to that of the original spectrograph except for an imaging unit capable of recording images at a frame rate of up to 1000 fps, which had been used in previous sprite imaging observations [*Stenbaek-Nielsen et al.*, 2000; *Moudry et al.*, 2002, 2003]. The schematic of the spectrograph is illustrated in Figure 3.2.

The spectrograph has a large aperture front lens (Vivitar 135 mm f/1.2) which focuses entering light onto a vertically oriented slit in a flat mirror. The slit width is variable; for the data presented here, it was set to provide a field of view of 0.15° × 13°. The light passing through the slit strikes a concave mirror with a focal length of 305 mm, which is placed one focal length away from the slit; hence, the light reflecting from the concave mirror becomes collimated. The collimated light travels back and strikes the flat mirror, which is at an angle of 15° with respect to the optical axis of the front lens. The light reflecting from the flat mirror is then diffracted by a 600 lines/mm transmission grating.

Behind the grating is the imaging unit. An large aperture lens (Old Delft 105 mm f/0.9) focuses the first order spectrum from the grating onto an image intensifier (VARO), which has a 450 to 900 nm spectral range and a P43 phosphor with 1 ms decay time. The image from the intensifier is reduced via a set of relay lenses to fit the CCD chip of a high-speed camera (Hamilton Standard). The CCD chip has 256 × 256 pixels with a dynamic range of 8 bits (256 gray levels). It comprised four quadrants of 128 × 128 pixels; each quadrant is read

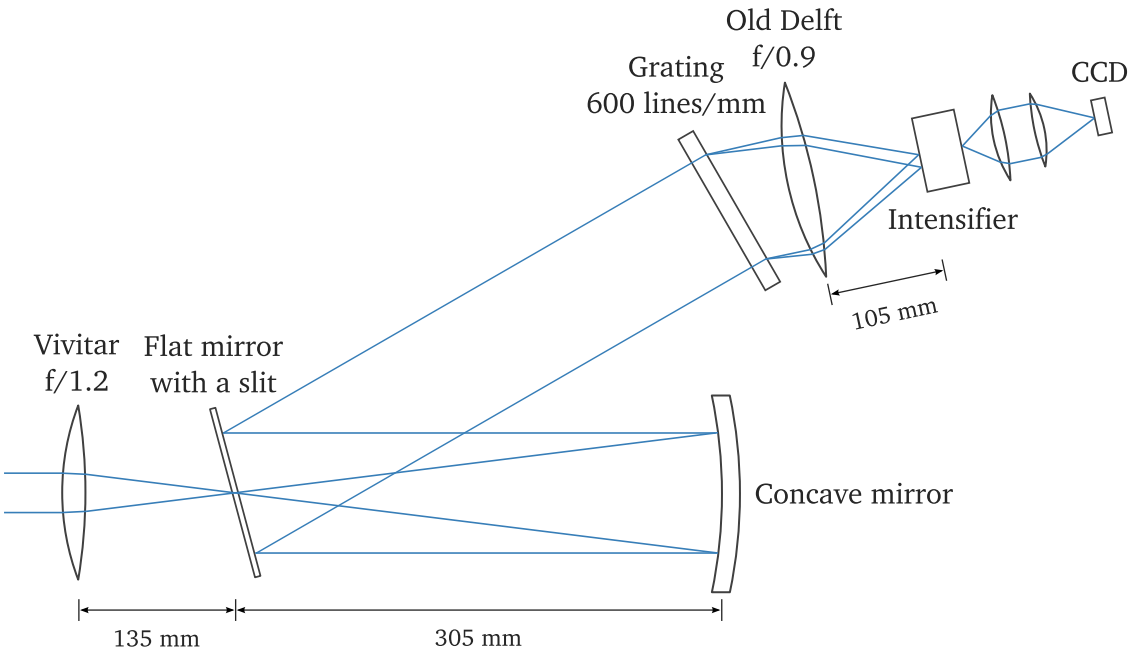

Figure 3.2. Schematic of the intensified CCD imaging spectrograph.

out in parallel with separate electronics, resulting in slightly different noise characteristics. The spectral coverage in an image is about 170 nm and can be set anywhere within the 350 to 900 nm range of the spectrograph. For the data presented here, the 170 nm range would give from 640 to 820 nm, covering the part of the $\Delta v = 1$ sequence and $\Delta v = 2$ and 3 sequences of the First Positive system, and the $\Delta v = 2$ and 3 sequences of the Meinel system.

The data acquisition of the spectrograph is controlled from a PC. The Hamilton Standard camera can record images at a frame rate of up to 1000 fps; for the data presented here, images were recorded at 300 fps. The camera continuously records images into an internal, circular memory buffer with a capacity equivalent to 4096 frames; unless they are stored to disk, the buffer will be overwritten and the data will be lost. The data were transferred and stored on a hard disk drive using a computer program developed by H. Stenbaek-Nielsen. Saving the data was triggered by a keyboard command, activated when seeing sprites on the associated video system.

The spectrograph was calibrated from measurements made during and after the observation period. The wavelength scale was determined from measurements of nitrogen, krypton, and mercury gas discharge lamps at the Langmuir Laboratory during the observation period. The instrument response and broadening were determined from laboratory measurements at the Geophysical Institute after the observation period. The instrument response convolved with

vignetting of the optical system was determined from measurements of a quartz–halogen tungsten lamp (Optronic Laboratories M-804) traceable to a NIST standard. The instrument broadening was determined from measurements of an isolated helium line at 668 nm. The measured line profile itself represents the instrument broadening; it was best approximated by an antisymmetric Gaussian–Lorentzian, in a form of

$$S(\lambda) = (1-\alpha)\exp\left(-4\ln(2)\left(\frac{\lambda}{W_{\mathrm{R,L}}}\right)^2\right) + \alpha\frac{1}{1+4(\lambda/W_{\mathrm{R,L}})^2} \tag{3.1}$$

where λ is wavelength in nm, α is a mixing ratio, and W_{R} and W_{L} are the full width half maximum of the right and the left side relative to the center, respectively. The function parameters were determined from the measurements. The spectral resolution defined as the mean of W_{R} and W_{L} is about 3 nm.

Along with the spectrograph, an intensified CCD video camera was used to record sprites and the background stars. It consists of a front lens (Canon 50 mm f/0.95), an image intensifier (VARO), and a CCD camera (PULNiX TM-745E), and has a wide field of view of 25° × 18°. The PULNiX camera operates at a normal video frame rate of 30 fps (60 fields per seconds) and provides 16.7 ms resolution. The video was routed to a video time inserter where time from a GPS receiver is inserted to each frame in the Society of Motion Picture and Television Engineers (SMPTE) format. The time inserted video was then recorded by a VHS tape recorder and displayed on a TV monitor.

The video camera and spectrograph were co-aligned on an azimuth–elevation mount (Figure 3.3). The alignment between the two instruments were accurately established from star fields that were recorded with the video camera and with the spectrograph running at a slow frame rate. With the known alignment, the video on the TV monitor provided scene awareness and allowed accurately aiming the spectrograph.

The background stars recorded in the video provided the pointing directions of the instruments. During the observations, the pointing directions were obtained from the reading of the azimuth–elevation mount, which is accurate enough for aiming the instruments but not for detailed analyses. The pointing directions for detailed analyses were determined from the background stars with a computer program called STAR after the observation period (H. Stenbaek-Nielsen, private communication). The STAR computes a star field using the Smithsonian Astrophysical Star Catalog for a given location at a given time and displays them onto a star field recorded in a video frame. The computed star field can be translated, rotated,

Figure 3.3. Instrument setup at the Laboratory Laboratory: an intensified CCD imaging spectrograph and an intensified CCD video camera were mounted on an azimuth–elevation mount. Shown here is the setup with Jim Desroschers working on the PC for data acquisition on the roof of the Annex building at the Laboratory Laboratory.

and stretched until a good fit is obtained. This provides the transformation from any pixel in the video frame to accurate azimuth and elevation angles.

3.3 Observations and Data

The instruments were installed at the northwest corner of the roof of the Annex building at the Langmuir Laboratory. This setup provided a view from the north clockwise through the south–southwest over the High Plains, where sprites are normally associated with mesoscale convective systems (MCSs) [*Lyons et al.*, 2000]—a group of storms that evolves in such a way that it produces a long-lived storm system having dimensions much larger than individual storms [*Goodman and MacGorman*, 1986]. In this type of storm system, positive cloud-to-ground lightning strokes are mostly confined to a region with the highest cloud tops, which are often found above the trailing stratiform region [*Lyons et al.*, 2000]. Moreover, a small subregion of the trailing stratiform region produces particularly large positive cloud-to-ground lightning strokes that causes sprites.

The storm activity during the observation period was monitored with infrared imagery from the Geostationary Operational Environmental Satellites (GOES) and lightning data from the National Lightning Detection Network (NLDN). The GOES is a two-satellite constellation in a geosynchronous orbit above the equator, and the infrared imagery provides cloud coverage and cloud top temperature. The NLDN is an array of more than 100 sensors covering the continental United States and documents cloud-to-ground lightning strokes with detection efficiency of 80 to 90 percent with high accuracy both in time (about 1 μs) and space (about 500 m) [*Cummins et al.*, 1998].

These meteorological data were made available in near real-time via Internet and were used for locating and tracking potential sprite-producing thunderstorms. The GOES infrared imagery was used to monitor the development of large storms, particularly the region with the highest cloud tops, which corresponds to a region of the coldest surface temperature in the imagery. The NLDN lightning data were used to monitor where large positive cloud-to-ground lightning strokes frequently occur—that is, the region where sprites most likely occur.

With the near real-time storm tracking capability, we were able to observe sprites without much difficulty despite the narrow field of views of the instruments. The typical observation protocol we employed is as follows. The instruments are aimed in the direction where sprites most likely occur based on the GOES and NLDN data, and the video from the intensified CCD camera is then closely monitored until an event occurs. Once an event is sighted in the video

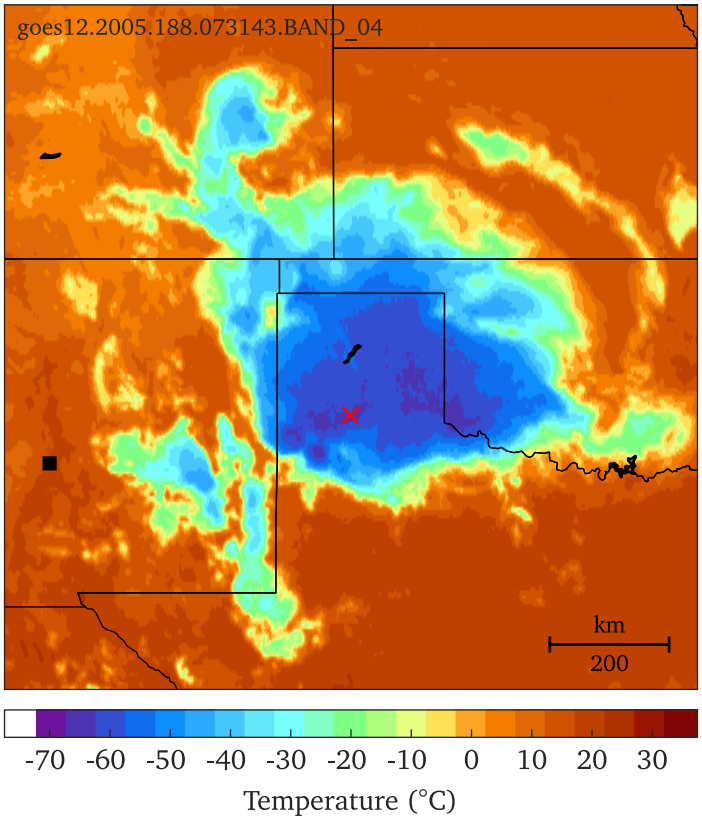

Figure 3.4. Observing geometry for the event at 07:20:54 UTC on 7 July 2005. The geometry is shown on top of the surface temperature produced from the GOES-12 infrared image. A square shows the location of the Langmuir Laboratory, and a cross shows the location of the parent positive cloud-to-ground lightning strike, as reported by the NLDN.

camera, the spectrograph is re-oriented to the position of that event. Sprites typically occur one after another in a small region of a storm for an extended period of time, and therefore another event is likely to occur in close enough proximity to be recorded by the spectrograph. The direction of the instruments are adjusted as a storm drifts or different regions become active throughout the night.

On 7 July 2005, sprites were observed over a large thunderstorm over northwest Texas, northeast to east of the Langmuir Laboratory (Figure 3.4). The viewing geometry provided relatively long horizontal distances of roughly 500 km, but good sprite spectra were obtained during the night. In the following, the best quality data obtained from two events on 7 July 2005 are presented: one occurred at 07:20:54 UTC and the other at 08:42:35 UTC.

The first event at 07:20:54 UTC was composed of multiple carrot sprites and columnar sprites as shown in Figure 3.5a. These sprites occurred following a positive cloud-to-ground lightning strike at (34.698°N, 101.710°W), as reported by the NLDN, which provides a horizontal range

of about 510 km from the Langmuir Laboratory. The location of the parent lightning stroke was used to infer the altitude scale of the sprites, assuming that the center of the sprites is at the range of the lightning stroke. Sprites, however, may be horizontally displaced from the parent lightning strokes by 50 km [*Wescott et al.*, 2001]. This gives an uncertainty of about 7 to 10 km in the altitude scale.

Altitude resolved spectra were obtained from the carrot sprite in the center of the cluster. The sprite has a bright, columnar body between 60 and 70 km altitude, upward branching structures spreading from the top of the body and terminating in diffusive emissions at 90 km altitude, and faint tendrils extending downward from the bottom of the body and terminating at 50 km altitude. Of these, the top portion of the body and the structures above were inside the field of view. The spectra recorded at 300 fps were identifiable in five frames: the second frame has good signals, the third has weaker signals, and the rest of the frames have spectra barely recognizable in the noise. The spectra in the second and third frame are shown in Figure 3.5b and c, respectively. Visually identifiable features in the spectra are the band structures of the First Positive system. The degradation in the structure near 760 nm, so characteristic in the data, is due to absorption by the (0–0) O_2 Atmospheric band.

The second event at 08:42:35 UTC was composed of a large carrot sprite and columnar sprites as shown in Figure 3.6a. These sprites occurred following a positive cloud-to-ground lightning strike at (33.946°N, 101.388°W), as reported by the NLDN, which provides a horizontal range of about 540 km from the Langmuir Laboratory. The location of the parent lightning stroke was used to infer the altitude scale of the sprites as in the case of the first event.

Altitude resolved spectra were obtained from the large carrot sprite in the center. The sprite has a bright body between 60 and 75 km altitude, diffusive tops spreading from the body, and faint tendrils extending from the bottom of the body and terminating at 50 km altitude. All the vertical structures were inside the field of view. The spectra recorded at 300 fps are identifiable in three frames: the first have quite good signals, the second has weaker signals, and the third has a spectrum barely recognizable in the noise. The spectra in the first and second frame are shown in Figure 3.6b and c, respectively. As is the case with the first event, visually identifiable features in the spectra are the band structures of the First Positive system. The horizontal dark band in the spectra, presumably, corresponds to a narrow section in the sprite structure at about 70 km altitude (Figure 3.6a), though it is difficult to confirm because the sprite saturated the image pixels in the video.

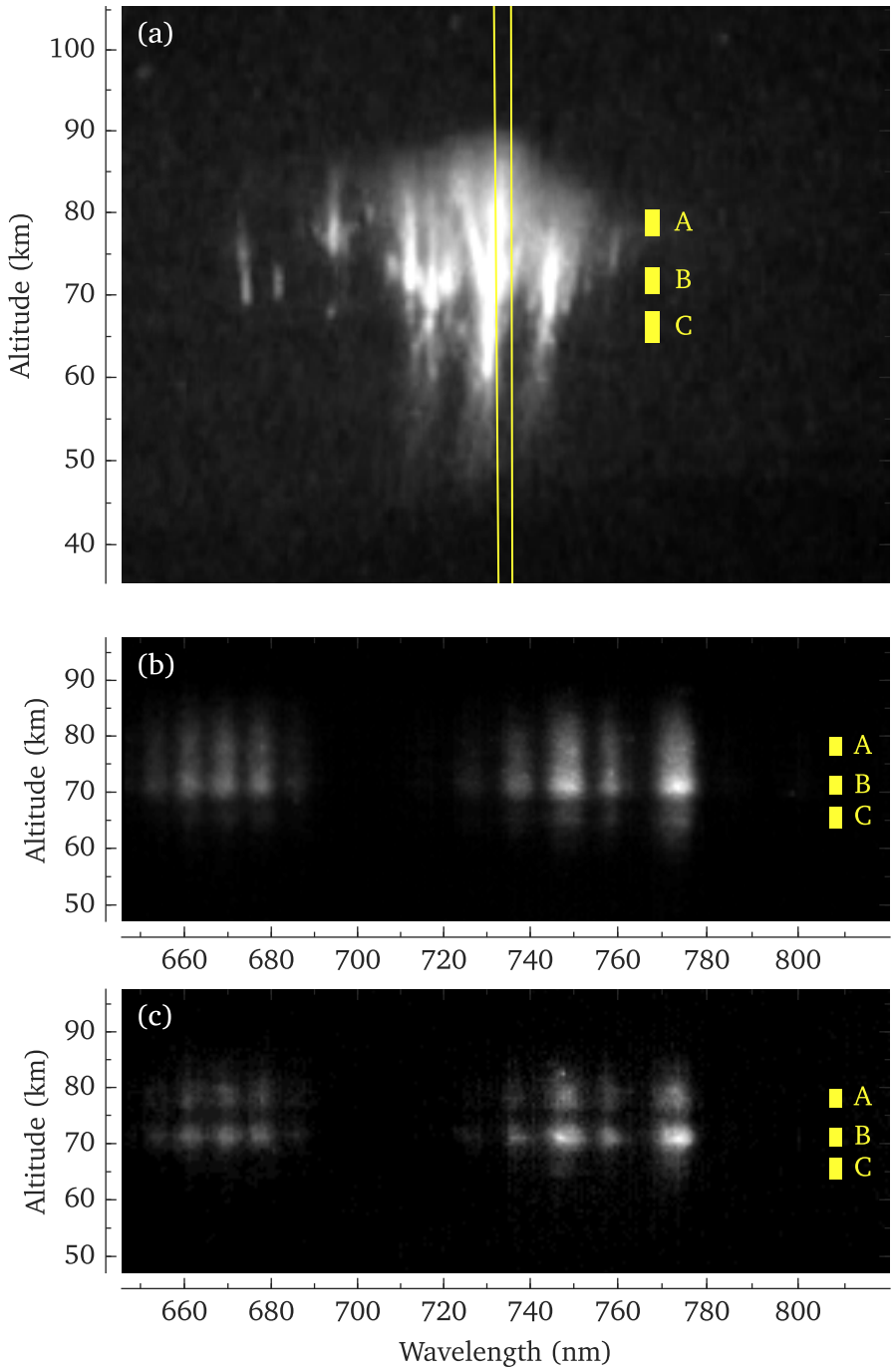

Figure 3.5. (a) Sprites at 07:20:54 UTC on 7 July 2005. Yellow lines in the center show the field of view of the spectrograph. Spectra were obtained from a carrot sprite in the center. (b) Spectrum in the second frame. (c) Spectrum in the third frame. Markers shows the altitude ranges where spectra are extracted for analysis.

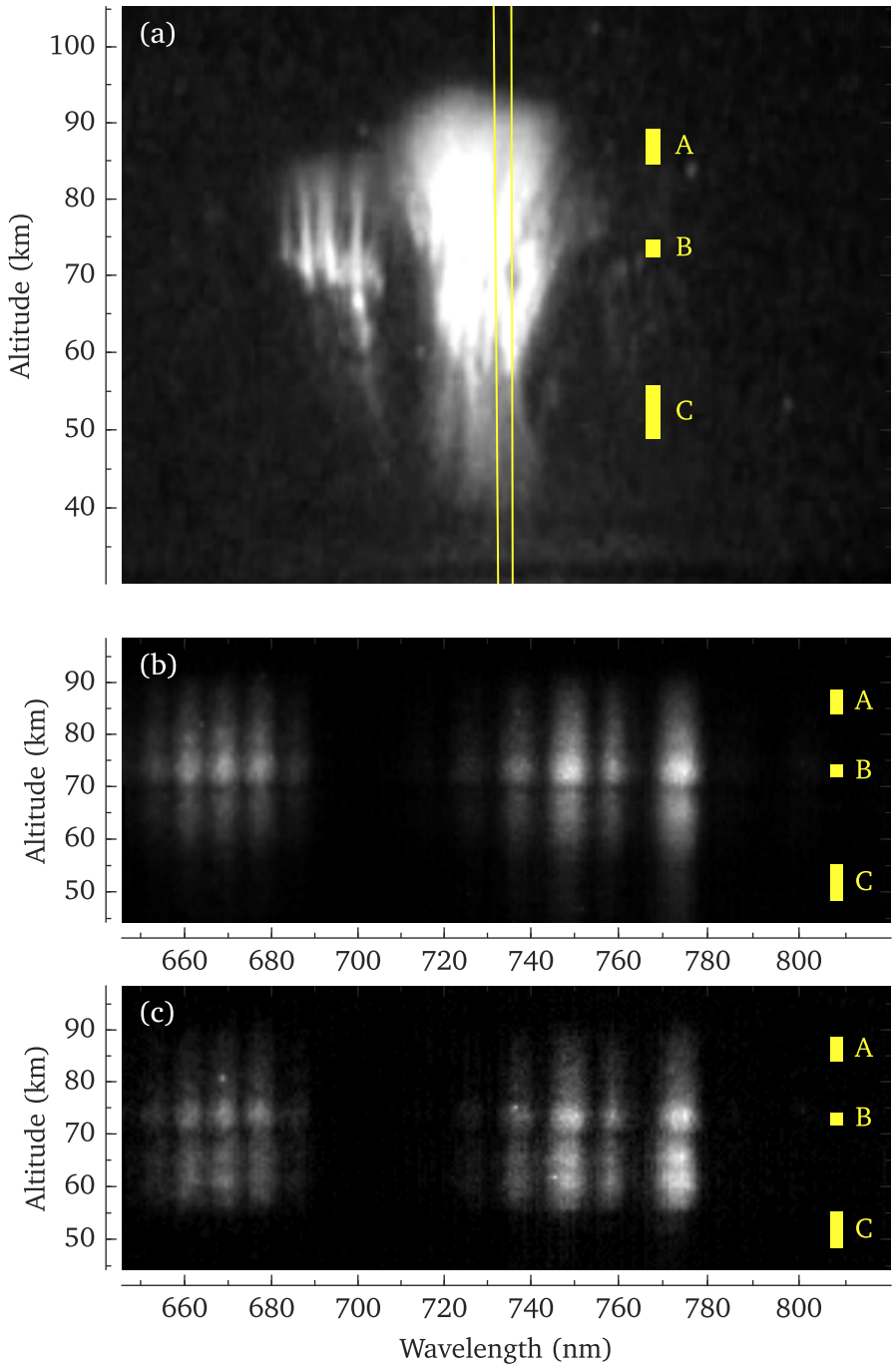

Figure 3.6. (a) Sprites at 08:42:35 UTC on 7 July 2005. Yellow lines in the center show the field of view of the spectrograph. Spectra were obtained from a carrot sprite in the center. (b) Spectrum in the first frame. (c) Spectrum in the second frame. Markers shows the altitude ranges where spectra are extracted for analysis.

3.4 Spectral Analysis

The altitude resolved spectra were examined in three different structures along the vertical extent of the sprites. Selected structures in the sprites are shown by yellow markers in Figure 3.5 and 3.6. For the sprite at 07:20:54 UTC, they are the upward branching structure between 77 and 80 km altitude, the transition between the body and upward branching structure between 70 and 73 km altitude, and the top portion of the body between 64 and 67 km altitude. For the sprite at 08:20:35 UTC, they are the upward branching structure 84 and 89 km altitude, the body between 72 and 74 km altitude, and the tendrils between 49 and 55 km altitude.

Spectra from the different structures of the sprites are shown in Figure 3.7 and 3.8. Figure 3.7 shows the spectra from the second frame in the event at 07:20:54 UT, and Figure 3.8 shows the spectra from the first frame in the event at 08:42:35 UT. These spectra were extracted from the image data by correcting for the instrument response and by integrating the rows corresponding to the altitude ranges.

The observed spectra are mainly composed of the First Positive system without any obvious indication of the Meinel system. The major features from 650 to 690 nm and those from 710 to 780 nm are the $\Delta v = 3$ ($v' = 3$ to 7) and $\Delta v = 2$ ($v' = 2$ to 7) sequences of the First Positive system, respectively. The minor features near 800 nm are the $\Delta v = 1$ ($v' = 6$ to 7) sequence of the First Positive system. There are the $\Delta v = 2$ and $\Delta v = 3$ sequences of the Meinel system from 690 to 730 nm and from 780 to 810 nm, respectively. These Meinel bands, however, overlap the nearby First Positive bands, making it difficult to distinguish respective emissions. From visual inspection, I found no obvious indication of the Meinel bands in the observed spectra.

The First Positive bands observed in the different sprite structures show some variations, implying that the vibrational distribution of the upper state varies along the vertical extent of the sprites. The variations in the First Positive bands are clearly seen in the intensity of the (4–2) band relative to that of the (2–0) band.

The possible presence of the Meinel bands and the variation of the vibrational distribution were examined with synthetic spectra. The procedure of the spectral analysis employed here is based on those used in the previous sprite studies [*Morrill et al.*, 1998; *Bucsela et al.*, 2003]. Spectral features included in the synthetic spectra were molecular band progressions—each of which is a set of the molecular bands with a common upper vibrational level—of the First Positive system. They were composed of 13 bands with upper vibrational levels $v' = 2$ to 7: (2–0), (3–1), (3–0), (4–1), (4–2), (5–2), (5–3), (6–3), (6–4), (6–5), (7–4), (7–5), and (7–6) bands. The shape of each vibrational band was computed from individual rotational lines (Section 2.2),

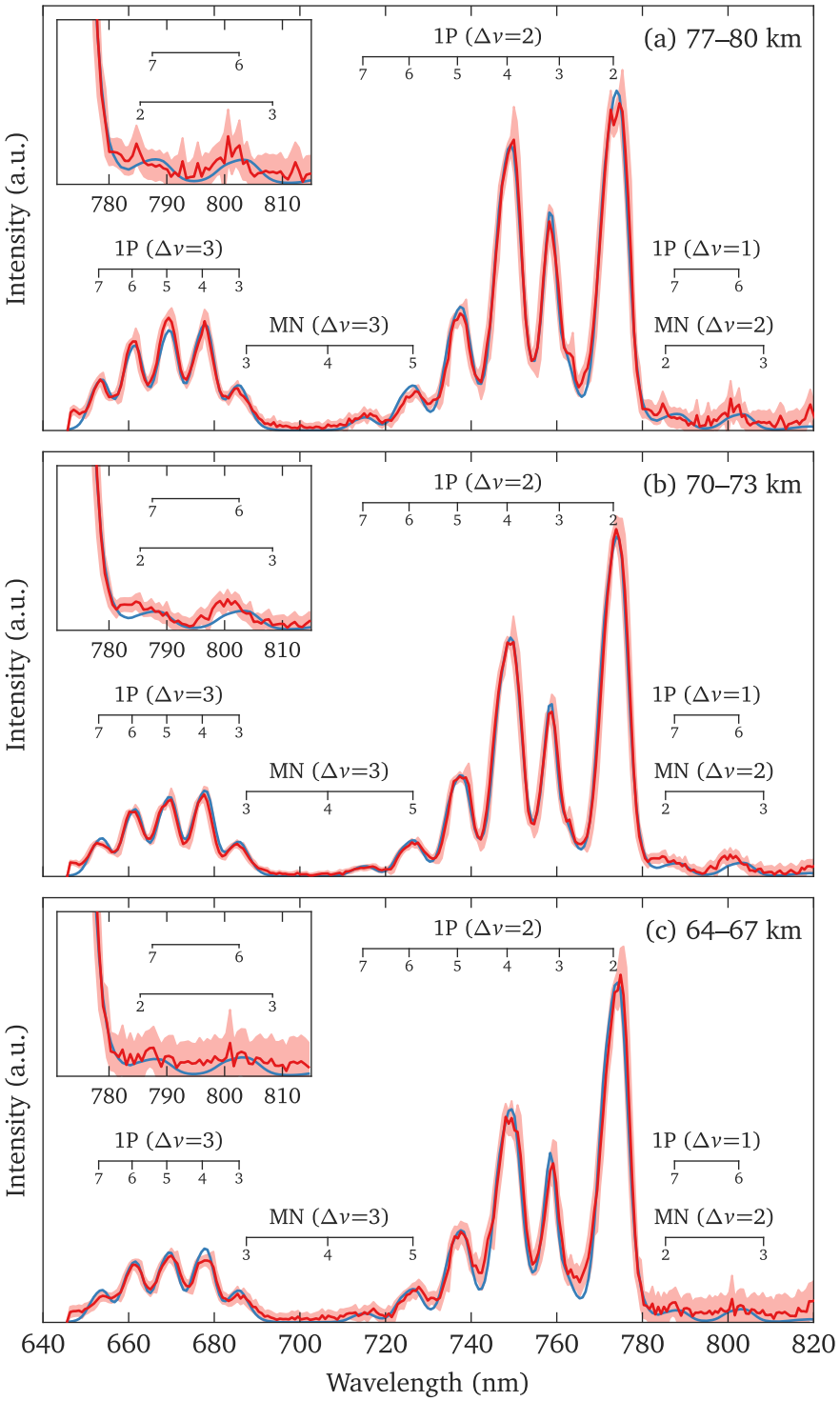

Figure 3.7. Spectra from different structures of the sprite at 07:20:54 UTC on 7 July 2005: (a) the upward branching structure between 77 and 80 km altitude; (b) the transition between the body and the upward branching structures between 70 and 73 km altitude; (c) the body between 64 and 67 km altitude. Red curves with associated shaded areas show the observed data with uncertainties. Blue curves show the synthetic spectra best fitted to the data.

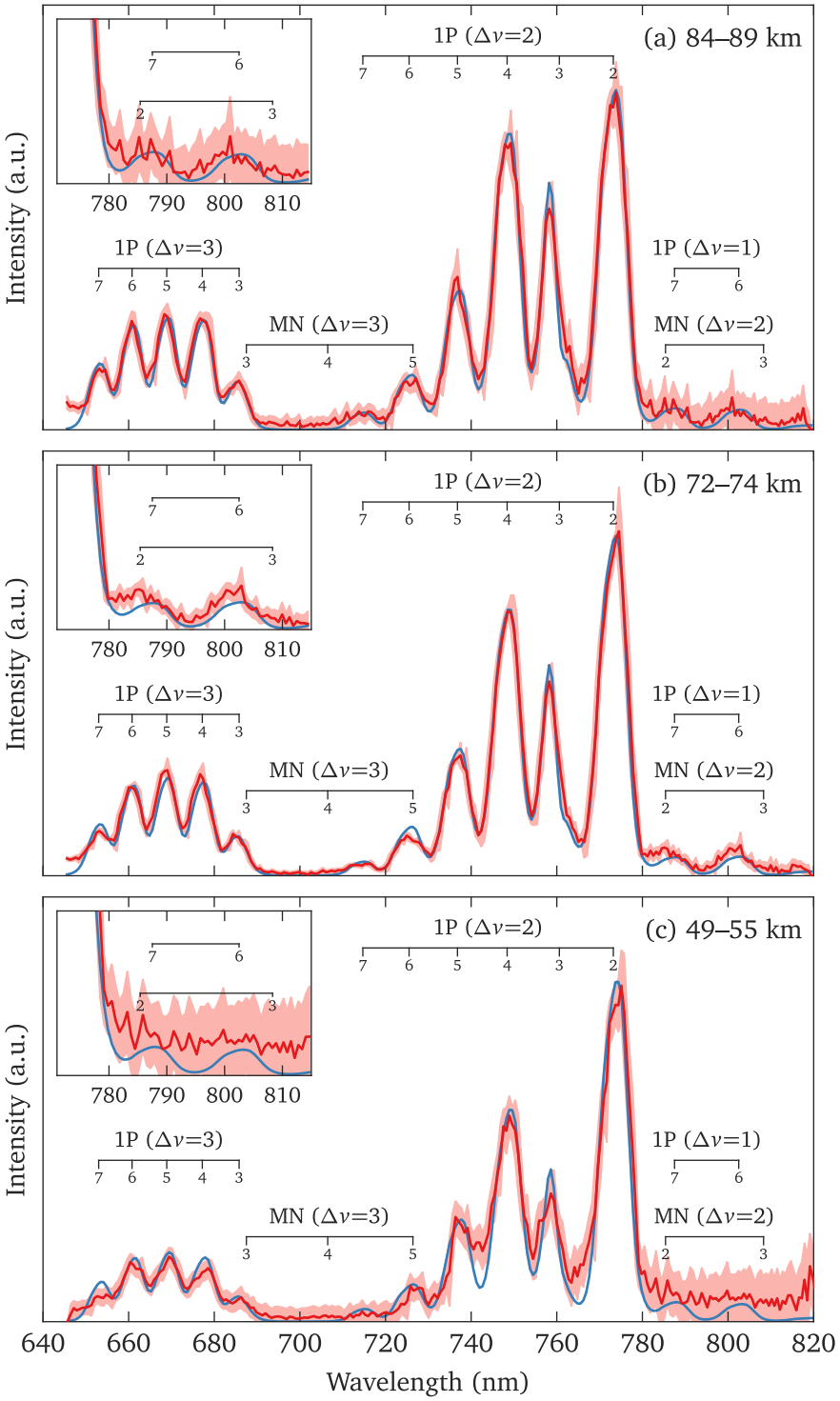

Figure 3.8. Spectra from different structures of the sprite at 08:42:35 UTC on 7 July 2005: (a) the upward branching structures between 84 and 89 km altitude; (b) the body between 72 and 74 km altitude; (c) the tendrils between 49 and 55 km altitude. Red curves with associated shaded areas show the observed data with uncertainties. Blue curves show the synthetic spectra best fitted to the data.

and the intensities of the rotational lines were then scaled with the atmospheric transmittance, which was calculated from the MOSART code for each viewing geometry (Section 2.3). The attenuated spectra were convolved with the instrument broadening given by Equation 3.1.

The synthetic spectra were fitted to the observed spectra. It was performed by scaling the intensities of the band progressions to minimize the chi-square of the fitting using a non-linear least square fitting routine. The weights for the least square fitting routine were based on the uncertainties of the measurements, and the wavelength scales were stretched by a small amount but less than the spectral resolution to improve spectral alignment. The synthetic spectra best fitted to the observed spectra are shown with blue curves in Figure 3.7 and 3.8.

The rotational temperature of all synthetic bands were assumed to be 230 K [*Morrill et al.*, 1998; *Bucsela et al.*, 2003]. To validate this assumption, the observed spectra were fitted with spectra synthesized at different rotational temperatures. One of the results of the spectral fitting is shown in Figure 3.9. The synthetic spectra at 230 and 300 K are both nicely fitted to the data, and the fits are qualitatively the same. But the synthetic spectrum at 800 K is poorly fitted to the data. The spectral resolution of about 3 nm does not permit accurate determination of rotational temperature, but overall the observed spectra are consistent with rotational temperatures up to 300 K. This implies that the plasmas induced by the sprites are indeed weakly ionized and therefore are non-thermal.

3.5 Presence of the N_2^+ Meinel Emission

The fits indicate that the signals from the Meinel emission are below or comparable to the noise level. Overall, the observed spectra were nicely reproduced by the fits, indicating no or little indication of the Meinel bands. Two humps near 785 to 800 nm observed in the transition region of the sprite at 07:20:54 UTC (Figure 3.7b) and in the body of the sprite at 08:42:35 UTC (Figure 3.8b) were not fully reproduced by the fits, and the residuals near 785 nm could be attributed to the (2–0) Meinel band because its band origin is at 785.4 nm. Nevertheless, the residuals are only marginally larger than the uncertainties of the measurements, and it is also possible that the residuals are merely artifacts introduced by calibration errors. Therefore, I concluded that the signals from the (2–0) Meinel band in the two spectra are, at most, comparable to the noise level. There are also the Meinel bands between 690 to 730 nm, but I do not find any indication of the ionization bands in the observed spectra.

Based on the noise levels and the residuals of the fits, the upper limit of the signals from the (2–0) Meinel band was inferred to be 3 to 7% of the (2–0) First Positive band. For the sprite

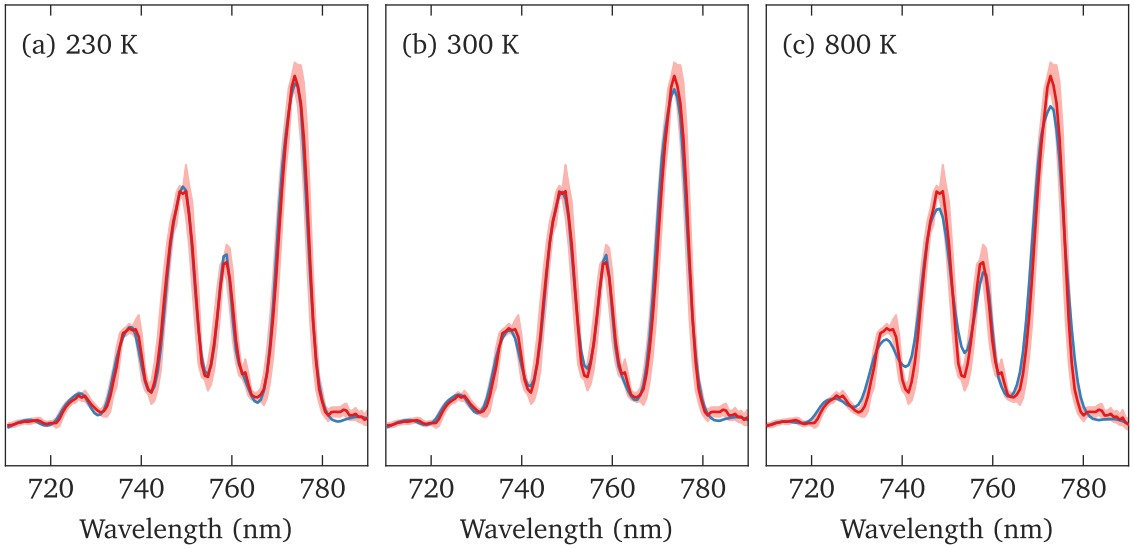

Figure 3.9. Synthetic spectral fitting with different rotational temperatures at 230, 300 and 800 K. The observed spectrum from the transition region of the sprite at 07:20:54 UT was fitted with synthetic spectra at different rotational temperatures. Red curves with associated shaded areas show the observed data with uncertainties. Blue curves show the synthetic spectra best fitted to the data.

at 07:20:54 UT, the upper limits are 3% in the upward branching structures between 77 and 88 km altitude, 3% in the transition region between 70 and 73 km altitude, and 4% in the body between 64 and 67 km altitude. For the sprite at 08:42:35 UT, the upper limits are 5% in the upward branching structures between 84 and 89 km altitude, 3% in the body between 72 and 74 km altitude, and 3% in the tendrils between 49 and 55 km altitude.

The upper limit of the (2–0) Meinel band indicates that the population of $N_2^+(A^2\Pi_u^+, v=2)$ is, at most, about 3 to 7% of $N_2(B^3\Pi_g, v=2)$. The transition probabilities of the (2–0) Meinel and the (2–0) First Positive bands are comparable: $4.02\times10^4\,s^{-1}$ for the (2–0) Meinel band and $4.29\times10^4\,s^{-1}$ for the (2–0) First Positive band [*Gilmore et al.*, 1992]. This means that the relative intensity of the (2–0) Meinel band with respect to the (2–0) First Positive band is roughly equivalent to that of the relative population of the upper levels. Hence, the upper limit of the relative band intensity indicates that the upper limit of the relative population of $N_2^+(A^2\Pi_u^+, v=2)$ with respect to $N_2(B^3\Pi_g, v=2)$ is roughly 3 to 7%.

The relative population of $N_2^+(A^2\Pi_u^+, v=2)$ was examined with a plasma kinetic model, which is based on those used for interpreting observed sprite emissions in previous studies [*Kuo et al.*, 2005, 2008; *Adachi et al.*, 2006]. The model simulates the populations of relevant excited species under a steady state condition in a (zero-dimensional) volume of weakly-ionized air

plasmas under the influence of a constant electric field.

The populations of excited species were assumed to be governed by a set of simplified kinetic reactions: electron impact excitation and ionization of neutral molecules, radiative cascading, and collisional quenching. The electrons accelerated by the electric field collide with neutral molecules and produce excitation and ionization of the molecules. Some of the molecules in excited states may release their excess energy by emitting photons and transition into the lower energy level. The others may be collisionally quenched, transferring their excess energy to neutral molecules. The excited species included in the model were $N_2(B\,^3\Pi_g, v)$, $N_2(C\,^3\Pi_u, v)$ and $N_2{}^+(A\,^2\Pi_u^+, v)$. The reactions incorporated in the model are summarized in Table 3.1.

The set of the kinetic reactions provides a set of steady state equations for the populations of the excited species. The equation for the population $N_{v'}^{n'}$ of an excited species in a vibrational level v' in an excited state n' is given by

$$q_{v'}k^{n'}(E/N)Nn_e + \sum_m \sum_w A_{wv'}N_w^m - \sum_m \sum_w A_{v'w}N_{v'}^{n'} - Q_{v'}N_{n'}^{v'} = 0 \tag{3.2}$$

where $q_{v'}$ is the Franck–Condon factor between the ground state and the upper level v', $k^{n'}(E/N)$ is the rate coefficient for electron impact excitation of the state n' as a function of the reduced electric field E/N, n_e is the electron density, and $A_{v'v''}$ is the Einstein coefficient for spontaneous emission associated with the transition from the upper level v' to the lower level v''. The quantity $Q_{v'}$ is the quenching rate for the upper level v' and is expressed in a form of

$$Q_{v'} = k_{q,N_2}N_{N_2} + k_{q,O_2}N_{O_2}$$

where k_{q,N_2} and k_{q,O_2} are the rate coefficients for quenching of the upper level v' by N_2 and O_2, respectively, and N_{N_2} and N_{O_2} are the densities of N_2 and O_2, respectively.

By solving the steady state equation (Equation 3.2), the population $N_{v'}^{n'}$ of the excited species can be expressed as

$$N_{v'}^{n'} = \frac{q_{v'}k^{n'}(E/N)Nn_e + \sum_m \sum_w A_{wv'}N_w^m}{\sum_m \sum_w A_{v'w} + Q_{v'}}. \tag{3.3}$$

The first term in the nominator is the contribution of electron impact excitation or ionization, and the second term in the nominator is the contribution of radiative cascading from the upper levels. The cascading term is zero for $N_2(C\,^3\Pi_u, v)$ and $N_2{}^+(A\,^2\Pi_u^+, v)$ and is non-zero for $N_2(B\,^3\Pi_g, v)$ because of the electronic transition from $N_2(C\,^3\Pi_u, v)$, which forms the N_2 Second

Table 3.1. Reactions incorporated in the plasma kinetic model.

Reaction		Reference
Electron impact excitation		
$e^* + N_2(X\,^1\Sigma_g^+, v''=0) \rightarrow e + N_2(B\,^3\Pi_g, v')$		*Hagelaar and Pitchford* [2005][a]
$e^* + N_2(X\,^1\Sigma_g^+, v''=0) \rightarrow e + N_2(C\,^3\Pi_u, v')$		*Hagelaar and Pitchford* [2005][a]
Electron impact ionization		
$e^* + N_2(X\,^1\Sigma_g^+, v''=0) \rightarrow e + e + {N_2}^+(A^2\Pi_u, v')$		*Hagelaar and Pitchford* [2005][a]
Radiative cascading		
$N_2(B\,^3\Pi_g, v') \rightarrow N_2(A\,^3\Sigma_g^+, v'') + h\nu$	N_2 First Positive system	*Gilmore et al.* [1992]
$N_2(C\,^3\Pi_u, v') \rightarrow N_2(B\,^3\Pi_g, v'') + h\nu$	N_2 Second Positive system	*Gilmore et al.* [1992]
${N_2}^+(A^2\Pi_u, v') \rightarrow {N_2}^+(X\,^2\Sigma_g^+, v'') + h\nu$	${N_2}^+$ Meinel system	*Gilmore et al.* [1992]
Collisional quenching		
$N_2(B\,^3\Pi_g, v') + N_2 \rightarrow N_2 + N_2$		*Piper* [1988]
$N_2(B\,^3\Pi_g, v') + O_2 \rightarrow N_2 + O_2$		*Piper* [1992]
$N_2(C\,^3\Pi_u, v') + N_2 \rightarrow N_2 + N_2$		*Dilecce et al.* [2006]
$N_2(C\,^3\Pi_u, v') + O_2 \rightarrow N_2 + O_2$		*Pereira et al.* [2010]
${N_2}^+(A^2\Pi_u, v') + N_2 \rightarrow {N_2}^+ + N_2$		*Piper et al.* [1985]
${N_2}^+(A^2\Pi_u, v') + O_2 \rightarrow {N_2}^+ + O_2$		*Piper et al.* [1985]

[a] The rate coefficients were obtained by solving a Boltzmann equation for electrons in a weakly ionized air plasma using BOLSIG+ software [*Hagelaar and Pitchford*, 2005], with a set of electron collision cross sections compiled by A. V. Phelps (available at http://jila.colorado.edu/~avp/collision_data/).

Positive system.

Using the steady state solution, I computed the relative population of $N_2^+(A^2\Pi_u^+, v=2)$ with respect to $N_2(B^3\Pi_g, v=2)$. Dividing the population of the former by that of the later cancel out the air density N and electron density n_e in Equation 3.2. Hence, the relative population becomes a function of the reduced electric field E/N via the rate coefficients for electron impact excitation and ionization. The relative population also depends on altitude via the densities of N_2 and O_2.

The computation of the relative population requires various rate coefficients and constants; they are summarized in the following. The rate coefficients for electron impact excitation and ionization were obtained by solving a Boltzmann equation for electrons in a weakly ionized air plasma using BOLSIG+ software [*Hagelaar and Pitchford*, 2005], with a set of electron collision cross sections compiled by A. V. Phelps (available at http://jila.colorado.edu/~avp/collision_data/). I verified the results from BOLSIG+ by comparing with experimental electron swarm data [*Dutton*, 1975; *Davies*, 1983]. The rate coefficients for quenching of the excited species were obtained from the literature: $N_2(B^3\Pi_g)$, *Piper* [1988] and *Piper* [1992]; $N_2(C^3\Pi_u)$, *Dilecce et al.* [2006] and *Pereira et al.* [2010]; $N_2^+(A^2\Pi_u^+)$, *Piper et al.* [1985]. The Franck–Condon factors and the Einstein coefficients were obtained from [*Gilmore et al.*, 1992].

The relative populations of $N_2^+(A^2\Pi_u^+, v=2)$ computed at 60, 70 and 90 km altitude are shown in Figure 3.10. They are shown here as a function of the electric field normalized by the breakdown threshold E_k/N. The relative population at a given altitude increases with the electric field; the relative population for a given electric field decreases at lower altitudes, which is due to the quenching of the Meinel system.

The relative population at 60 km altitude simulates that in the tendrils, which are indeed produced by the downward propagating streamers (Section 1.2). The downward propagating streamers produce an impulsive ionization emission from the N_2^+ First Negative system, and the electric field responsible for the ionization emission has been reported [*Morrill et al.*, 2002; *Kuo et al.*, 2005; *Liu et al.*, 2006; *Adachi et al.*, 2006, 2008], though the reported values scatter considerably from the lowest $\approx E_k$ [*Morrill et al.*, 1998] to the highest $\geq 3E_k$ [*Liu et al.*, 2006]. Nevertheless, the model predicted that the relative population at $4E_k$ is about 3%, which is lower than the upper limit of 7% in the tendrils of the sprite at 08:42:35 UT.

The relative population at 70 km altitude simulates that in the body. The electric field in the body has been reported to be about E_k or less [*Morrill et al.*, 2002; *Adachi et al.*, 2006, 2008]. The model predicted that the relative population at E_k is about 0.1%, which is considerably

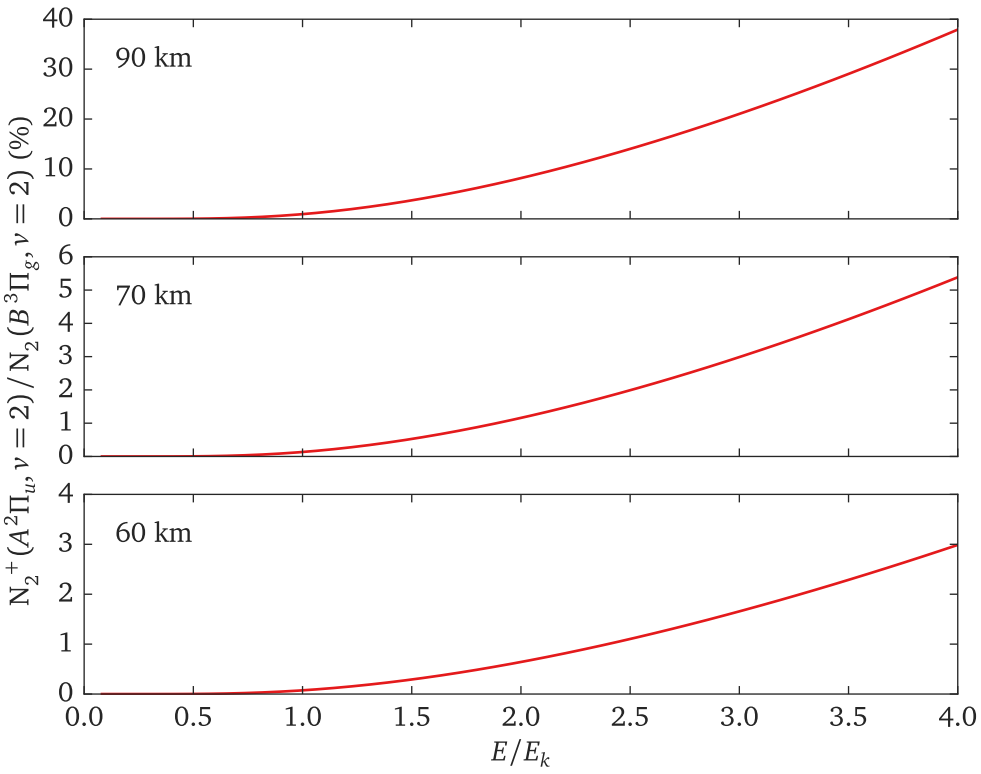

Figure 3.10. Modeled relative population of $N_2^+(A^2\Pi_u^+, v=2)$ with respect to $N_2(B^3\Pi_g, v=2)$ as a function of E/E_k at different altitudes.

lower than the upper limits of 4% in the body of the sprite at 07:20:54 UT and 3% in the body of the sprite at 08:42:35 UT.

The relative population at 90 km altitude simulates that in the upward branching structures, which are indeed produced by the upward propagating streamers (Section 1.2). The electric field in the upward branching structures has been reported to be somewhat smaller than or comparable to that in the body, which is about E_k [*Adachi et al.*, 2006]. The model predicted that the relative population at E_k is less than 1%, which is lower than the upper limit of 5% in the upward branching structures of the sprite at 08:42:35 UT.

The model results lend support to the conclusion that the signals from the (2–0) Meinel band in the observed spectra are, at most, comparable to the noise levels. The model predicted, at all altitudes considered, that the relative population of $N_2^+(A^2\Pi_u^+, v=2)$ with respect to $N_2(B^3\Pi_g, v=2)$ are substantially lower than the upper limits inferred from the noise levels and the residuals of the fits. This indicates that the (2–0) Meinel band emissions from the sprites were indeed very weak, and the signals from the ionization emissions were below the noise levels, consistent with no or little indication of the Meinel band in the observed spectra.

As mentioned in Section 3.1, *Morrill et al.* [1998] and *Bucsela et al.* [2003], in contrast, reported spectral features attributable to the Meinel system. These features were identified in the spectrum obtained from the tendrils at 57 km altitude, which is shown in Figure 3.1. The spectral data indicate that the relative population of $N_2^+(A^2\Pi_u^+, v=2)$ to $N_2(B^3\Pi_g, v=2)$ is about 27% [*Morrill et al.*, 1998, Table 4], which is significantly larger than the upper limit of 3 to 7% inferred in the present study. *Morrill et al.* [1998] and *Bucsela et al.* [2003] suggested that the collisional energy transfer between $N_2^+(A^2\Pi_u^+)$ and $N_2^+(X^2\Sigma_g^+)$ [*Katayama et al.*, 1980; *Katayama*, 1984] is a rapid process and may be responsible for the presence of the Meinel emission well below the quenthing altitude of 85 to 90 km. But the kinetic model employed in the present study predicted that the relative population is merely 0.1 to 3.0% at 60 km altitude, implying that the collisional energy transfer alone may not expain the observed relative population.

3.6 Altitude Variation of the $N_2(B^3\Pi_g)$ Vibrational Distribution

The fits determined the relative populations of the upper vibrational levels $v' = 2$ to 7. The population of the $v' = 3$ level is, however, not certain compared to those of the other levels because of the absorption of the (3–1) First Positive band by the (0–0) O_2 Atmospheric band. Therefore, the vibrational distribution reported here was defined as the relative populations normalized by the total population of the levels $v' = 2$ and 4 through 7. This normalization was applied not only to the distributions determined from the observed spectra but also to those obtained from the literature which will be mentioned in this section.

The vibrational distributions obtained from the sprite at 07:20:54 UTC are shown in Figure 3.11. The distribution in the transition region between 70 and 73 km altitude and that in the upper branching structure between 77 and 80 km altitude were determined from the data in the second and third frame. The distribution in the body between 64 and 67 km altitude was determined only from the data in the second frame because of the poor signal to noise of the data in the third frame. The observed distributions in the two successive frames remain essentially the same, indicating the excitation processes do not change over 6 ms. But the observed distributions in the different structures show variations; the relative populations of the $v' = 3$ level and higher decrease in the structures at lower altitude. Such variation along the vertical extent of the sprite is in agreement with previous reports [*Heavner*, 2000; *Bucsela et al.*, 2003].

The vibrational distributions obtained from the sprite at 08:41:35 UTC are shown in Fig-

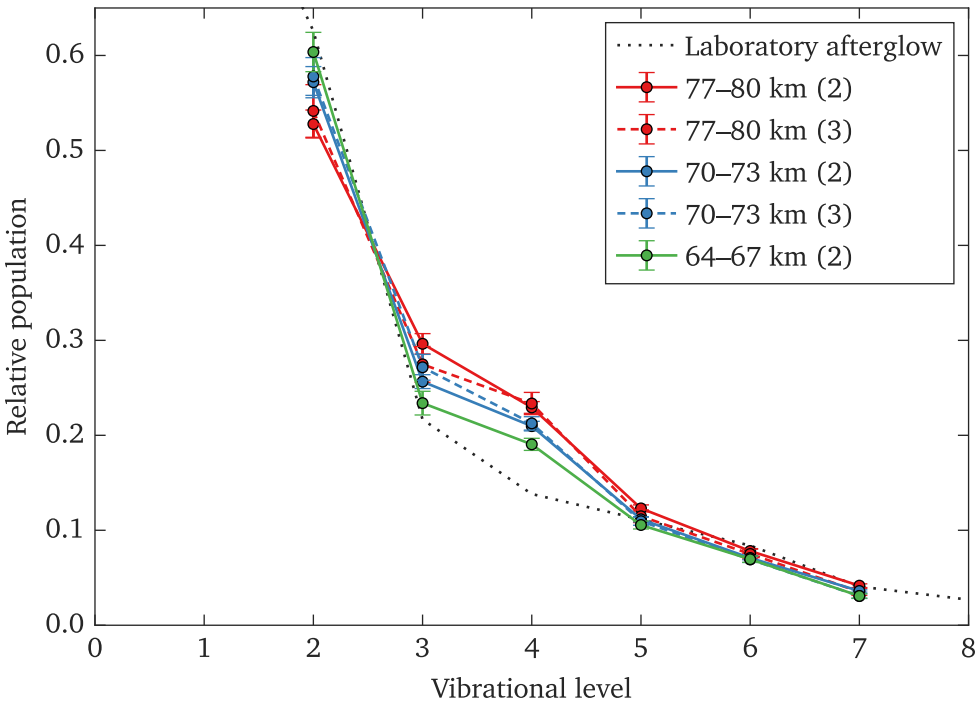

Figure 3.11. $N_2(B\,^3\Pi_g)$ vibrational distributions obtained from the sprite at 07:20:54 UTC. Solid lines show the data from the second frame, and dashes lines show the data from the third frame. A black dotted curve shows the distribution observed in laboratory afterglow in pure nitrogen at 200 mTorr [*Morrill and Benesch*, 1994].

ure 3.12. The distribution in the body between 72 and 74 km altitude was determined from the data in the first and second frame. The distribution in the tendrils between 49 and 55 km altitude and that in the upward branching structures between 84 and 89 km altitude were obtained only from the first frame because of the poor signal to noise in the data in the second frame. Again, the observed distributions in the two successive frames remain essentially the same, but those in the different structures show similar variations as seen above. Moreover, the observed distribution in the tendrils is in good agreement with the previously reported distribution in the tendrils at 53 km altitude [*Bucsela et al.*, 2003].

The observed vibrational distributions, in fact, vary with altitude. The altitude variation were examined with the intensity ratios of the (4–2) to the (2–0) First Positive band. They were computed from the data in the second frame in the event at 07:20:54 UT and the data in the first frame in the event at 08:42:35 UT. These data were corrected for the instrument response and the atmospheric transmittance; therefore, the variation of the intensity ratio roughly represents that of the relative population of the $v' = 4$ to the $v' = 2$ level. The intensity ratios as functions of altitude from about 50 to 90 km are shown in Figure 3.13. Although the

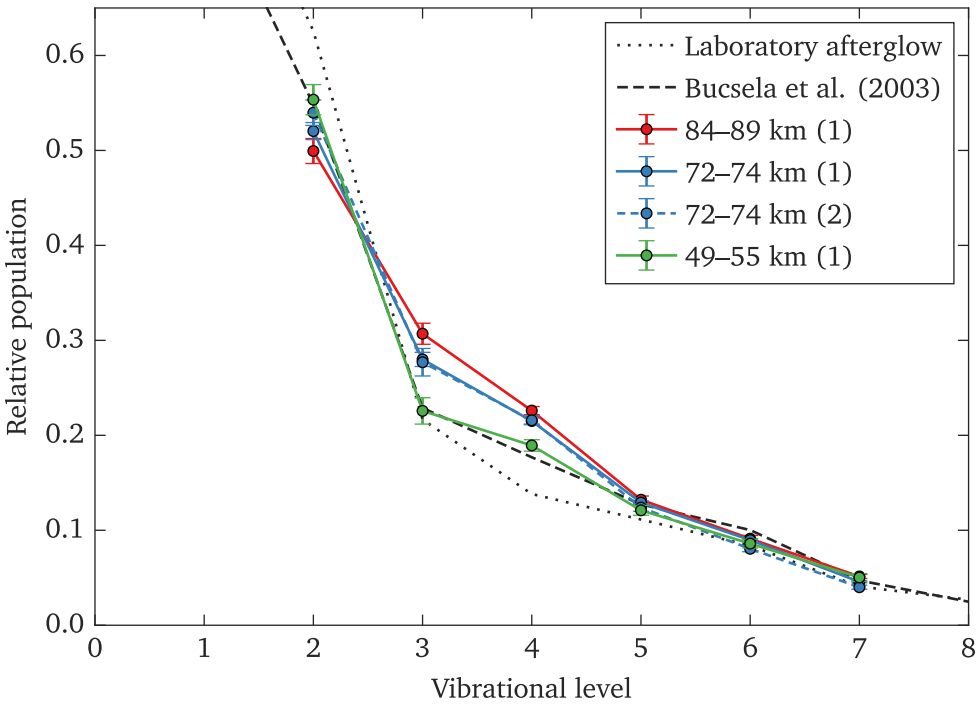

Figure 3.12. $N_2(B\,^3\Pi_g)$ vibrational distributions obtained from the sprite at 08:42:35 UTC. Solid curves show the data from the first frame, and a dashed curve shows the data from the second frame. A black dotted curve shows the distribution observed in laboratory afterglow in pure nitrogen at 200 mTorr [*Morrill and Benesch*, 1994]. A black dashed curve shows the previously reported distribution in the tendrils at 53 km altitude [*Bucsela et al.*, 2003].

altitude range includes different structures, the intensity ratios increases more or less linearly with altitude, indicating that the vibrational distributions vary with altitude.

The altitude variation indicates the ranking of the processes producing $N_2(B\,^3\Pi_g, v)$ varies with altitude, implying that collisional energy transfer processes are responsible for the observed vibrational distributions.

Bucsela et al. [2003] suggested that an energy transfer between vibrationally excited N_2 ground state $N_2(X\,^1\Sigma_g^+)$ and the low-lying metastable triplet state $N_2(A\,^3\Sigma_u^+)$ may be responsible for the production of $N_2(B\,^3\Pi_g, v)$ at lower altitudes. They pointed out that the vibrational distribution in the tendrils at 53 km altitude is similar to ones observed in laboratory afterglow. The afterglow distribution is indicative of an energy transfer process between $N_2(X\,^1\Sigma_g^+, v)$ and $N_2(A\,^3\Sigma_u^+)$, which is expressed as

$$N_2(A\,^3\Sigma_u^+, v = 0, 1) + N_2(X\,^1\Sigma_g^+, w \geq 5) \rightarrow N_2(B\,^3\Pi_g, v') + N_2(X\,^1\Sigma_g^+, w - 5) \tag{3.4}$$

Hence, the similarity to the afterglow distribution implies that the energy pooling process

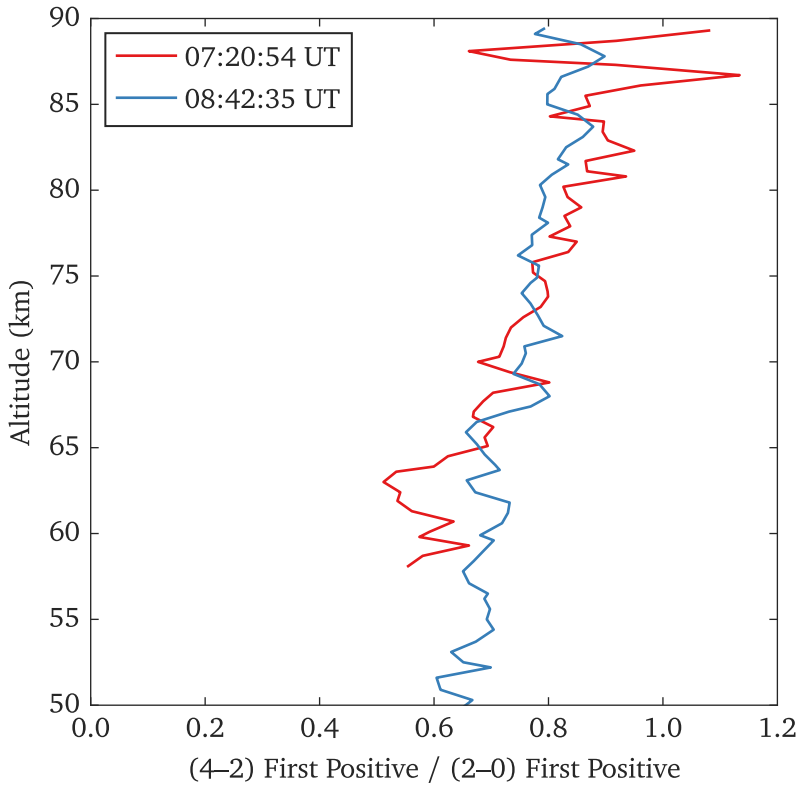

Figure 3.13. Altitude profiles of the intensity ratio of the (4–2) to the (2–0) First Positive band. The intensity ratios were computed from the observed spectra corrected for the instrument spectral response and the atmospheric transmittance.

plays a role in producing $N_2(B\,^3\Pi_g, v)$. In fact, the vibrational distributions observed in the present study become similar to the afterglow distribution at lower altitudes, which are shown in Figure 3.11 and 3.12.

Recent modeling study documented by *Gordillo-Vazquez* [2010], however, indicated otherwise; the energy pooling reaction suggested by *Bucsela et al.* [2003] is negligible in the production of $N_2(B\,^3\Pi_g, v)$. This and the subsequent study instead suggested that other types of collisional processes are responsible for the observe vibrational distribution.

Gordillo-Vazquez [2010] reported vibrational kinetics in sprites at 78 km altitude. This study incorporated a total of 84 species with more than 800 reactions, and simulated vibrational kinetics in a plasma after the passage of a sprite streamer. During the passage of the streamer, $N_2(B\,^3\Pi_g, v)$ is primarily produced by electron impact excitation of $N_2(X\,^1\Sigma_g^+, v = 0)$, and secondly by radiative cascading from $N_2(C\,^3\Pi_u, v)$. After the passage, $N_2(B\,^3\Pi_g, v)$ is mainly produced by intersystem collisional transfer, which couples vibrational populations of overlapping triplet states [*Morrill and Benesch*, 1994]; they are expressed as

$$N_2(W\,^3\Delta_u, v) + N_2 \longleftrightarrow N_2(B\,^3\Pi_g, v) + N_2 \tag{3.5}$$

$$N_2(A\,^3\Sigma_u^+, v) + N_2 \longleftrightarrow N_2(B\,^3\Pi_g, v) + N_2 \tag{3.6}$$

$$N_2(B'\,^3\Sigma_u^-, v) + N_2 \longleftrightarrow N_2(B\,^3\Pi_g, v) + N_2 \tag{3.7}$$

The intersystem collisional transfer processes persist for up to several milliseconds, indicating that these collisional processes may be responsible, to some extent, for the observed vibrational distributions. The altitude investigated in this study is above the quenching altitude of the First Positive system, and $N_2(B\,^3\Pi_g, v)$ is primarily destructed by radiative decay. But this is not the case at lower altitudes.

In the subsequent study, *Luque and Gordillo-Vázquez* [2011] reported vibrational kinetics in sprites at 55 km altitude. This study demonstrated that the quenching of $N_2(B\,^3\Pi_g, v)$ by N_2 and O_2 significantly affects the vibrational distribution, particularly at the lower altitudes where the $N_2(B\,^3\Pi_g, v)$ is primarily destructed by quenching instead of radiative decay. Furthermore, the model result with a carefully selected set of the quenching rate coefficients produced the vibrational distribution that is in good agreement with the observed vibrational distributions at about 55 km altitude [*Bucsela et al.*, 2003; *Kanmae et al.*, 2007].

From the results of these two modeling studies, I speculate that the underlying mechanism

of the altitude variation of the vibrational distribution is twofold. While the intersystem collisional transfer is responsible for the variation above the quenching altitude, the quenching of $N_2(B^3\Pi_g, v)$ is responsible for the variation below the quenching altitude. Both processes involve a neutral molecules as a colliding particle, and therefore becomes more effective at lower altitudes within the respective regions.

Chapter 4

Observations of Streamer and Columnar Glow Spectra

4.1 Introduction

Early photometric observations recorded precise time histories of emissions from different band systems using narrowband photometers. *Suszcynsky et al.* [1998] and *Armstrong et al.* [1998] showed that ionization emissions occurred impulsively at the onset, but neutral emissions persisted for a longer period of time. Later, *Armstrong et al.* [2000] reported that the signals from all band emissions increased simultaneously at the onset, but the duration of each signal was different: the N_2^+ First Negative ($B\,^2\Sigma_u^+ \rightarrow X\,^2\Sigma_g^+$) emission lasted about 140 μs, the N_2 Second Positive ($C\,^3\Pi_u \rightarrow B\,^3\Pi_g$) emission lasted about 1 ms, and finally the N_2 First Positive ($B\,^3\Pi_g \rightarrow A\,^3\Sigma_u^+$) emission persisted for a few ms or longer. These reports indicates that sprites develop roughly in two separate phases. The first occurs within the first millisecond of the onset and is associated with an energetic initiation process; the second persists for tens to hundreds of milliseconds and is associated with less energetic secondary processes induced by the initiation [*Suszcynsky et al.*, 1998].

The development in two separate phases parallels the sprite development documented by high-speed imaging studies. As discussed in Section 1.2, high-speed imaging studies have shown that sprites develop in two phases: the initial active phase within the first few ms of the onset where sprite streamers rapidly develop, and the quiescent phase persisting for 10 to 100 ms where a columnar glow slowly decays. Hence, the two separate phases associated with the emissions parallel those observed in the sprite development. This implies that the impulsive ionization emissions at the onset and the continuing neutral emissions are associated with sprite streamers and columnar glows, respectively.

The photometric observations alone, however, did not establish hard evidence of these associations. This is because the measurements did not have sufficient resolution to examine the spatial information associated with the emissions. Other types of the measurements were needed to study the spatial variations of the emissions and to test the associations presumed from the temporal variations of the emissions.

To spatially resolve relevant band emissions from sprites, *Morrill et al.* [2002] made airborne multi-color imaging observations. The observations simultaneously recorded the N_2 Second Positive and N_2^+ First Negative emissions using intensified video cameras with narrow passband filters. While the video recording limited temporal resolution, the airborne imaging with narrowband filters provided altitude profiles of the band emissions with spatial resolution

improved over the previous photometric observations.

The multi-color imaging study indeed confirmed the association of the ionization emissions with sprite streamers and that of the neutral emissions with columnar glows. *Morrill et al.* [2002] reported that the N_2^+ First Negative emission was nearly constant at all altitudes, and the N_2 Second Positive emission was roughly constant in the tendrils but intensifies in the body. As mentioned in Section 1.2, the tendrils are produced by the emissions from sprite streamers, and the body is mainly produced by the emissions from a columnar glow. Hence, the altitude profiles indicate that the First Negative emission was primarily associated with sprite streamers, and a large part of the Second Positive emission was associated with a columnar glow, confirming the associations presumed from the previous photometric observations.

Hence, the photometric and multi-imaging observations together indicate that sprite streamers are energetic initiation processes that primarily cause ionization in sprites, columnar glows are less energetic secondary processes that mainly produce the relatively long-lived neutral emissions. The excitation threshold energy of the N_2^+ First Negative system is about 8 eV higher than that of the N_2 Second Positive system and is about 11 eV higher than that of the N_2 First Positive system. Accordingly, the presence and absence of the ionization emission suggests the ranking of the underlying electron energies: the electron energy in sprite streamers is higher than in columnar glows.

To investigate the ranking of the electron energies in sprite streamers and columnar glows, we built a slitless spectrograph. Slitless spectroscopy is a classical technique commonly used in astronomy (Figure 4.1). Since stars and meteors are point sources, a transmission grating in front of a camera lens works as a spectrograph without a slit and a collimating unit. In sprites, streamers and columnar glows are essentially point and line sources, respectively, in typical viewing geometries, making them ideal targets for slitless spectroscopy.

In this chapter, I present results from airborne spectral observations made, in the summer of 2009, with the slitless spectrograph. The slitless spectrograph was first used in ground-based observations made in the summer of 2007. The observations successfully provided spectra from individual streamers and columnar glows, but no blue emission was observed due to the severe atmospheric attenuation along the long lines of sight from the ground [*Kanmae et al.*, 2010]. To minimize the atmospheric attenuation and to observe blue emissions from sprites, the 2009 observations were made from the NSF sponsored High-performance Instrumented Airborne Platform for Environmental Research (HIAPER) aircraft maintained and operated by NCAR.

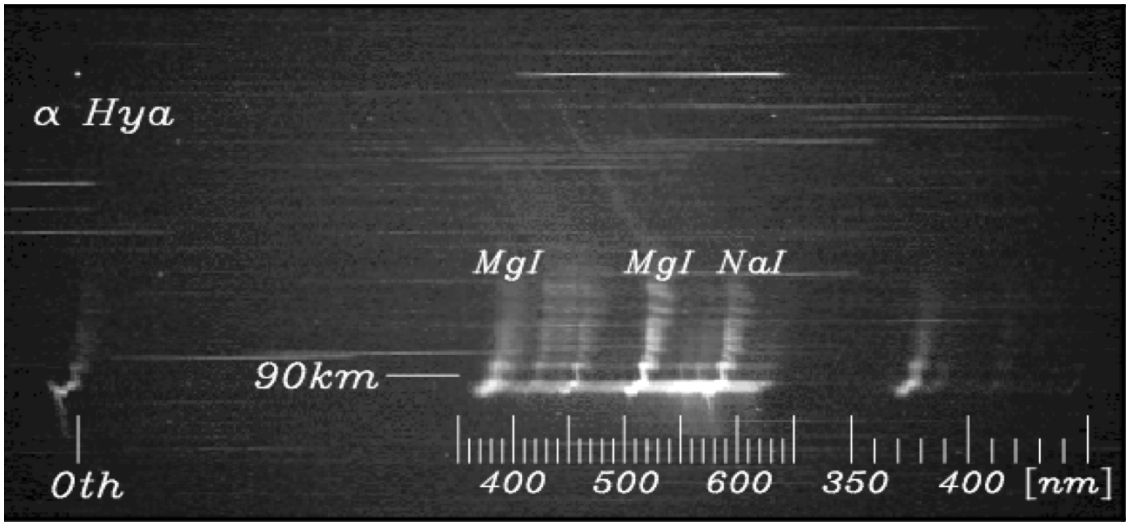

Figure 4.1. Slitless spectroscopy of a star and a persistent train of a meteor. Features near the top is a star α Hya and its spectrum, and those near the bottom is a persistent train of a meteor and its spectrum. Note that the persistent train spectrum clearly shows both the first order and second order. This image was reproduced from [*Abe*, 2000].

4.2 Instrumentation

An intensified CMOS imaging spectrograph was used to measure emission spectra from sprites. This spectrograph is slitless; it was built with a transmission grating and an imaging unit capable of recording images at a frame rate of 10 000 fps and higher, which had been used in previous high-speed sprite imaging observations [*McHarg et al.*, 2007; *Stenbaek-Nielsen et al.*, 2007].

The forefront optics of the spectrograph is a transmission grating with groove spacing of 100 lines/mm blazed at 425 nm. The diffracted light from the grating is focused by a front lens (Nikon 50 mm f/1.4) on an image intensifier (Video Scope VS4-1845HS) which has extended blue response and a P24 phosphor with a decay time of 10 μs, preventing persistence of the image signals carried on to the following image. The image from the intensifier is then reduced via a relay optics to fit the CMOS chip of a high-speed camera (Vision Research Phantom v7.0). The CMOS chip has 800 × 600 pixels with a dynamic range of 12 bits (4096 gray levels), though an actual image size is software configurable; for the data presented here, it was set to 640 × 256 pixels, which provided a field of view of 15.0° × 6.0°. The camera was synchronized with a IRIG-B time code from a GPS receiver, and the GPS time was stamped at the end of the integration time of each image.

The data acquisition was controlled from a laptop computer. For the data presented here, images were recorded at a frame rate of 10 000 fps with 50 μs exposures. The short exposure

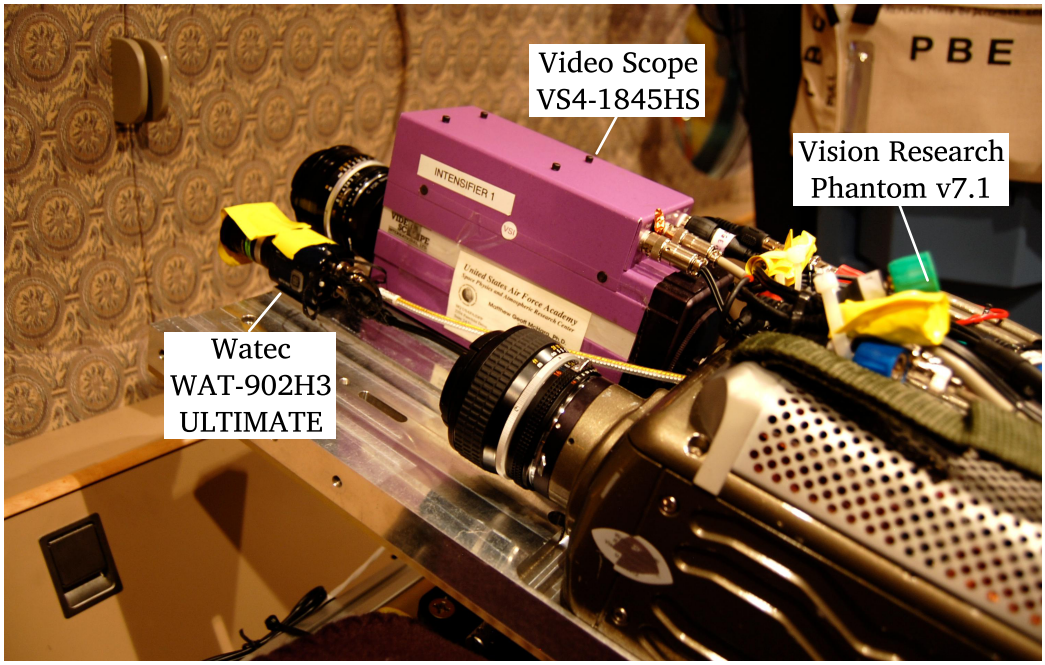

Figure 4.2. Instrument setup inside the HIAPER aircraft.

at the beginning of each image was set by an electronic shutter on the intensifier to minimize "smearing" due to the fast temporal development of sprites. Images were continuously recorded in an internal memory of the camera with a capacity of 2 GB, equivalent to 8647 frames*. The memory was configured as a circular buffer, which means that unless the data are transferred and stored to a disk, the buffer will be overwritten and the data will be lost. The data were saved with a computer program provided by the camera manufacture; it halts recording by triggering a single command and transfers and stores the data to a hard disk drive of the computer.

Along with the spectrograph, a CCD video camera (Watec WAT-902H ULTIMATE) was used to record sprites and the background stars. It has a field of view of 31.3° × 22.4° with a 12 mm lens, and operates at a normal video frame rate of 30 fps. The video from the camera was routed to a video time inserter (KIWI-OSD) where time from a GPS receiver inserted on each frame. The time inserted video was then recorded on a MiniDV tape recorder and displayed on a LCD monitor. The video on the LCD monitor provided scene awareness and allowed to aim the spectrograph accurately. As discussed in the previous chapter (Section 3.2), the background stars recorded in the video provided the pointing directions for the instruments.

The spectrograph and the video camera were co-aligned on an azimuth–elevation mount looking through a left side aircraft window. The alignment of the two instruments was estab-

*The full length of a recording time was about 0.86 s.

lished from star fields. Star fields were recorded at the beginning and the end of every night of observation with the spectrograph running at a slow frame rate of 100 fps and with the video camera. The recorded star fields provided accurate alignment between the two instruments.

The spectrograph was calibrated from measurements made during the observation period. The wavelength scale was determined from measurements of a portable calibration source (Ocean Optics HG-1 Mercury Argon Calibration Source). The measurements were made on the ground. The calibration source was placed distant from the spectrograph so that it became essentially a point source, and was measured at 18 different incident angles to provide enough data for the calibration.

The wavelength scale depends on the incident angle of light with respect to the grating or, to put it differently, the position of the zero order spectrum in an image. With an x-axis along the dispersion direction on an image, the wavelength scale of the first order spectrum at x is a function of position x_0 of the zero order spectrum, and it can be approximated as a polynomial of $x - x_0$. I found that the wavelength scale is well approximated by a linear function:

$$\lambda = a(x_0)(x - x_0) + b(x_0) \tag{4.1}$$

where λ is wavelength in nm, and $a(x_0)$ and $b(x_0)$ are polynomial functions of x_0. The polynomials were determined from the measurements; the individual spectra were fitted with a linear function of $x - x_0$, and the resultant linear coefficients were then used to determine $a(x_0)$ and $b(x_0)$. The value of the polynomial $a(x_0)$, the dispersion projected onto an image, is about 4.1 nm/pixel slightly varying with x_0.

The instrument response convolved with the aircraft window was determined from measurements of stars. The instrument response in the blue and red was determined from measurements of α UMa[†], which is a hot star with an effective temperature of 10 000 K and has strong blue emission. The strong blue emission, however, may produce signals from the second order spectrum in the near infrared, making it difficult to determine accurate values. To workaround the second order signals, the instrument response in the near infrared was separately determined from measurements of ϵ UMa, which is a cool star with an effective temperature of 4500 K and relatively weak blue emission. The weak blue emission produces a negligible amount of the second order signals. The spectra of the two stars were measured from an altitude of 14 km and at elevation angles of 10 to 14 degrees during a test flight.

[†]UMa refers to the constellation of Ursae Majoris, which is popularly known as the Big Dipper.

The measured spectrum of each star was corrected for vignetting of the optics and for background signals, and then divided by a reference spectrum of the star. The reference spectrum was modeled from a stellar spectrum tabulated in the Kurucz 1993 Stellar Atmospheres Atlas [*Kurucz*, 1992], which contains spectra computed from stellar atmosphere models for a wide range of metallicities, effective temperatures, and gravities. The spectrum from the atlas was scaled by the atmospheric transmittance for a given viewing geometry of the measurement, which was computed with the MOSART code [*Cornette et al.*, 1995]. The attenuated spectrum was then convolved with the instrument broadening of the measurement. The instrument broadening was determined from structured features in the measured spectrum, such as the hydrogen absorption lines and the atmospheric absorption bands, and was approximated by a Gaussian with the full width at half maximum of about 12 nm. The instrument response curves obtained from the two stars were connected at 720 nm, and then the resultant curve was smoothed to produce the "complete" instrument response.

The instrument response is shown in Figure 4.3. The spectral coverage is from about 400 to 900 nm peaked near 550 nm, with a relatively steep cut-off in the response at 400 nm. According to a measurement independently made by P. Jenniskens, the steep blue cut-off is due to the aircraft window transmission (P. Jenniskens, private communication, 2009).

4.3 Observations and Data

The observation campaign was made in August 2009 jointly with another mission, the Airborne Detector for Energetic Lightning Emissions (ADELE), out of Melbourne, Florida. While the summer season storms in Florida produce high lightning activity, it does not frequently produce sprites. In anticipation that it would be difficult to observe sprites over Florida, we flew over the High Plains where they frequently occur associated with large storm systems or MCSs (Section 3.3).

The storm activity during the observation period was monitored with meteorological data. The data included infrared imagery from the GOES satellites and lightning data from the NLDN (Section 3.3). Additional lightning data were made available by S. Cummer of Duke University. The data provided charge moment changes of cloud-to-ground lightning strokes, which were determined from remote sensing of ELF waves radiated from the lightning strokes. As mentioned in Section 1.1, sprites are normally produced by positive cloud-to-ground lightning strokes with large charge moment changes. Hence, the charge moment change data allowed us to pinpoint sprite-producing regions of storms, which was a notable improvement over our observation

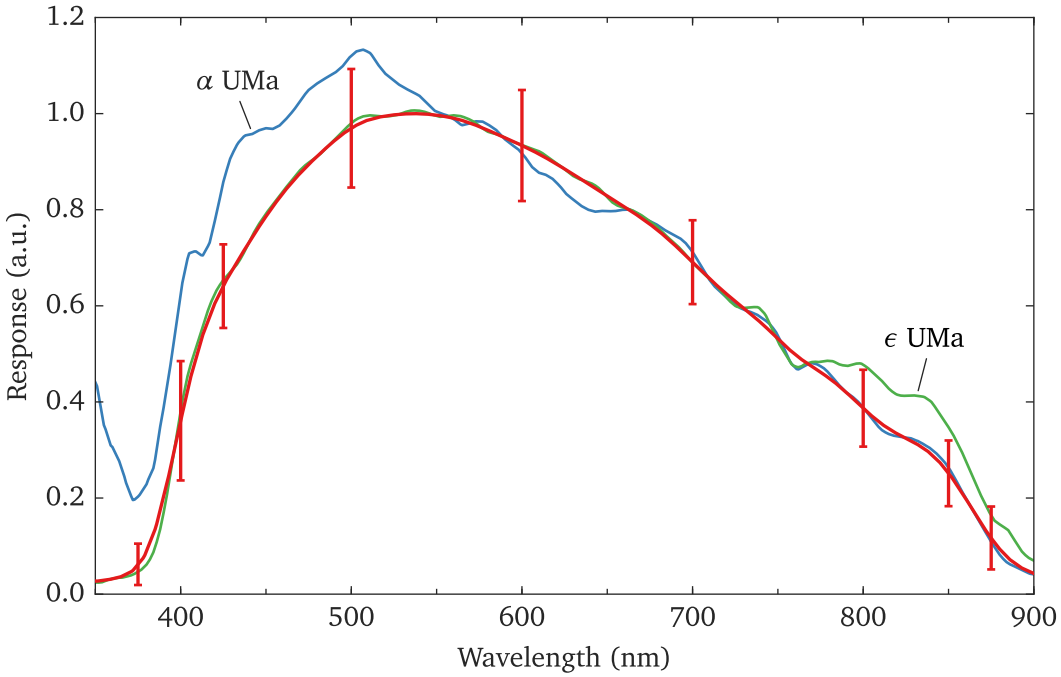

Figure 4.3. Instrument response of the spectrograph. Blue and green curves show the instrument response determined from measurements of α UMa and ϵ UMa, respectively. The two curves were connected at 730 nm, and the resultant curve was then smoothed to produce the instrument response shown in a red curve. The uncertainties in the instrument response are shown at selected wavelengths.

campaign in 2005.

These meteorological data were available near real-time via the Internet; this allowed us to make real-time flight planning on-board. We wanted to have sprites at an elevation angle of 20 to 30 degrees, which would position the aircraft about 200 to 300 km away from sprite-producing regions of storms. To keep the ideal distance, we normally flew on racetrack-like paths on the clear side of storm fronts so that the left side of the aircraft faced the storm on the near side leg. The flight path was adjusted as a storm drifted or different regions became active throughout the night. The cruising altitude was maintained near 14 km which significantly reduced atmospheric attenuation and allowed observation of blue emissions from sprites (Section 2.3).

Observations were made on three nights in August 2009, and spectra from 16 sprite events were recorded. All the events were recorded at elevation angles between 9 and 16 degrees, corresponding to path lengths of 200 to 310 km. Among the observed events, five events have well-defined spectra, and have been analyzed in detail. Blue emissions from streamers were observed in the five events, and those from columnar glows, however, were adequately extracted only in one event at 05:37:36 UT on 19 August. In the following, I present the data obtained from the event at 05:37:36 UT on 19 August and another event at 09:15:23 UT on 27 August.

The first event at 05:37:36 UT on 19 August was composed of two carrot sprites. On 19 August, sprites were observed above a large thunderstorm over northwest Oklahoma. The two sprites occurred following a positive cloud-to-ground lightning stroke at (36.062°N, 100.136°W), as reported by the NLDN, which provided a horizontal distance of about 280 km from the aircraft (Figure 4.4). The location of the parent lightning stroke was used to infer the altitude scale of the sprites, assuming that the center of the sprites is at the range of the lightning stroke (Section 3.3). The uncertainty associated with the altitude scale is about 4 km.

Of the two, the sprite to the left in the field of view provided data suitable for examining the initial stage of the sprite development. The two sprites observed with the video camera are shown in Figure 4.5, with the spectrograph's field of view covering large portions of both sprites. The sprite to the left started a few millisecond earlier than the sprite to the right. As a result, the spectra of the sprite to the right were overlapped with the spectra of remnant emission from the sprite to the left, making it difficult to separate them. On the other hand, the spectra of the sprite to the left were well isolated particularly in the initial stage of the sprite development.

The development of the sprite and its spectra is illustrated in Figure 4.6, with images of the zero and first order spectra in selected frames. The images were false-colored to enhance the visual dynamic range. The zero order position x_0 defines the shown wavelength scale, but

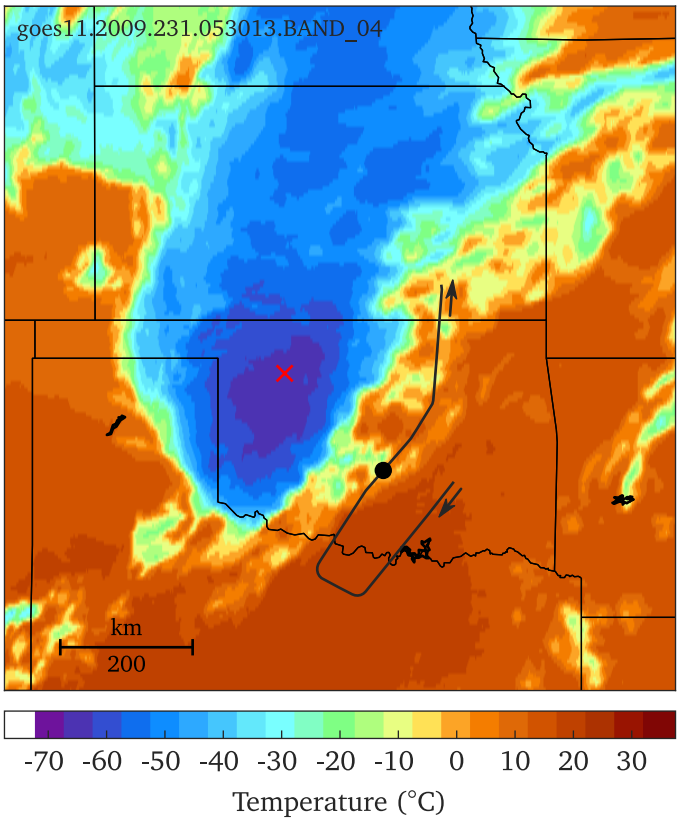

Figure 4.4. Observing geometry for the event at 05:37:36 UT on 19 August 2009. Ground track of the HIAPER aircraft is shown on top of the surface temperature map reproduced from the GOES-11 infrared image. The location of the aircraft at 05:37:26 UT, when the event was recorded, is shown by a dot, and the location of the parent lightning stroke, as reported by the NLDN, is shown by a cross.

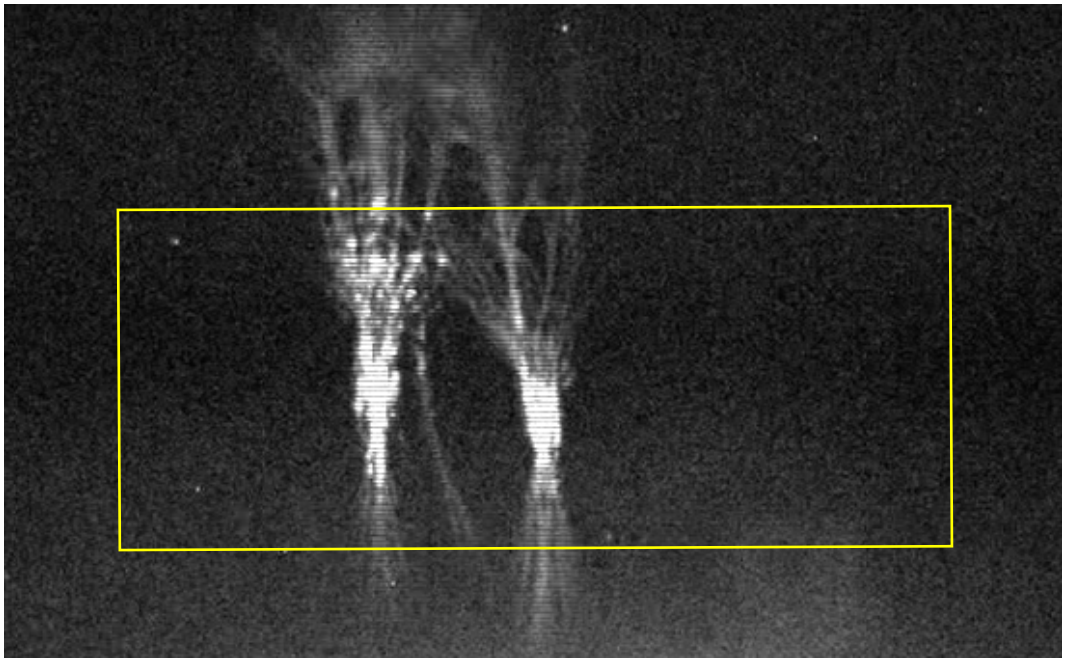

Figure 4.5. Sprites at 05:37:36 UT on 19 August 2009. The box shows the field of view of the spectrograph.

the wavelength scale for a spectrum of any feature is well approximated by shifting the shown scale by a distance between x_0 and the zero order position of the feature. For example, the wavelength scale in frame 15 refers to the columnar glow near the center, and the wavelength scale for the upward propagating streamer to the left can be approximated by adding about 30 nm to the shown scale.

Two weak spectral features between 650 and 800 nm were first observed in frame 3 in a downward propagating streamer, which initially appeared in frame 1 (not shown) at 75 km altitude out of the dark background. As the initial streamer moved downward and increased in brightness, the two features became brighter with two additional features near 600 and 880 nm. Furthermore, a weak spectral feature in the blue between 400 and 420 nm became visible in frame 6. The initial streamer split in frame 7 (not shown), and streamers spawned from the splitting proceeded further downward with subsequent splittings (e.g, frame 8 and 11).

On the trail of the initial streamer, a columnar glow became visible in frame 6 and increased in luminosity with time. Spectral features of the columnar glow developed similarly to those of the initial streamer: the spectral features between 650 and 800 nm were first observed in frame 8, and, those near 600 and 880 nm became visible later as the columnar glow became brighter. The spectral features in the blue between 400 and 420 nm became visible in frame 13. As the

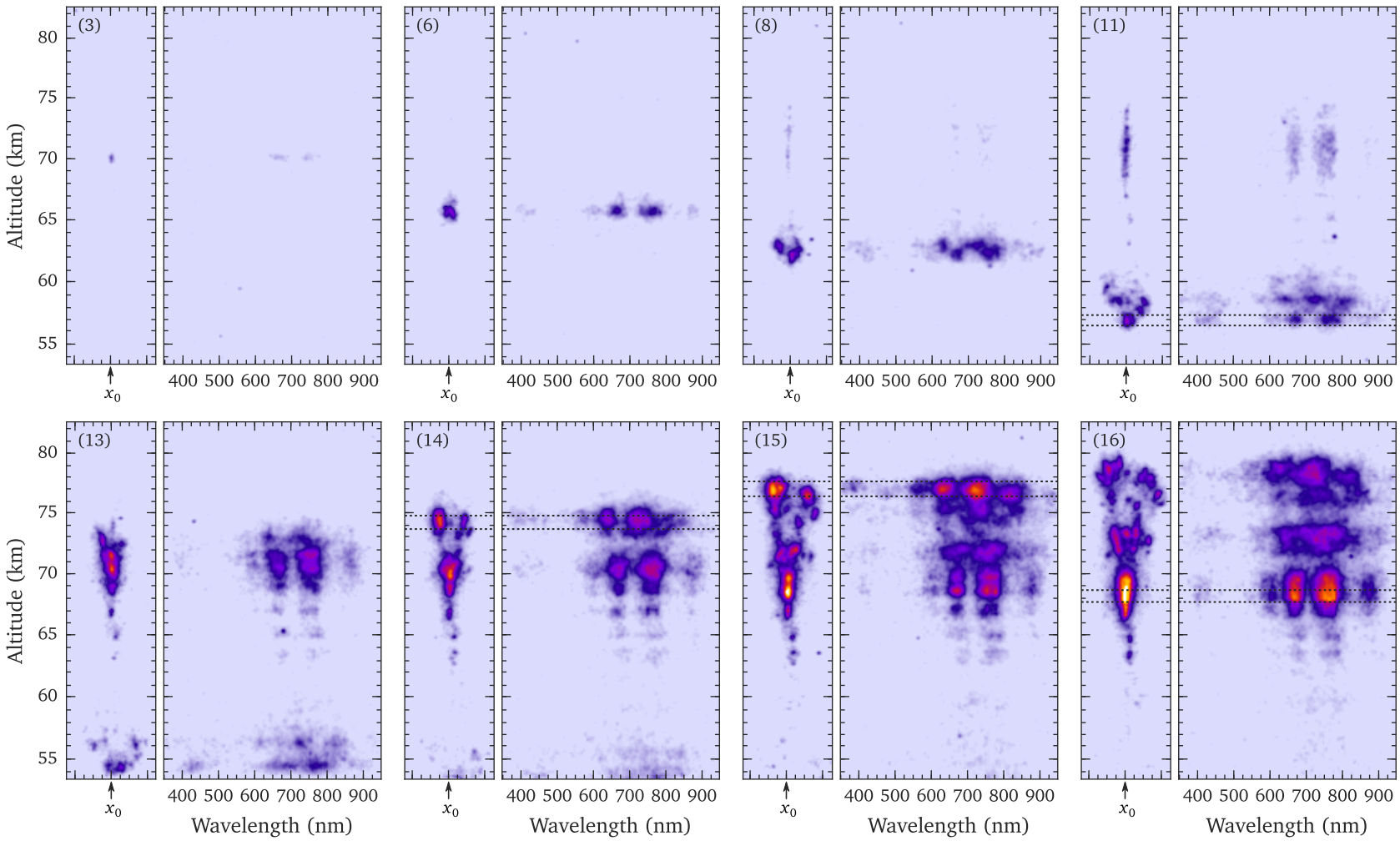

Figure 4.6. Spectra of the sprite at 05:37:36 UT on 19 August 2009. The images were recorded at a frame rate of 10 000 fps; they show the first order spectra with the corresponding zero order spectra. Dotted lines illustrate the regions where spectra were extracted for analysis.

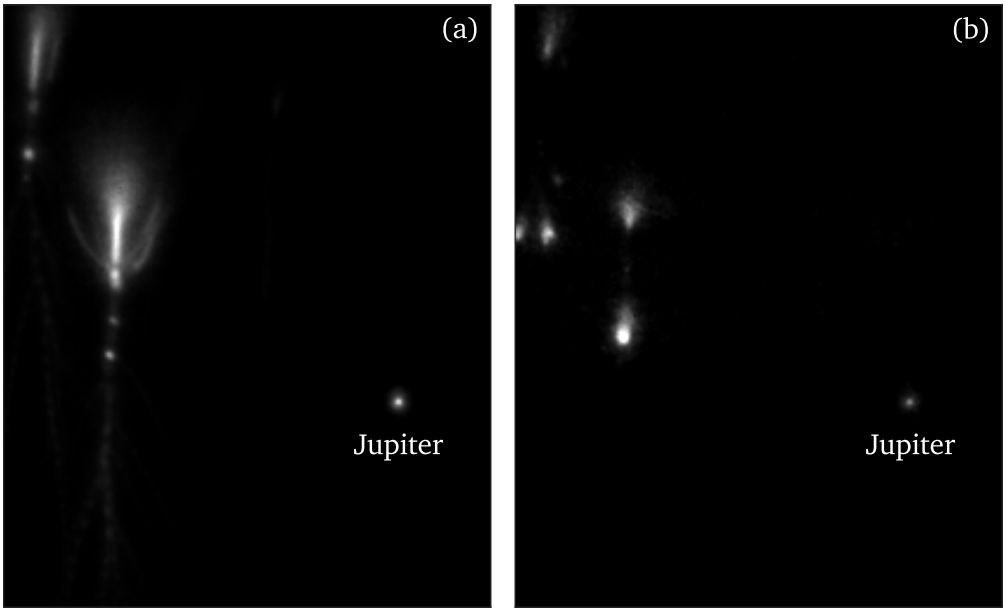

Figure 4.7. Sprites at 09:15:23 UT on 27 August 2009 observed with an intensified CMOS camera at a frame rate of 16 000 fps. (a) The image was created by averaging 2.5 ms of data. (b) An individual frame during the initial development of the sprites.

glow expanded both downward and sideways, upward propagating streamers launched from the upper part of the glow frame 14. The spectral features in the upward propagating streamers are the same as those observed in both downward propagating streamers and columnar glow. The upward propagating streamers expanded quickly and split into many in frame 16 and later.

The second event at 09:15:23 UT on 27 August was composed of six columnar sprites. On 27 August, sprites were observed above a large thunderstorm over the border between Oklahoma and Texas. The six sprites occurred following a positive cloud-to-ground lightning stroke at (34.623°N, 96.636°W), as reported by the NLDN, which provided a horizontal distance of about 190 km from the aircraft. As the case with the first event, the location of the parent lightning stroke was used to infer the altitude scale of the sprites. The uncertainty associated with the altitude scale is about 7 km.

Two of these sprites are shown in Figure 4.7. These images were observed with a high-speed intensified CMOS camera at a frame rate of 16 000 fps, which was co-aligned with the spectrograph during the night. Figure 4.7a was produced by averaging 2.5 ms of data to illustrate the spatial development of the sprites. The bright circular object to the right of the sprites is the planet Jupiter. In this time-averaged image, only the columnar glows are brighter than Jupiter. However, when compared in individual frames (e.g., Figure 4.7b), the

downward propagating streamers are indeed brighter than Jupiter, which is consistent with the emission rate of sprite streamers estimated by *Stenbaek-Nielsen et al.* [2007]. Although downward propagating streamers are very bright, they moved fast, traveling many pixels within the 2.5 ms. As a result, the streamers appear dimmer than stationary objects, e.g., Jupiter, in the time averaged image.

The development of the sprite to the right in the field of view and its spectra are illustrated in Figure 4.8, with images of the zero and first order spectra in selected frames. In contrast to the event at 05:37:36 UT on 19 August where a downward propagating streamer appeared to initiate out of the dark background, downward propagating streamers appeared to initiate from luminous patches within a preceding halo, another type of TLE, which is essentially descending diffuse glow of pancake-like shape [*Barrington-Leigh and Inan*, 1999]. As the halo descends, luminous patches formed within the originally unstructured halo. These patches slowly descended and became brighter (e.g., frame 1 and 3), and a downward propagating streamers eventually spawned from one of the patches in frame 4. Similar development of sprites has been reported by *Cummer et al.* [2006].

Two weak spectral features between 650 and 800 nm were first observed in frame 4 in the downward propagating streamer. As the initial streamer moved downward and increased in brightness, the two features became brighter with two additional features near 600 and 880 nm (frame 5). Furthermore, a weak spectral feature in the blue between 400 and 420 nm became visible in frame 7. The initial streamer split in frame 8 (not shown), and streamers spawned from the splitting proceeded further downward with subsequent splittings (e.g, frame 9 through 11).

The remnant of the luminous patch gradually increased in brightness and expanded both upward and downward forming a columnar glow. Spectral features of the columnar glow developed similarly to those of the initial streamer. The spectral features between 650 and 800 nm were first observed in frame 5, and those near 600 and 880 nm became visible as the glow became brighter. The spectral features in the blue between 400 and 420 nm became barely visible in frame 12. From the bottom of the glow, upward propagating streamers launched in frame 16 (not shown). They did not split as prolifically as those observed in event at 05:37:36 UT on 19 August. I speculate that pre-ionization produced by the preceding halo might suppress splittings of the upward propagating streamers [*Nijdam et al.*, 2011].

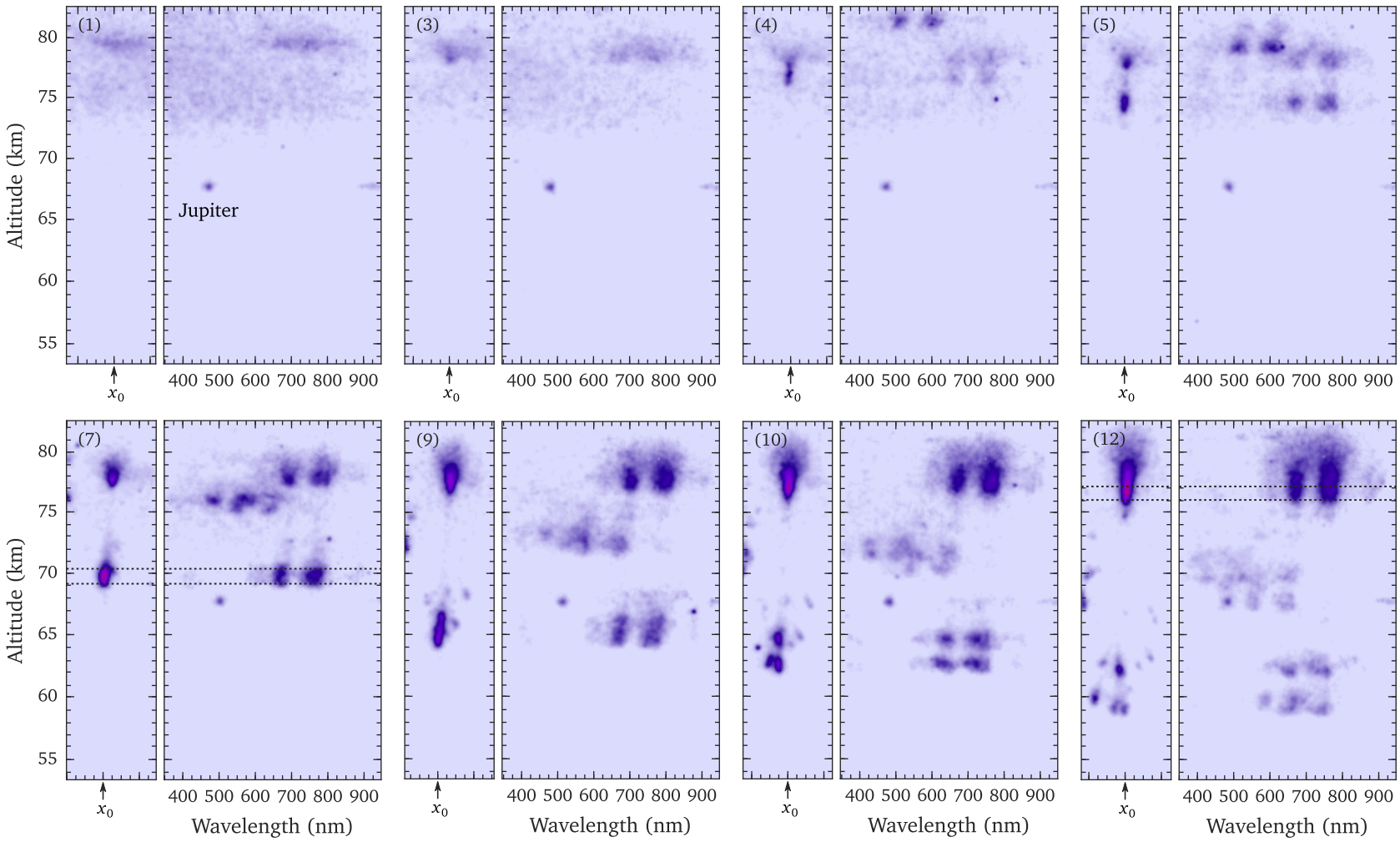

Figure 4.8. Spectra of the sprite at 09:15:23 UT on 27 August 2009. The images were recorded at a frame rate of 10 000 fps; they show the first order spectra with the corresponding zero order spectra. Dotted lines illustrate the regions where spectra were extracted for analysis.

4.4 Spectral Analysis

Spectra from one of the downward propagating streamers and the columnar glow in the sprite at 05:37:36 UT on 19 August are shown in Figure 4.9. They were extracted from an isolated streamer in frame 11 and the brightest segment of the glow in frame 16, both of which are shown with dotted lines in Figure 4.6. The image signals were vertically integrated to enhance the signal to noise, and the spectra were corrected for the instrument response. To identify differences in the blue, the spectra were then normalized so that the areas under the curves between 600 and 800 nm became the same. The spectral resolution was determined as the full width at half maximum of Gaussian fitted to the intensity curve of the zero orders; it is roughly 30 nm for both spectra.

The features in the visible and near infrared are primarily composed of the N_2 First Positive system. Both spectra have four features between 550 and 900 nm. The feature at 660 nm was identified as the $\Delta v = 3$ sequence of the First Positive system, that at 760 nm the $\Delta v = 2$ sequence, and that at 600 nm the $\Delta v = 4$ sequence. The feature at 900 nm was identified as the $\Delta v = 1$ sequence. This sequence is at the edge of the instrument response; consequently, the signals from this feature were very weak in the raw data (e.g., Figure 4.6 and 4.8) and were susceptible to noise. To verify the identification, I have performed synthetic spectral fitting of the First Positive system to the data. But it was not possible to obtain a good fit because of the coarse spectral resolution and the relatively large uncertainties in the measurements.

The features in the near ultraviolet and blue are composed of either the N_2 Second Positive system or a combination the N_2 Second Positive and the N_2^+ First Negative systems, but definite identification was difficult due to the large uncertainties. Both spectra have two features between 400 and 450 nm, though a sharp peak at 400 nm in the streamer spectrum is most likely due to the scintillation noise from the intensifier. These humps at about 400 nm and 420 nm were identified as the $\Delta v = -3$ and -4 sequence of the Second Positive system, respectively, both of which had been confirmed by previous spectral observations [*Heavner et al.*, 2010]. There are also the First Negative bands, which are the (1–0) band at 388.2 nm, the (0–0) band at 391.2 nm, the (1–2) band at 423.4 nm, and the (0–1) band at 427.8 nm. To verify the identification of the Second Positive bands and to examine the presence of these First Negative bands, I have performed synthetic spectral fitting of these band systems to the data. But, again, it was not possible to obtain a good fit because of the coarse spectral resolution and the large uncertainties in the measurements particularly below 400 nm, which is due to the steep cut-off in the instrument response. As a result, none of the First Negative bands were

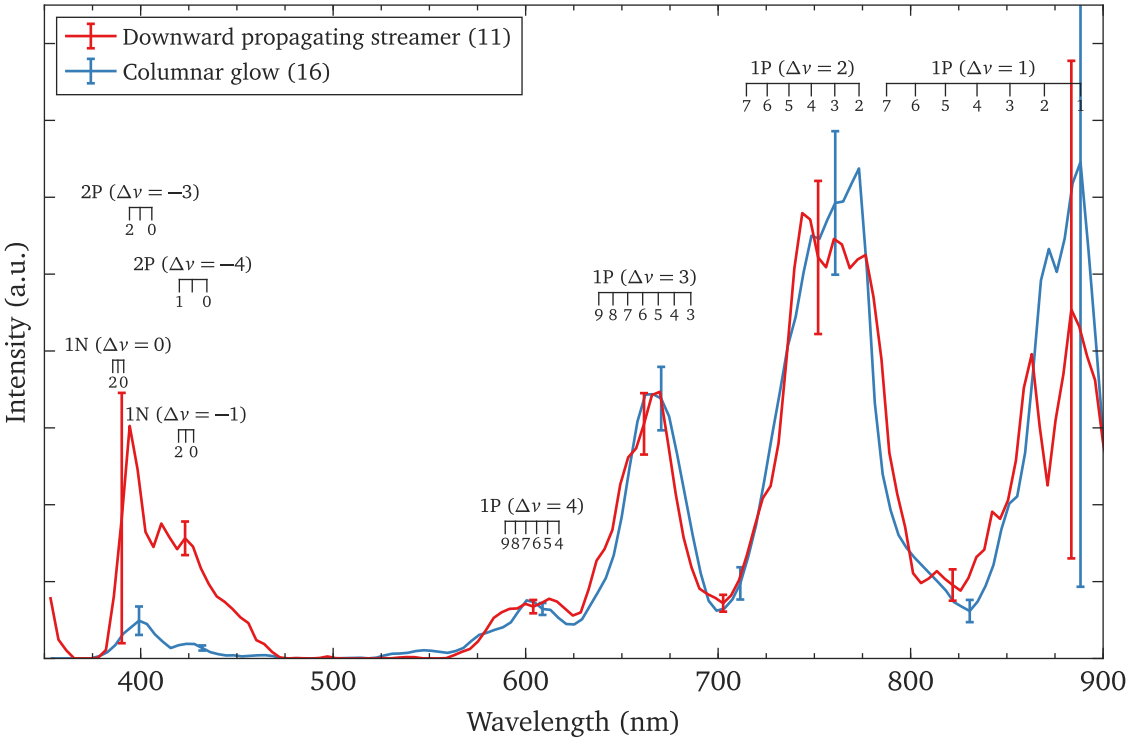

Figure 4.9. Spectra of a downward propagating streamers and a columnar glow in the sprite at 05:37:36 UT on 19 August 2009. The streamer spectrum was extracted from frame 11, and the glow spectrum was extracted from frame 16. They were corrected for the instrument response and normalized so that areas under the curves between 600 and 800 nm became the same.

positively identified.

A difference in the two spectra is clear: the streamer spectrum has a higher fraction of blue emission than the glow spectrum. It should be noted that the difference can not be attributed to the atmospheric attenuation associated with different viewing geometries, in which the streamer was observed at a lower elevation angle. The atmospheric transmittance for the streamer is indeed 10% lower at 400 nm than that for the glow, indicating that the streamer actually had an even higher fraction of blue emission. The excitation threshold energy for the Second Positive system is 11.0 eV, and that for the First Positive system is 7.4 eV. Therefore, the higher fraction of blue emission in the streamer indicates that the underlying electron energy in the streamer is higher than in the glow.

Spectra from one of the downward propagating streamers and the columnar glow in the sprites at 09:15:23 UT on 27 August are shown in Figure 4.10. They were extracted from the initial streamer in frame 7 and from the brightest segment of the glow in frame 11, both of which are shown with dotted lines in Figure 4.8. The spectra were corrected for the instrument response and were normalized by the areas under the curves between 600 and 800 nm, in the same manner as in Figure 4.9. The spectral resolution was determined to be roughly 26 nm for both spectra.

The features in the visible and near infrared are primarily composed of the N_2 First Positive system, and those in the near ultraviolet and blue are primarily composed of the N_2 Second Positive system. In the wavelength range 550 to 900 nm, both spectra have four features; they were identified as the $\Delta v = 1$ through 4 sequences of the First Positive system. In the wavelength range 400 to 450 nm, the streamer spectrum has two, yet broad, humps. The one at 400 nm was identified as the $\Delta v = -3$ sequence of the Second Positive system, the other at about 420 nm was the $\Delta v = -4$ sequence. The glow spectrum has a hump at 400 nm and very broad signal from 410 to 480 nm, which are different from the features observed in the streamer spectrum. These features could not be identified, though I suspect that these features were confused by scintillation noises from the intensifier. To quantify the identification, I have performed synthetic spectral fitting of the first and Second Positive systems to the observed spectra. But, again, it was not possible to obtain a good fit because of the coarse spectral resolution and the large uncertainties in the measurements.

A difference between the two spectra is not as clear as that in the spectra observed in the sprite at 05:37:36 UT on 19 August. Given that the near ultraviolet and blue signals from the glow is indeed scintillation noise, the streamer spectrum have a higher fraction of blue emission

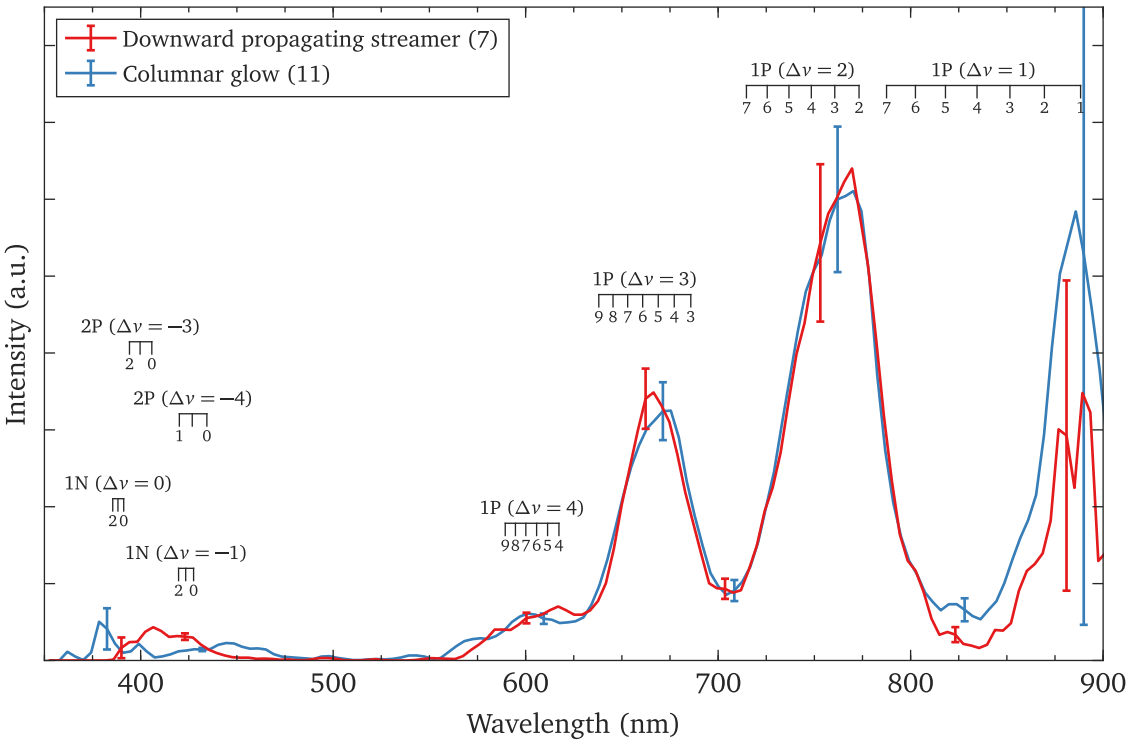

Figure 4.10. Spectra of a downward propagating streamers and a columnar glow in the sprite at 09:15:23 UT on 27 August 2009. The streamer spectrum was extracted from frame 7, and the glow spectrum was extracted from frame 12. They were normalized so that areas under the curves between 600 and 800 nm became the same.

than the glow spectrum by an appreciable magnitude. But the fraction of blue emission in the streamer spectrum is substantially lower than that in the streamer spectrum in the other event, indicating the electron energy in the streamer in this event is lower than that in the other event. It is likely that the driving electric field in the mesosphere in this event was weaker than in the other event.

4.5 Blue Emissions from Downward Propagating Streamers and Columnar Glows

To quantify the fraction of blue emission in downward propagating streamers and columnar glows, the intensity ratios of blue to red emissions were examined. They were determined from the observed spectra by taking the integrated signals from 400 to 500 nm and those from 600 to 800 nm. The blue and red wavelength ranges primarily include the N_2 Second Positive and N_2 First Positive emission, respectively; therefore, the relative values of the intensity ratios indicate those of the electron energies in the streamers and glows.

Figure 4.11 illustrates the intensity ratios obtained from different events, as functions of time elapsed from the onset of the events. The intensity ratios of columnar glows were obtained from the two sprites in the event at 05:37:36 UT on 19 August (Figure 4.5). The blue emissions from the two glows were not vertically uniform, and the intensity ratios were obtained from the segment that provided the highest values. In the first glow, the segment of the highest value gradually descended, and the intensity ratio increases with time. By contrast, in the second glow, the segment was nearly stationary, and the intensity ratio remains roughly at the same level.

The intensity ratios of downward propagating streamers were obtained from three events on 19 August and one event on 27 August. The intensity ratios of the streamers in the event at 05:37:36 UT on 19 August are consistently higher than those of the two glows in the same event, indicating that the electron energies in the streamers are higher than those in the glows. The intensity ratios of the streamers in different events on 19 August are also higher than those of the two glows. However, the intensity ratios of the streamers in the event at 09:15:23 UT on 27 August were considerably lower than those of the other streamers and even comparable to those of the two glows. This implies that the electron energies in sprites vary rather wildly from one event to another, though it seems that the electron energies in downward propagating streamers are higher than those in columnar glows for the same event.

The observed intensity ratios were examined with a plasma kinetic model, which was based on the kinetic model detailed in Section 3.5. The model simulates the populations of relevant

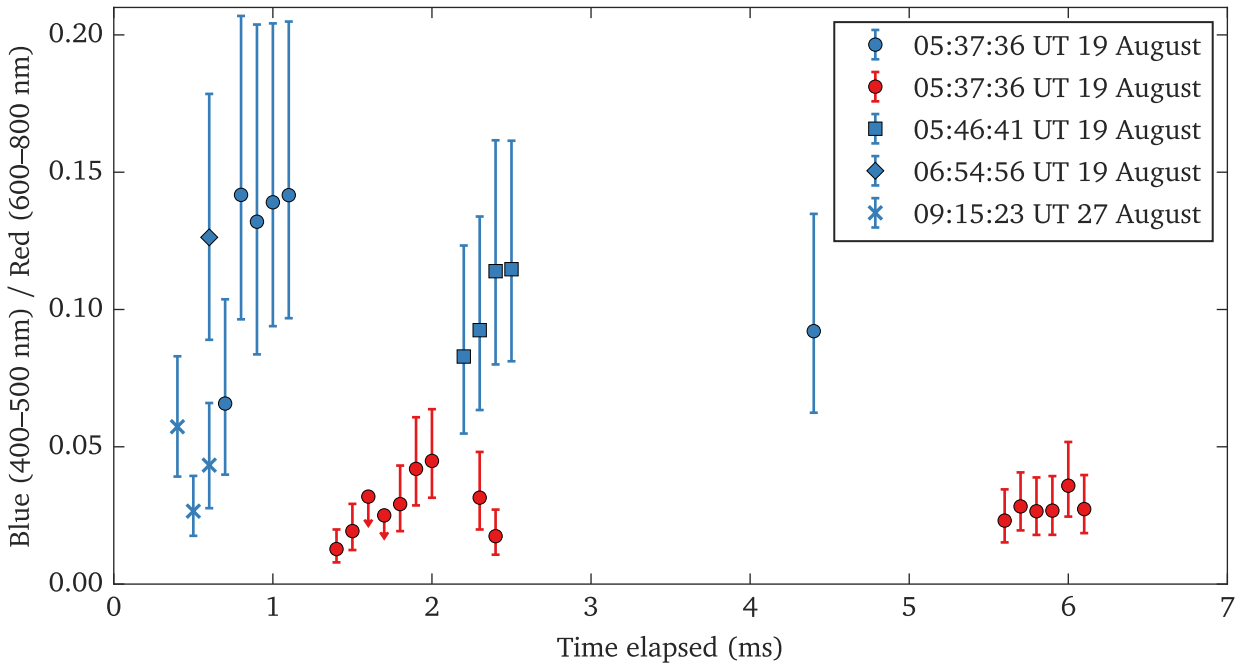

Figure 4.11. The intensity ratios of blue to red emissions in downward propagating streamers and columnar glows in different events, as as functions of time elapsed from the onset of the events. They were determined from the observed spectra by taking integrated signals from 400 to 500 nm and those from 600 to 800 nm. Blue and red colors are for the streamers and glows respectively, and different symbols are for different events as annotated. Error bars with a downward arrow indicate that the values are the upper limits due to saturated pixels in the spectra.

excited species under a steady state condition in a (zero-dimensional) volume of weakly-ionized air plasmas under the influence of a constant electric field. The relative populations of excited species were determined by a set of simplified kinetic reactions: electron impact excitation and ionization of neutral molecules, radiative cascading, and collisional quenching. The excited species incorporated in the model were $N_2(B\,^3\Pi_g, v)$, $N_2(C\,^3\Pi_u, v)$, and $N_2^+(B\,^2\Sigma_u^+, v)$, which are responsible for excitation of the N_2 First Positive, N_2 Second Positive, and N_2^+ First Negative emissions, respectively. The reactions incorporated in the model are summarized in Table 4.1.

The computation of the relative populations requires various rate coefficients and constants; they are summarized in the following. The rate coefficients for electron impact excitation and ionization were obtained by solving a Boltzmann equation for electrons in a weakly ionized air plasma using BOLSIG+ software [*Hagelaar and Pitchford*, 2005], with a set of electron collision cross sections compiled by A. V. Phelps (available at http://jila.colorado.edu/~avp/collision_data/). The rate coefficients for quenching of the excited species were based on those used in the previous sprite studies [*Adachi et al.*, 2006, 2008]. The rate coefficients for quenching of the excited species by N_2 were obtained from [*Vallance Jones*, 1974]. The rate coefficient for quenching of the $N_2(B\,^3\Pi_g, v = 1)$ by O_2 was obtained from [*Piper*, 1992] and was used for the entire $N_2(B\,^3\Pi_g)$ state. The Franck–Condon factors and the Einstein coefficients for spontaneous emission were obtained from [*Gilmore et al.*, 1992].

The relative populations of the excited species obtained from the model were used to compute the relative band intensities, and they were used to simulate the intensity ratios of blue to red emissions. To simulate the observations, the relative band intensities were attenuated by the atmospheric transmittance and were convolved with the instrument broadening. From the resultant band intensities, the intensity ratios were computed by taking integrated intensities of the N_2 Second Positive and N_2^+ Negative emissions from 400 to 500 nm and those of the N_2 First Positive emissions from 600 to 800 nm.

The modeled intensity ratios were given as functions of the reduced electric field E/N, and comparison with the observations allowed us to infer the electric fields in the downward propagating streamers and columnar glows. For the events on 19 August 2009, the inferred electric fields were 0.4 to $0.9E_k$ in the streamers and 0.3 to $0.6E_k$ in the glows, where E_k is the conventional breakdown threshold field. However, in the streamers, the assumption of uniformity of the plasma and electric field breaks down, and the electric field inferred from the intensity ratio of the N_2 Second Positive to the N_2 First Positive emissions has been reported to underestimate the true value by a factor of about 1.7 [*Celestin and Pasko*, 2010]. Applying this

Table 4.1. Reactions incorporated in the plasma emission model.

Reaction		Reference
Electron impact excitation		
$e^* + N_2(X\,^1\Sigma_g^+, v''=0) \rightarrow e + N_2(B\,^3\Pi_g, v')$		*Hagelaar and Pitchford* [2005][a]
$e^* + N_2(X\,^1\Sigma_g^+, v''=0) \rightarrow e + N_2(C\,^3\Pi_u, v')$		*Hagelaar and Pitchford* [2005][a]
Electron impact ionization		
$e^* + N_2(X\,^1\Sigma_g^+, v''=0) \rightarrow e + e + {N_2}^+(A^2\Pi_u, v')$		*Hagelaar and Pitchford* [2005][a]
Radiative cascading		
$N_2(B\,^3\Pi_g, v') \rightarrow N_2(A^3\Sigma_g^+, v'') + h\nu$	N_2 First Positive system	*Gilmore et al.* [1992]
$N_2(C\,^3\Pi_u, v') \rightarrow N_2(B\,^3\Pi_g, v'') + h\nu$	N_2 Second Positive system	*Gilmore et al.* [1992]
${N_2}^+(B\,^2\Pi_u, v') \rightarrow {N_2}^+(X\,^2\Sigma_g^+, v'') + h\nu$	${N_2}^+$ First Negative system	*Gilmore et al.* [1992]
Collisional quenching		
$N_2(B\,^3\Pi_g) + N_2 \rightarrow N_2 + N_2$		*Vallance Jones* [1974]
$N_2(B\,^3\Pi_g) + O_2 \rightarrow N_2 + O_2$		*Piper* [1992][b]
$N_2(C\,^3\Pi_u) + N_2 \rightarrow N_2 + N_2$		*Vallance Jones* [1974]
$N_2(C\,^3\Pi_u) + O_2 \rightarrow N_2 + O_2$		*Vallance Jones* [1974]
${N_2}^+(B\,^2\Sigma_u^+) + N_2 \rightarrow {N_2}^+ + N_2$		*Vallance Jones* [1974]
${N_2}^+(B\,^2\Sigma_u^+) + O_2 \rightarrow {N_2}^+ + O_2$		*Vallance Jones* [1974]

[a] The rate coefficients were obtained by solving a Boltzmann equation for electrons in a weakly ionized air plasma using BOLSIG+ software [*Hagelaar and Pitchford*, 2005], with a set of electron collision cross sections compiled by A. V. Phelps (available at http://jila.colorado.edu/~avp/collision_data/).

[b] The rate coefficient for the $v = 1$ level was used for the entire $N_2(B\,^3\Pi_g)$ state.

correction factor increases the electric field to 0.7 to 1.5E_k. Nevertheless, the model indicated that the electric fields in the streamers are higher than that in the glows.

Adachi et al. [2006] reported the local electric fields in the streamers estimated from the intensity ratios of the Second Positive to the First Positive emissions. The reported values after applying the correction factor are 1.7 to 3.4E_k, which are significantly larger than the value reported above. It may be attributed to the fact that most of the events analyzed by *Adachi et al.* [2006] were extremely bright events (T. Adachi, private communication, 2010).

4.6 Blue Emissions from Upward Propagating Streamers

Blue emission from an upward propagating streamer was observed in the sprite at 05:37:36 UT. Unfortunately, the spectra of the streamer was not fully isolated: it partially overlapped the spectrum of another nearby streamer. Nevertheless, the data provide an insight into the electron energy of the upward propagating streamer for comparison with those of the downward propagating streamers and columnar glows in the same event.

The spectra from the upward propagating streamer are shown in Figure 4.12. They were extracted from a brighter upward propagating streamer to the left in the field of view in frame 14 and 15, which are shown with dotted lines in Figure 4.6. In frame 14, the spectrum of the streamer partially overlapped that of an upward propagating streamer to the right, which was horizontally separated by 15 pixels equivalent to 60 nm in wavelength. This indicates that the spectral features of the streamer to the right from 400 to 450 nm and those from 560 to 620 nm are at 460 to 510 nm and at 620 to 680 nm in the shown wavelength, respectively. Therefore, although the two spectra partially overlapped, the spectral features of the streamer to the left from 400 to 450 nm and those from 560 to 620 nm were well-defined, allowing a comparison of the fractional blue emissions. This is also true for the spectrum of the same upward propagating streamer in frame 15 because the two streamers are separated by 20 pixels, equivalent to 80 nm.

The upward propagating streamer spectra were compared with those of the downward propagating streamer in frame 11 and the columnar glow in frame 16. These spectra were normalized by the peak intensity between 560 and 620 nm, but are not corrected for the instrument response to avoid introducing errors. The upward propagating streamer spectra show significant deviation above 680 nm, but this is caused by the overlapping spectra.

The fraction of blue emissions from the upward propagating streamer was slightly higher than those from the columnar glow, but was substantially lower than that of the downward propagating streamer. It should be noted that the difference is not an artifact introduced by

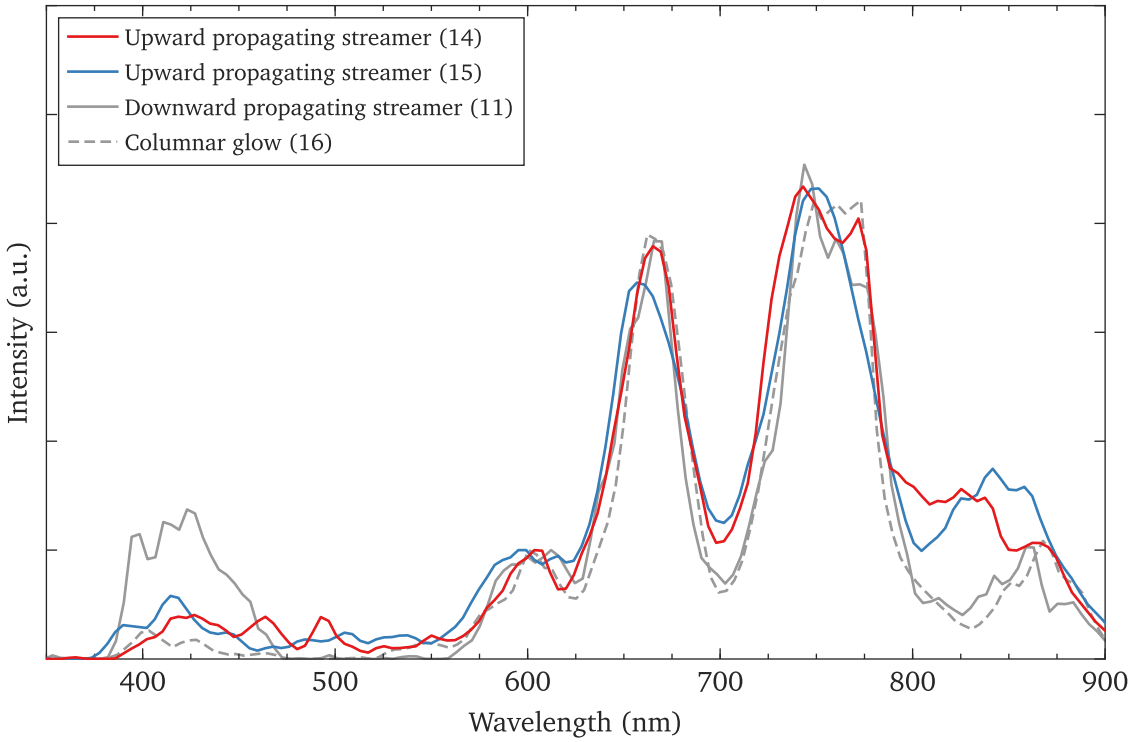

Figure 4.12. Spectra of an upward propagating streamer observed in the sprite at 05:37:36 UT on 19 August. They were extracted from frame 14 and 15 (Figure 4.6). The downward propagating streamer spectrum in frame 11 and the columnar glow spectrum in frame 16 are also shown for comparison. The spectra were normalized by the peak intensity between 560 and 620 nm, but not corrected for the instrument response.

the normalization employed above. I have also normalized the spectra by the areas under the curves between 560 and 600 nm and by the peak intensities between 620 and 700 nm, but I saw the same result regardless of the normalization methods. The difference in the fractional blue emissions suggests that the electron energy in the upward propagating streamer is slightly higher than that in the glow, but lower than that in the downward propagating streamer.

Chapter 5

Summary

Ionization in sprites has been evidenced by observations of the N_2^+ First Negative ($B\,^2\Sigma_u^+ \rightarrow X\,^2\Sigma_g^+$) emission, but further evidence of the ionization may be provided by the N_2^+ Meinel ($A^2\Pi_u^+ \rightarrow X\,^2\Sigma_g^+$) emission. The Meinel emission in the visible and near infrared is more accessible from the ground-based platforms compared with the First Negative emission in the near ultraviolet and blue; therefore, the Meinel emission would be a valuable probe of ionization processes in sprites. The presence of the Meinel emission, however, is somewhat controversial because it is expected to be strongly quenched in the mesosphere and below. Previous spectral observations in the visible and near infrared have been examined for the Meinel bands, but the nature of the Meinel emission in sprites still remains an open issue [*Mende et al.*, 1995; *Hampton et al.*, 1996; *Green et al.*, 1996; *Morrill et al.*, 1998; *Bucsela et al.*, 2003].

To investigate the presence of the Meinel emission along the vertical extent of sprites, we made spectral observations in the summer of 2005. The ground-based observations were made with an intensified CCD spectrograph with a vertically oriented slit, which allowed us to obtain vertically resolved spectra and to examine emissions from different structures along the vertical extent of sprites. The spectrograph provided spectral coverage in the visible and near infrared from 640 to 820 nm with a resolution of about 3 nm. Spectra were recorded at 300 fps.

The observed spectra were mainly composed of the N_2 First Positive ($B\,^3\Pi_g \rightarrow A\,^3\Sigma_u^+$) system, and no or little indication of the Meinel bands was found in any structures along the vertical extent of sprites. To verify the apparent lack of the Meinel bands, the observed spectra were fitted with synthetic spectra of the First Positive system to differentiate the signals from the Meinel bands. The signals from the Meinel bands were determined to be indeed below or comparable to the noise level. Based on the noise level and the residuals of the fit, the population of $N_2^+(A^2\Pi_u^+, v=2)$ was inferred to be at most 3 to 7 % of $N_2(B\,^3\Pi_g, v=2)$.

In addition to the Meinel bands, the spectral observations in 2005 provided an opportunity to investigate the vibrational distribution of the $N_2(B\,^3\Pi_g)$ state, the upper state of the First Positive system. Previous spectral observations have suggested that the vibrational distribution varies along the vertical extent of sprites, which implies that the ranking of the processes that lead to excitation of the First Positive emission varies [*Heavner*, 2000; *Bucsela et al.*, 2003]. But the previous data were very limited, and additional data were needed to characterize the variation along the vertical extent of sprites.

The observed spectra confirmed the previously reported variation of the vibrational distribu-

tion and furthermore indicated that the distribution simply varies with altitude. The observed vibrational distributions showed that the relative populations of the $v' = 3$ level and higher decrease at lower altitude, which is consistent with the previous reports [*Heavner*, 2000; *Bucsela et al.*, 2003], and the observed distribution in the tendrils at 49 to 55 km was in good agreement with the previously reported distribution in the tendrils at 53 km altitude [*Bucsela et al.*, 2003]. Moreover, the intensity ratios of the (4–2) to (2–0) First Positive bands decreased more or less linearly with decreasing altitude, indicating that the observed distribution simply varies with altitude regardless of different structures along the vertical extend of sprites.

The altitude variation indicates that the ranking of the processes producing $N_2(B\,^3\Pi_g, v)$ varies with altitude, and collisional processes, such as quenching and other types of energy transfer, are responsible for the observed vibrational distributions. From the results of recent modeling studies [*Gordillo-Vazquez*, 2010; *Luque and Gordillo-Vázquez*, 2011], I speculate that the underlying mechanism of the altitude variation of the vibrational distribution is twofold. While the intersystem collisional transfer is responsible for the variation above the quenching altitude, the quenching of $N_2(B\,^3\Pi_g, v)$ is responsible for the variation below the quenching altitude. Both processes involve a neutral molecules as a colliding particle, and therefore becomes more effective at lower altitudes within the respective regions.

Recent high-speed imaging observations have revealed that sprites develop in forms of sprite streamers and columnar glows [*Stenbaek-Nielsen and McHarg*, 2008, references therein]. Sprite streamers are narrow filamentary channels. They rapidly propagate both downward and upward, frequently split into narrower channels, and quickly extend over the altitude range 40 to 90 km within a few ms. Columnar glows are, as the name suggests, more or less stationary emission of a columnar shape. They forms in the wake of downward propagating streamers and normally persist for a few to 10 ms.

The ranking of the underlying electron energies in sprite streamers and columnar glows has been suggested by previous observational studies. Photometric measurements provided temporally resolved time histories of different band emissions, but with no spatial resolution [*Suszcynsky et al.*, 1998; *Armstrong et al.*, 1998, 2000]. Multi-color imaging measurements provided spatially resolved distributions of two different band emissions, but with poor temporal resolution [*Morrill et al.*, 2002]. From the results of these measurements together, it was inferred that sprite streamers are energetic initiation processes that primarily cause ionization in sprites, and columnar glows are less energetic secondary processes that mainly produce the relatively long-lived neutral emissions. However, there has been no direct measurement that confirms the

underlying electron energies.

To investigate the underlying electron energies, we made spectral observations with a slitless spectrograph in the summer of 2009. The spectrograph was composed of a transmission grating and a high-speed intensified CMOS camera, which had been previously used in high-speed imaging observations [*McHarg et al.*, 2007; *Stenbaek-Nielsen et al.*, 2007], to temporally resolve the streamers and glows. It provided spectral coverage from the near ultraviolet to near infrared 400 to 900 nm, and spectra were recorded at 10 000 fps. To minimize atmospheric attenuation and to observe blue emissions from sprites, the observations were made from an aircraft.

The observed spectra in the visible and near infrared were primarily composed of the N_2 First Positive system, and those in the near ultraviolet and blue were primarily composed of the N_2 Second Positive system. The N_2^+ First Negative system was not positively identified in the data because of the coarse spectral resolution and the large uncertainties particularly below 400 nm, due primarily to a steep cut-off in the aircraft window transmission.

Nevertheless, the fraction of blue emissions clearly indicated that the electron energies in downward propagating streamers are higher than those in columnar glows. In the event at 05:37:26 UT on 19 August, the fractional blue emissions in the streamers were consistently higher than those of the glows. From the fractional blue emissions, the local electric fields were inferred: the electric field in the streamers was 0.7 to 1.5 E_k, and that in the glows was 0.3 to 0.6 E_k, where E_k is the threshold field for conventional breakdown in air. In the other two events on 19 August, the fractional blue emissions in the streamers were consistently higher than those in the glows in the event on 05:37:26 UT on 19 August.

Moreover, the data suggest that the ranking of the electron energy in upward propagating streamers compared to those in downward propagating streamers and columnar glows. In the event at 05:36:36 UT, the fractional blue emissions in the upward propagating streamers was substantially lower than those in the downward propagating streamers and slightly higher than or comparable to those of the glows. This indicates that the electron energy in the upward propagating streamers are substantially lower than those in the downward propagating streamers but slightly higher or comparable to those in the glows.

The data also suggest that the electron energies in sprites vary greatly from one event to another. In the even at 09:15:23 UT on 27 August, the fractional blue emission in the streamers was substantially lower than those the other streamers and even comparable to those of the glows in the event at 05:37:26 UT on 19 August. This implies that the electron energies in sprites vary rather greatly from one event to another.

The observations with the slitless spectrograph unambiguously confirmed the more energetic nature of sprite streamers than columnar glows, which had not been possible in previous observations. However, no feature of the N_2^+ First Negative system was positively identified in the observed spectral features because of the steep cut-off in the aircraft window transmittance below 400 nm. Airborne observations with a slitless spectrograph with a quartz window may allow us to observe the N_2^+ First Negative emissions and thus to study ionization processes in individual streamers and columnar glows.

Bibliography

Abe, S. (2000), Spectroscopic study of meteors and persistent trains, Ph.D. thesis, The Graduate University for Advanced Studies.

Adachi, T., H. Fukunishi, Y. Takahashi, Y. Hiraki, R.-R. Hsu, H.-T. Su, A. B. Chen, S. B. Mende, H. U. Frey, and L. C. Lee (2006), Electric field transition between the diffuse and streamer regions of sprites estimated from ISUAL/array photometer measurements, *Geophys. Res. Lett.*, *33*, L17803, doi:10.1029/2006GL026495.

Adachi, T., Y. Hiraki, K. Yamamoto, Y. Takahashi, H. Fukunishi, R.-R. Hsu, H.-T. Su, A. B. Chen, S. B. Mende, H. U. Frey, and L. C. Lee (2008), Electric fields and electron energies in sprites and temporal evolutions of lightning charge moment, *J. Phys. D: Appl. Phys.*, *41*(23), 234,010, doi:10.1088/0022-3727/41/23/234010.

Allen, N. L., and A. Ghaffar (1995), The conditions required for the propagation of a cathode-directed positive streamer in air, *J. Phys. D: Appl. Phys.*, *28*, 331–337, doi:10.1088/0022-3727/28/2/016.

Armstrong, R. A., J. A. Shorter, M. J. Taylor, D. M. Suszcynsky, W. A. Lyons, and L. S. Jeong (1998), Photometric measurements in the SPRITES '95 & '96 campaigns of nitrogen second positive (399.8 nm) and first negative (427.8 nm) emissions, *J. Atmos. Sol. Terr. Phys.*, *60*(7–9), 787–799, doi:10.1016/S1364-6826(98)00026-1.

Armstrong, R. A., D. M. Suszcynsky, W. A. Lyons, and T. E. Nelson (2000), Multi-color photometric measurements of ionization and energies in sprites, *Geophys. Res. Lett.*, *27*(5), 653–656, doi:10.1029/1999GL003672.

Barrington-Leigh, C. P., and U. S. Inan (1999), Elves triggered by positive and negative lightning discharges, *Geophys. Res. Lett.*, *26*, 683–686, doi:10.1029/1999GL900059.

Bazelyan, E. M., and Y. P. Raizer (1998), *Spark Discharge*, CRC Press.

Boccippio, D. J., E. R. Williams, S. J. Heckman, W. A. Lyons, I. T. Baker, and R. Boldi (1995), Sprites, ELF transients, and positive ground strokes, *Science*, *269*, 1088–1091, doi:10.1126/science.269.5227.1088.

Bór, J. (2013), Optically perceptible characteristics of sprites observed in Central Europe in 2007-2009, *J. Atmos. Sol.-Terr. Phys.*, *92*, 151–177, doi:10.1016/j.jastp.2012.10.008.

Brown, J. M. (1998), *Molecular Spectroscopy*, Oxford University Press.

Brown, J. M., and A. Carrington (2003), *Rotational Spectroscopy of Diatomic Molecules*, Cambridge University Press.

Bucsela, E. J., J. S. Morrill, M. J. Heavner, C. L. Siefring, S. L. Berg, D. L. Hampton, D. R. Moudry, E. M. Wescott, and D. D. Sentman (2003), $N_2\,(B\,^3\Pi_g)$ and $N_2^+\,(A\,^2\Pi_u)$ vibrational distributions observed in sprites, *J. Atmos. Sol. Terr. Phys.*, *65*(5), 583–590, doi:10.1016/S1364-6826(02)00316-4.

Cartwright, D. C., S. Trajmar, A. Chutjian, and W. Williams (1977), Electron impact excitation of the electronic states of N_2. II. Integral cross sections at incident energies from 10 to 50 eV, *Phys. Rev. A*, *16*, 1041–1051, doi:10.1103/PhysRevA.16.1041.

Celestin, S., and V. P. Pasko (2010), Effects of spatial non-uniformity of streamer discharges on spectroscopic diagnostics of peak electric fields in transient luminous events, *Geophys. Res. Lett.*, *37*, L07804, doi:10.1029/2010GL042675.

Ciddor, P. E. (1996), Refractive index of air: new equations for the visible and near infrared, *Appl. Optics*, *35*, 1566, doi:10.1364/AO.35.001566.

Cornette, W. M., P. Acharya, D. Robertson, and G. P. Anderson (1995), Moderate spectral atmospheric radiance and transmittance code (MOSART), *Technical Report PL-TR-94-2244*, Philips Laboratory, Directorate of Geophysics, Hanscom AFB, MA.

Cummer, S. A., and W. A. Lyons (2004), Lightning charge moment changes in U.S. High Plains thunderstorms, *Geophys. Res. Lett.*, *31*, L05114, doi:10.1029/2003GL019043.

Cummer, S. A., and W. A. Lyons (2005), Implications of lightning charge moment changes for sprite initiation, *J. Geophys. Res.*, *110*, A04304, doi:10.1029/2004JA010812.

Cummer, S. A., N. Jaugey, J. Li, W. A. Lyons, T. E. Nelson, and E. A. Gerken (2006), Submillisecond imaging of sprite development and structure, *Geophys. Res. Lett.*, *33*, L04104, doi:10.1029/2005GL024969.

Cummins, K. L., M. J. Murphy, E. A. Bardo, W. L. Hiscox, R. B. Pyle, and A. E. Pifer (1998), A Combined TOA/MDF Technology Upgrade of the U.S. National Lightning Detection Network, *J. Geophys. Res.*, *103*, 9035–9044, doi:10.1029/98JD00153.

Davies, D. K. (1983), Measurements of swarm parameters in dry air, *Theoretical Notes 346*, Westinghouse R&D Center, Pittsburgh, PA.

Dilecce, G., P. F. Ambrico, and S. De Benedictis (2006), OODR-LIF direct measurement of $N_2\,(C\,^3\Pi_u, v = 0\text{–}4)$ electronic quenching and vibrational relaxation rate coefficients by N_2 collision, *Chem. Phys. Lett.*, *431*, 241–246, doi:10.1016/j.cplett.2006.09.094.

Dilecce, G., P. F. Ambrico, and S. De Benedictis (2010), On the collision quenching of $N_2^+\,(B\,^2\Sigma_u^+, v = 0)$ by N_2 and O_2 and its influence on the measurement of E/N by intensity ratio of nitrogen spectral bands, *J. Phys. D: Appl. Phys.*, *43*(19), 195,201, doi:10.1088/0022-3727/43/19/195201.

Dutton, J. (1975), A survey of electron swarm data, *J. Phys. Chem. Ref. Data*, *4*, 577–856, doi:10.1063/1.555525.

Ebert, U., C. Montijn, T. M. P. Briels, W. Hundsdorfer, B. Meulenbroek, A. Rocco, and E. M. van Veldhuizen (2006), The multiscale nature of streamers, *Plasma Sources Sci. Technol.*, *15*, 118, doi:10.1088/0963-0252/15/2/S14.

Ebert, U., S. Nijdam, C. Li, A. Luque, T. Briels, and E. van Veldhuizen (2010), Review of recent results on streamer discharges and discussion of their relevance for sprites and lightning, *J. Geophys. Res.*, *115*(A14), A00E43, doi:10.1029/2009JA014867.

Franz, R. C., R. J. Nemzek, and J. R. Winckler (1990), Television image of a large upward electrical discharge above a thunderstorm system, *Science*, *249*, 48–51, doi:10.1126/science.249.4964.48.

Gerken, E. A., U. S. Inan, and C. P. Barrington-Leigh (2000), Telescopic imaging of sprites, *Geophys. Res. Lett.*, *27*(17), 2637–2640, doi:10.1029/2000GL000035.

Gilmore, F. R., R. R. Laher, and P. J. Espy (1992), Franck–Condon factors, r-centroids, electronic transition moments, and einstein coefficients for many nitrogen and oxygen band systems, *J. Phys. Chem. Ref. Data*, *21*(5), 1005–1107, doi:10.1063/1.555910.

Goodman, S. J., and D. R. MacGorman (1986), Cloud-to-Ground Lightning Activity in Mesoscale Convective Complexes, *Mon. Wea. Rev.*, *114*, 2320, doi:10.1175/1520-0493(1986)114<2320:CTGLAI>2.0.CO;2.

Gordillo-Vazquez, F. J. (2010), Vibrational kinetics of air plasmas induced by sprites, *J. Geophys. Res.*, *115*, A00E25, doi:10.1029/2009JA014688.

Green, B. D., M. E. Fraser, W. T. Rawlins, L. Jeong, W. A. M. Blumberg, S. B. Mende, G. R. Swenson, D. L. Hampton, E. M. Wescott, and D. D. Sentman (1996), Molecular excitation in sprites, *Geophys. Res. Lett.*, *23*(16), 2161–2164, doi:10.1029/96GL02071.

Hagelaar, G. J. M., and L. C. Pitchford (2005), Solving the Boltzmann equation to obtain electron transport coefficients and rate coefficients for fluid models, *Plasma Sources Sci. Technol.*, *14*, 722–733, doi:10.1088/0963-0252/14/4/011.

Hale, L. C. (1994), Coupling of ELF/ULF energy from lightning and MeV particles to the middle atmosphere, inosphere, and global circuit, *J. Geophys. Res.*, *99*, 21,089, doi:10.1029/94JD00357.

Hallinan, T. J., H. C. Stenbaek-Nielsen, and C. S. Deehr (1985), Enhanced aurora, *J. Geophys. Res.*, *90*, 8461–8475, doi:10.1029/JA090iA09p08461.

Hampton, D. L., M. J. Heavner, E. M. Wescott, and D. D. Sentman (1996), Optical spectral characteristics of sprites, *Geophys. Res. Lett.*, *23*(1), 89–92, doi:10.1029/95GL03587.

Heavner, M. J. (2000), Optical spectroscopic observations of sprites, blue jets, and elves: Inferred microphysical processes and their macrophysical implications, Ph.D. thesis, University of Alaska Fairbanks.

Heavner, M. J., J. S. Morrill, C. Siefring, D. D. Sentman, D. R. Moudry, E. M. Wescott, and E. J. Bucsela (2010), Near-ultraviolet and blue spectral observations of sprites in the 320-460 nm region: N_2 (2PG) emissions, *Geophys. Res. Lett.*, *115*, A00E44, doi:10.1029/2009JA014858.

Hedin, A. E. (1991), Extension of the MSIS thermosphere model into the middle and lower atmosphere, *J. Geophys. Res.*, *96*(A2), 1159–1172, doi:10.1029/90JA02125.

Herzberg, G. (1950), *Molecular Spectra and Molecular Structure I. Spectra of Diatomic Molecules*, second ed., Van Nostrand Reinhold Company.

Kanmae, T., H. C. Stenbaek-Nielsen, and M. G. McHarg (2007), Altitude resolved sprite spectra with 3 ms temporal resolution, *Geophys. Res. Lett.*, *34*(7), L07810, doi:10.1029/2006GL028608.

Kanmae, T., H. C. Stenbaek-Nielsen, M. G. McHarg, and R. K. Haaland (2010), Observation of sprite streamer head's spectra at 10,000 fps, *J. Geophys. Res.*, *115*, A00E48, doi:10.1029/2009JA014546.

Katayama, D. H. (1984), Collision induced electronic energy transfer between the $A^2\Pi_u$ ($v = 4$) and $X\,^2\Sigma_g^+$ ($v = 8$) rotational manifolds of N_2^+, *J. Chem. Phys.*, *81*, 3495–3499, doi:10.1063/1.448076.

Katayama, D. H., T. A. Miller, and V. E. Bondybey (1980), Collisional deactivation of selectivity excited N_2^+, *J. Chem. Phys.*, *72*, 5469–5475, doi:10.1063/1.439016.

Klynning, L., and P. Pagès (1982), The band spectrum of N_2^+, *Phys. Scr.*, *25*(4), 543–560, doi:10.1088/0031-8949/25/4/009.

Kovacs, I. (1969), *Rotational Structure in the Spectra of Diatomic Molecules*, Elsevier, New York.

Kuo, C.-L., R. R. Hsu, A. B. Chen, H. T. Su, L. C. Lee, S. B. Mende, H. U. Frey, H. Fukunishi, and Y. Takahashi (2005), Electric fields and electron energies inferred from the ISUAL recorded sprites, *Geophys. Res. Lett.*, *32*, L19103, doi:10.1029/2005GL023389.

Kuo, C. L., A. B. Chen, J. K. Chou, L. Y. Tsai, R. R. Hsu, H. T. Su, H. U. Frey, S. B. Mende, Y. Takahashi, and L. C. Lee (2008), Radiative emission and energy deposition in transient luminous events, *J. Phys. D: Appl. Phys.*, *41*(23), 234,014, doi:10.1088/0022-3727/41/23/234014.

Kurucz, R. L. (1992), Model Atmospheres for Population Synthesis, in *The Stellar Populations of Galaxies*, *IAU Symposium*, vol. 149, edited by B. Barbuy and A. Renzini, p. 225.

Laher, R. R., and F. R. Gilmore (1991), Improved fits for the vibrational and rotational constants of many states of nitrogen and oxygen, *J. Phys. Chem. Ref. Data*, *20*, 685–712, doi:10.1063/1.555910.

Li, J., and S. A. Cummer (2009), Measurement of sprite streamer acceleration and deceleration, *Geophys. Res. Lett.*, *36*, L10812, doi:10.1029/2009GL037581.

Liu, N., V. P. Pasko, D. H. Burkhardt, H. U. Frey, S. B. Mende, H.-T. Su, A. B. Chen, R.-R. Hsu, L.-C. Lee, H. Fukunishi, and Y. Takahashi (2006), Comparison of results from sprite streamer modeling with spectrophotometric measurements by ISUAL instrument on FORMOSAT-2 satellite, *Geophys. Res. Lett.*, *33*, L01101, doi:10.1029/2005GL024243.

Lofthus, A., and P. H. Krupenie (1977), The spectrum of molecular nitrogen, *J. Phys. Chem. Ref. Data*, *6*, 113–307, doi:10.1063/1.555546.

Luque, A., and F. J. Gordillo-Vázquez (2011), Modeling and analysis of $N_2(B\,^3\Pi_g)$ and $N_2(C\,^3\Pi_u)$ vibrational distributions in sprites, *Journal of Geophysical Research (Space Physics)*, *116*, A02306, doi:10.1029/2010JA015952.

Lyons, W. A. (1996), Sprite observations above the U.S. High Plains in relation to their parent thunderstorm systems, *J. Geophys. Res.*, *101*, 29,641–29,652, doi:10.1029/96JD01866.

Lyons, W. A., R. A. Armstrong, E. A. Bering, III, and E. R. Williams (2000), The hundred year hunt for the sprite, *EOS Trans.*, *81*, 373–377, doi:10.1029/00EO00278.

Marinelli, W. J., W. J. Kessler, B. D. Green, and W. A. M. Blumberg (1989), Quenching of $N_2(a\,^1\Pi_g, v' = 0)$ by N_2, O_2, CO, CO_2, CH_4, H_2, and Ar, *J. Chem. Phys.*, *90*, 2167–2173, doi:10.1063/1.456012.

McHarg, M. G., H. C. Stenbaek-Nielsen, and T. Kammae (2007), Observations of streamer formation in sprites, *Geophys. Res. Lett.*, *34*, L06804, doi:10.1029/2006GL027854.

McHarg, M. G., H. C. Stenbaek-Nielsen, T. Kanmae, and R. K. Haaland (2010), Streamer tip splitting in sprites, *J. Geophys. Res.*, *115*(A14), A00E53, doi:10.1029/2009JA014850.

Mende, S. B., R. L. Rairden, G. R. Swenson, and W. A. Lyons (1995), Sprite spectra; N_2 1 PG band identification, *Geophys. Res. Lett.*, *22*(19), 2633–2636, doi:10.1029/95GL02827.

Morrill, J., E. Bucsela, C. Siefring, M. Heavner, S. Berg, D. Moudry, S. Slinker, R. Fernsler, E. Wescott, D. Sentman, and D. Osborne (2002), Electron energy and electric field estimates in sprites derived from ionized and neutral N_2 emissions, *Geophys. Res. Lett.*, *29*(10), 1462, doi:10.1029/2001GL014018.

Morrill, J. S., and W. M. Benesch (1994), Role of N_2 $(A'\,^5\Sigma_g^+)$ in the enhancement of N_2 $B\,^3\Pi_g(v = 10)$ populations in the afterglow, *J. Chem. Phys.*, *101*, 6529–6537, doi:10.1063/1.468347.

Morrill, J. S., E. J. Bucsela, V. P. Pasko, S. L. Berg, M. J. Heavner, D. R. Moudry, W. M. Benesch, E. M. Wescott, and D. D. Sentman (1998), Time resolved N_2 triplet state vibrational populations and emissions associated with red sprites, *J. Atmos. Sol. Terr. Phys.*, *60*(7–9), 811–829, doi:10.1016/S1364-6826(98)00031-5.

Moudry, D., H. Stenbaek-Nielsen, D. Sentman, and E. Wescott (2003), Imaging of elves, halos and sprite initiation at 1ms time resolution, *J. Atmos. Sol.-Terr. Phys.*, *65*, 509–518, doi:10.1016/S1364-6826(02)00323-1.

Moudry, D. R., H. C. Stenbaek-Nielsen, D. D. Sentman, and E. M. Wescott (2002), Velocities of sprite tendrils, *Geophys. Res. Lett.*, *29*(20), 1992, doi:10.1029/2002GL015682.

Naghizadeh-Kashani, Y., Y. Cressault, and G. A. (2010), Net emission coefficient of air thermal plasmas, *J. Phys. D: Appl. Phys.*, *43*(14), 145,204, doi:10.1088/0022-3727/43/14/145204.

Nijdam, S. (2011), Experimental investigations on the Physics of Streamers, Ph.D. thesis, Technische Universiteit Eindhoven.

Nijdam, S., G. Wormeester, E. M. van Veldhuizen, and U. Ebert (2011), Probing background ionization: positive streamers with varying pulse repetition rate and with a radioactive admixture, *J. Phys. D: Appl. Phys.*, *44*, 5201, doi:10.1088/0022-3727/44/45/455201.

Nudnova, M. M., and A. Y. Starikovskii (2008), Streamer head structure: role of ionization and photoionization, *J. Phys. D: Appl. Phys.*, *41*(23), 234,003, doi:10.1088/0022-3727/41/23/234003.

Pasko, V. P. (2003), Atmospheric physics: Electric jets, *Nature*, *423*, 927–929, doi:10.1038/423927a.

Pasko, V. P. (2007), TOPICAL REVIEW: Red sprite discharges in the atmosphere at high altitude: the molecular physics and the similarity with laboratory discharges, *Plasma Sources Sci. Technol.*, *16*, S13, doi:10.1088/0963-0252/16/1/S02.

Pasko, V. P., U. S. Inan, Y. N. Taranenko, and T. F. Bell (1995), Heating, ionization and upward discharges in the mesosphere, due to intense quasi-electrostatic thundercloud fields, *Geophys. Res. Lett.*, *22*, 365–368, doi:10.1029/95GL00008.

Pasko, V. P., U. S. Inan, and T. F. Bell (1998), Spatial structure of sprites, *Geophys. Res. Lett.*, *25*(12), 2123–2126, doi:10.1029/98GL01242.

Pereira, L., A. Morozov, M. M. Fraga, T. Heindl, R. Krücken, J. Wieser, and A. Ulrich (2010), Temperature dependence of the quenching of $N_2(C\,^3\Pi_u)$ by $N_2(X)$ and $O_2(X)$, *Eur. Phys. J. D*, *56*, 325–334, doi:10.1140/epjd/e2009-00313-4.

Piper, L. G. (1988), State-to-state $N_2(A\,^3\Sigma_u^+)$ energy pooling reactions. II. The formation and quenching of $N_2(B\,^3\Pi_g, v' = 1\text{–}12)$, *J. Chem. Phys.*, *88*, 6911–6921, doi:10.1063/1.454388.

Piper, L. G. (1992), Energy transfer studies on $N_2(X\,^1\Sigma_g^+, v)$ and $N_2(B\,^3\Pi_g)$, *J. Chem. Phys.*, *97*(1), 270–275, doi:10.1063/1.463625.

Piper, L. G., B. D. Green, W. A. M. Blumberg, and S. J. Wolnik (1985), N_2^+ Meinel band quenching, *J. Chem. Phys.*, *82*, 3139–3145, doi:10.1063/1.448211.

Rakov, V. A., and M. A. Uman (2003), *Lightning: Physics and Effects*, Cambridge University Press.

Roux, F., and F. Michaud (1990), Investigation of the rovibrational levels of the $B\,^3\Pi_g$ state of $^{14}N_2$ molecule above the dissociation limit $N(^4S) + N(^4S)$ by Fourier transform spectrometry, *Can. J. Phys.*, *68*, 1257–1261, doi:10.1139/p90-181.

Roux, F., F. Michaud, and M. Vervloet (1993), High-resolution Fourier spectrometry of $^{14}N_2$ violet emission spectrum: extensive analysis of the $C\,^3\Pi_u \rightarrow B\,^3\Pi_g$ system, *J. Mol. Spectrosc.*, *158*, 270–277, doi:10.1006/jmsp.1993.1071.

Schadee, A. (1978), Unique definitions for the band strength and the electronic-vibrational dipole moment of diatomic molecular radiative transitions., *J. Quant. Spectrosc. Radiat. Transfer*, *19*, 451–453, doi:10.1016/0022-4073(78)90120-6.

Sentman, D. D., E. M. Wescott, D. L. Osborne, D. L. Hampton, and M. J. Heavner (1995), Preliminary results from the Sprites94 aircraft campaign: 1. Red sprites, *Geophys. Res. Lett.*, *22*, 1205–1208, doi:10.1029/95GL00583.

Stanley, M., P. Krehbiel, M. Brook, C. Moore, W. Rison, and B. Abrahams (1999), High speed video of initial sprite development, *Geophys. Res. Lett.*, *26*, 3201–04, doi:10.1029/1999GL010673.

Stenbaek-Nielsen, H. C., and M. G. McHarg (2008), High time-resolution sprite imaging: observations and implications, *J. Phys. D: Appl. Phys.*, *41*(23), 234,009, doi:10.1088/0022-3727/41/23/234009.

Stenbaek-Nielsen, H. C., D. R. Moudry, E. M. Wescott, D. D. Sentman, and F. T. São Sabbas (2000), Sprites and possible mesospheric effects, *Geophys. Res. Lett.*, *27*, 3829–3832, doi:10.1029/2000GL003827.

Stenbaek-Nielsen, H. C., M. G. McHarg, T. Kanmae, and D. D. Sentman (2007), Observed emission rates in sprite streamer heads, *Geophys. Res. Lett.*, *34*, L11105, doi:10.1029/2007GL029881.

Stenbaek-Nielsen, H. C., R. Haaland, M. G. McHarg, B. A. Hensley, and T. Kanmae (2010), Sprite initiation altitude measured by triangulation, *J. Geophys. Res.*, *115*, A00E12, doi:10.1029/2009JA014543.

Stenbaek-Nielsen, H. C., T. Kanmae, M. G. McHarg, and R. Haaland (2013), High-Speed Observations of Sprite Streamers, *Surveys in Geophysics*, doi:10.1007/s10712-013-9224-4.

Suszcynsky, D. M., R. A. Roussel-Dupré, W. A. Lyons, and R. A. Armstrong (1998), Blue-light imagery and photometry of sprites, *J. Atmos. Sol. Terr. Phys.*, *60*(7–9), 801–809, doi:10.1016/S1364-6826(98)00027-3.

Vallance Jones, A. (1974), *Aurora*, D. Reidel Publishing Company.

Wescott, E. M., H. C. Stenbaek-Nielsen, D. D. Sentman, M. J. Heavner, D. R. Moudry, and F. T. S. Sabbas (2001), Triangulation of sprites, associated halos and their possible relation to causative lightning and micrometeors, *J. Geophys. Res.*, *106*(A6), 10,467–477, doi:10.1029/2000JA000182.

Whiting, E. E., and R. W. Nicholls (1974), Reinvestigation of rotational-line intensity factors in diatomic spectra, *Astrophys. J. Suppl. Ser.*, *27*, 1, doi:10.1086/190286.

Whiting, E. E., J. A. Paterson, I. Kovács, and R. W. Nicholls (1973), Computer checking of rotational line intensity factors for diatomic transitions, *J. Mol. Spectrosc.*, *47*, 84–98, doi:10.1016/0022-2852(73)90078-7.

Whiting, E. E., A. Schadee, J. B. Tatum, J. T. Hougen, and R. W. Nicholls (1980), Recommended conventions for defining transition moments and intensity factors in diatomic molecular spectra, *J. Mol. Spectrosc.*, *80*, 249–256, doi:10.1016/0022-2852(80)90137-X.

Williams, E., E. Downes, R. Boldi, W. Lyons, and S. Heckman (2007), Polarity asymmetry of sprite-producing lightning: A paradox?, *Radio Sci.*, *42*, RS2S17, doi:10.1029/2006RS003488.

Williams, E. R. (2010), Origin and context of C. T. R. Wilson's ideas on electron runaway in thunderclouds, *J. Geophys. Res.*, *115*, A00E50, doi:10.1029/2009JA014581.

Wilson, C. T. R. (1924), The electric field of a thundercloud and some of its effects, *Proc. R. Soc. London*, *37*, D32, doi:10.1088/1478-7814/37/1/314.